

**HIGH STRENGTH ALUMINUM MATRIX COMPOSITES REINFORCED
WITH Al_3Ti AND TiB_2 IN-SITU PARTICULATES**

by
Siming Ma

A Dissertation

*Submitted to the Faculty of Purdue University
In Partial Fulfillment of the Requirements for the degree of*

Doctor of Philosophy



School of Engineering Technology

West Lafayette, Indiana

May 2021

**THE PURDUE UNIVERSITY GRADUATE SCHOOL
STATEMENT OF COMMITTEE APPROVAL**

Prof. Xiaoming Wang, Chair

School of Engineering Technology

Prof. David Johnson

Department of Material Engineering

Prof. Sarah Leach

Department of Mechanical and Engineering Technology

Prof. Milan Rakita

School of Engineering Technology

Approved by:

Dr. Kathyne A. Newton

To my parents

ACKNOWLEDGMENTS

Please let me express my sincere gratitude to all who have helped me during my Ph.D. program and the accomplishment of this dissertation.

Firstly, I would like to thank for my advisor, Dr. Xiaoming Wang, for his guidance and support in my research and life all along my Ph.D. program.

Appreciated for my thesis committee members: Prof. David Johnson, Prof. Sarah Leach and Prof. Milan Rakita for their guidance and comments for my research work. Also thanks for Prof. Zhen Zhao, Prof. Xincun Zhuang and Prof. Zhe Chen from Shanghai Jiao Tong University for their kind support in my doctoral study and research.

Besides, I would like to thank the visiting scholars, Dr. Yongsheng Wang and Dr. Yuqing Wang for their help in my experimental work. Also thanks for my colleague Dr. Aoke Jiang for his support in Purdue University. In addition, I want to thank all the staff from School of Engineering Technology, who have helped me in my study and research in Purdue University. Also thanks for all the staff and students who have supported me in my life and research throughout my doctoral years in Purdue University. Special thanks to Dr. Joshua Huang from Ryobi USA Inc. for his guidance in my internship and research. Also thanks to Dr. Chuan Zhang from CompuTherm LLC and Dr. Nan Li from the Center for Integrated Nanotechnologies, Los Alamos National Laboratory for their help in experimental supports.

Finally, special thanks to my mother and my father. They have been always supporting and encouraging me during my Ph.D. program.

TABLE OF CONTENTS

LIST OF TABLES	9
LIST OF FIGURES	10
ABSTRACT	14
CHAPTER 1. INTRODUCTION	16
1.1 Background	16
1.2 Scope of Study	18
1.3 Significance of Study	19
1.4 Research Questions	19
1.5 Assumptions	19
1.6 Limitations	20
1.7 Delimitations	21
1.8 Summary	21
CHAPTER 2. REVIEW OF LITERATURE	22
2.1 Overview of in-situ PRAMCs	22
2.2 Fabrication of in-situ PRAMCs with Al ₃ Ti and TiB ₂	25
2.2.1 Solid–Liquid Reaction Processes	25
2.2.1.1 Exothermic Dispersion (XD TM)	25
2.2.1.2 Reactive Hot Pressing (RHP)	26
2.2.1.3 Flux-Assisted Synthesis	27
2.2.2 Solid–Solid Reaction Process	28
2.3 Mechanical properties of PRAMCs	29
2.3.1 Tensile Behavior	29
2.3.2 Other mechanical properties	30
2.3.3 Ex-situ vs In-situ	31
2.4 Strengthening Mechanisms	33
2.5 Micromechanical simulation of PRAMCs	37
2.6 Summary	40
CHAPTER 3. FRAMEWORK AND METHODOLOGY	41
3.1 Research Approach	41

3.2 Materials Preparation	41
3.2.1 In-situ synthesis	41
3.2.2 Rolling	42
3.2.3 Heat treatment.....	43
3.3 Mechanical Properties Characterization	44
3.4 Microstructure Characterization	44
3.4.1 X-ray Diffraction	44
3.4.2 Optical Microscopy	44
3.4.3 Scanning Electron Microscopy.....	45
3.4.4 Transmission Electron Microscopy	45
3.4.5 Quantitative Image Analysis.....	46
3.5 Thermodynamic Calculations	46
3.6 Finite Element Modelling	46
3.7 Summary	47
CHAPTER 4. MICROSTRUCTURES AND MECHANICAL PROPERTIES OF IN-SITU Al_3Ti	
PARTICULATE REINFORCED A356 COMPOSITES	48
4.1 Introduction.....	48
4.2 Experiment.....	49
4.3 Microstructure Analysis.....	50
4.3.1 SEM analysis	50
4.3.2 EDS analysis.....	53
4.4 Mechanical Properties.....	55
4.5 Discussions	57
4.5.1 Effect of Sr addition.....	57
4.5.2 Effect of Al_3Ti	58
4.5.3 Effect of heat treatment	60
4.6 Summary	61
CHAPTER 5. EVOLUTION OF INTERMETALLIC PHASES IN AN AL-SI-TI ALLOY	
DURING SOLUTION TREATMENT.....	63
5.1 Introduction.....	63
5.2 Experiment.....	64

5.3 Microstructure.....	65
5.3.1 SEM analysis	65
5.3.2 EDS analysis.....	67
5.3.3 TEM analysis	70
5.4 Thermodynamic calculations of the Al–Si–Ti system.....	74
5.5 Al-Si-Ti phase evolution.....	77
5.6 Summary	80
CHAPTER 6. THREE-DIMENSIONAL (3D) MICROMECHANICAL SIMULATION OF THE EFFECT OF PARTICLE SIZE, FRACTION AND DISTRIBUTION ON THE MECHANICAL BEHAVIOR OF AN IN-SITU AL ₃ Ti/A356 COMPOSITE	82
6.1 Introduction.....	82
6.2 Material and Experiment.....	83
6.3 Modeling.....	85
6.4 Micromechanical Simulation.....	87
6.4.1 Constitutive behavior.....	87
6.4.2 Damage mechanisms	88
6.4.3 Loading and Boundary conditions.....	91
6.5 Simulation Results	92
6.5.1 Model validation.....	92
6.5.2 Effect of particle size	95
6.5.3 Effect of particle fraction.....	100
6.5.4 Effect of particle distribution.....	102
6.6 Discussions	104
6.7 Summary	109
CHAPTER 7. EFFECT OF HOT ROLLING AND HEAT TREATMENT ON MICROSTRUCTURE AND MECHANICAL PROPERTIES OF AN IN-SITU TiB ₂ /AL-CU-MG-SC COMPOSITE	111
7.1 Introduction.....	111
7.2 Experiment.....	112
7.3 Microstructure.....	114
7.3.1 Microstructure of in-situ TiB ₂ /Al2618 composites	114

7.3.2 EDS analysis	117
7.4 Mechanical Properties.....	120
7.4.1 Tensile properties.....	120
7.4.2 Fracture surface	122
7.5 Discussions	123
7.5.1 Effect of hot rolling	124
7.5.2 Effect of heat treatment	125
7.5.3 Effect of TiB ₂ particulates	126
7.6 Summary	128
CHAPTER 8. CONCLUSIONS	131
REFERENCES	134
PUBLICATIONS.....	154

LIST OF TABLES

Table 2.1. Mechanical properties of PRAMCs with in-situ Al_3Ti and TiB_2 reinforcements from related researches.	32
Table 4.1. Tensile properties of A356 alloy and Al_3Ti /A356 composites.....	56
Table 5.1. EDS point analysis on the locations of $(\text{Al,Si})_3\text{Ti}$ and the lamellar structure in the samples after different solution treatment times.....	69
Table 5.2. The crystallographic data of the related phases with a comparison of the measured interplanar crystal spacings from FFT patterns in Fig. 5.5.....	73
Table 5.3. Diffusion data for the dilute solution of Ti and Si in α -Al matrix at solution treatment temperature 540 °C (813 K), where R is the gas constant (8.31 J/mol·K) (Christian, 1975).	79
Table 7.1. Chemical composition of the studied materials (in wt. %).	113

LIST OF FIGURES

Figure 1.1. Examples of applications of AMCs in industries. (a) Honda Prelude 2.0l-cylinder block (Donaldson Steven L & Miracle Daniel B, 2001); (b) F-16 illustrating ventral fins on the bottom of the fuselage aft (rearward) of the wings (Donaldson Steven & Miracle Daniel, 2001); (c) Conductor cables of power transmission towers (Miracle, 2005).	17
Figure 2.1. Microstructure of (a) Al ₃ Ti/A356 composite (S. Ma & Wang, 2019); (b) TiB ₂ /Al2618 composite (S. Ma et al., 2020); (c) Al-5Ti-1B master alloy with TiB ₂ at the α -Al grain boundaries and Al ₃ Ti in α -Al grain centers (X. Wang et al., 2015).	24
Figure 2.2. Schematic figure for the fabrication XD dispersion-hardened composites. (S. Tjong & Ma, 2000).....	26
Figure 2.3. Schematic figure showing an apparatus of fabricating in-situ MMCs by flux-assisted synthesis. (S. Tjong & Ma, 2000).....	28
Figure 2.4. (a) 2D multi-particle RVE model with round inclusions (Qing, 2013b); (b) 3D multi-particle RVE models with different particle morphology (Chawla et al., 2006).....	38
Figure 2.5. Flow chart showing typical procedure for micromechanical simulations on the microstructure-based RVE by FEM.....	39
Figure 3.1. The laboratory rolling mill for rolling process.	43
Figure 3.2. Heating oven for heat treatment of the samples.	43
Figure 4.1. Backscattered electron images of as-cast (a) A356 alloy, (b) Al ₃ Ti/A356 and (c) Al ₃ Ti/A356-Sr composites; and T6 treated (d) A356, (e) Al ₃ Ti/A356 and (f) Al ₃ Ti/A356-Sr composites.....	51
Figure 4.2. Statistics of (a) average particle diameter and (b) average aspect ratio of Al ₃ Ti particles; (c) average particle diameter and (d) average aspect ratio of Si particles in different samples. ..	52
Figure 4.3. EDS analyses of as-cast Al ₃ Ti/A356-Sr composite (a) Back scattered electron image with an inserted EDS spectrum from point 1 on an Al ₃ Ti particle; (b)~(e) Elemental mapping of Al, Ti, Si and Sr elements, respectively.....	53
Figure 4.4. EDS analysis of a T6 treated Al ₃ Ti/A356-Sr sample (a) Back scattered electron image with an inserted image shows the magnified structure of Si-rich zone); (b)~(e) Elemental mapping of Al, Ti, Si and Sr, respectively; (f) a magnified SEM image showing the structure of a Si-rich zone; (g) and (h) spectra of point 1 and point 2 in figure (a), respectively.	54
Figure 4.5. Stress-strain curves of A356 and Al ₃ Ti/A356 composites	55
Figure 4.6. Typical fracture surface of as-cast (a) A356 alloy, (b) Al ₃ Ti/A356 and (c) Al ₃ Ti/A356-Sr composites; and T6 treated (d) A356, (e) Al ₃ Ti/A356 and (f) Al ₃ Ti/A356-Sr composites.	56
Figure 5.1. Backscattered electron images of the Al-Si-Ti alloy (a) at as-cast state; and after solution treatment at 540 °C for (b) 4 h; (c) 12h; (d) 24 h; (e) 48 h; (f) 72 h.	65

Figure 5.2. Percentage of intermetallic particulates containing lamellar structure in the Al-Si-Ti alloy after different solution treatment time. 67

Figure 5.3. (a) Back-scattered electron image of the as-cast Al-Si-Ti alloy with (b)~(e) EDS Elemental mapping of Al, Si, Ti and Mg elements, respectively and (f) an EDS spectrum from Point 1 on an intermetallic particulate in figure (a). 67

Figure 5.4. (a) Back-scattered electron image of the Al-Si-Ti alloy after 4 h solution treatment, with (b)~(e) EDS Elemental mapping of Al, Si, Ti and Mg elements, respectively, and (f)~(g) the EDS spectra from Point 1 on an intermetallic particulate and Point 2 on the lamellar structure in figure (a), respectively. 68

Figure 5.5. (a) A TEM bright field image of the composite after solution treatment for 4 h showing an interface between an $(Al,Si)_3Ti$ particulate and the lamellar structure; (b1) scanning transmission electron microscopy (STEM) high-angle annular dark-field (HAADF) of the red rectangular area in figure (a) and (b2~b4) corresponding EDS elemental mappings of Al, Ti, and Si. (c1) magnified TEM image of Area 1 in figure (a); (c2) magnified HRTEM image of the red rectangular area in figure (c1); (d1) magnified TEM figure of Area 2 in figure (a); (d2) magnified HRTEM image of the red rectangular area in figure (d1); (e1)~(e3) corresponding FFT patterns of different locations in figure (c2); (f1, f2) corresponding FFT patterns of different locations in figure (d2); (g) the FFT pattern from the $(Al,Si)_3Ti$ -Al interface; (h) simulated diffraction pattern of $TiSi_2$ (C49-type) from $[100]$ axis; (i) the FFT pattern from the τ_2 -Al interface. 70

Figure 5.6. (a) A calculated isothermal section of Al-Si-Ti ternary system at 540 °C; (b) Magnified red rectangular area in the Al-rich corner in figure (a); (c) and (d) The evolution of phase fractions in the Al-7.10 at. % Si-1.34 at.% Ti alloy simulated under equilibrium condition and Scheil condition, respectively. 74

Figure 5.7. Schematic drawing of the transition from a solid $(Al,Si)_3Ti$ particulate to a lamellar structure with the increase of solid solution treatment time; (a) blocky $(Al,Si)_3Ti$ in as-cast alloy; (b) Si enrichment in a part of the particulate and the diffusion of elements along the arrows; (c) formation of lamellar structure limited to only parts of the particulates together with further Si enrichment and elemental diffusion in another area; (d) a completion of the transition of the entire $(Al,Si)_3Ti$ particulate into a lamellar structure. 77

Figure 6.1. Backscattered electron images showing typical microstructure of (a) T6-A356 matrix and (b) T6- Al_3Ti /A356 composite in this work; (c) Optical images showing four typical areas near the fracture surface of the Al_3Ti /A356 composite after tensile test; (d) Particle size distribution of Al_3Ti in the Al_3Ti /A356 composite. 85

Figure 6.2. (a) Examples of 3D automatically generated RVEs containing randomly distributed Al_3Ti particles with various sizes and volume fractions. (b) 5pct-5 μ m RVEs with random distribution, 50 % particle clustering, and 100 % particle clustering. (The edge length of all the RVEs in this figure is 30 μ m) 86

Figure 6.3. The critical value $D\eta_c$ of the T6-A356 matrix determined by uniaxial tensile simulation. (SDV5 in the legend refers to $D\eta$) 89

Figure 6.4. Schematic image of loading and boundary conditions on the 3D RVEs. 92

Figure 6.5. Effect of (a) the parameter kd and (b) $efcr$ and $emaxck$ on the obtained nominal stress-strain curves from RVE simulation.	93
Figure 6.6. Effect of (a) the selected RVE edge length; (b) mesh density; and (c) model variation on the simulation nominal stress strain curves; (d) comparison between the nominal stress-strain curves from 5pct-5 μ m RVE and from experimental uniaxial tensile test.	95
Figure 6.7. (a1)~(a3) simulation stress-strain curves of 5pct-3, 5, and 10 μ m RVEs, respectively. (b1)~(b3) the average S11 stress component of Al ₃ Ti and A356 matrix phases corresponding to the RVEs in Figs. 6.7(a1)~(a3), respectively.....	96
Figure 6.8. (a) S11 stress component distributions on the Al ₃ Ti particles at different nominal strains of 5pct-3, 5, and 10 μ m RVEs; (b) The matrix damage parameter $D\eta$ distribution at different nominal strains of 5pct-3, 5, and 10 μ m RVEs (A section on X-Z plane is shown for each model. $D\eta$ of the gray colored elements here has exceeded the critical value $D\eta_c$, indicating that damage has already occurred on those elements. It is also applicable for Figs. 6.10(b) and 6.12(b)).	99
Figure 6.9. (a1)~(a3) The simulation stress-strain curves of of 5, 10, and 15pct-5 μ m RVEs, respectively. (b1)~(b3) The average S11 stress component of Al ₃ Ti and A356 matrix phases corresponding to the RVEs in Figs. 6.9(a1)~(a3), respectively.....	100
Figure 6.10. (a) S11 stress component distributions on the Al ₃ Ti particles at different nominal strains of 5, 10, and 15pct-5 μ m RVEs; (b) The matrix damage parameter $D\eta$ distribution at different nominal strains of these three RVEs.	101
Figure 6.11. (a) Simulation stress-strain curves of 5pct-5 μ m, 5pct-5 μ m-clu50% and 5pct-5 μ m-clu100% RVEs, respectively. (b) The average S11 stress component of Al ₃ Ti and A356 matrix phases corresponding to the RVEs in Figure 6.11(a), respectively.	102
Figure 6.12. (a) S11 stress component distributions on the Al ₃ Ti particles at different nominal strains of 5pct-5 μ m, 5pct-5 μ m-clu50% and 5pct-5 μ m-clu100% RVEs; (b) The matrix damage parameter $D\eta$ distribution at different nominal strains of these three RVEs.....	103
Figure 6.13. (a) Predicted Young's Modulus of Al ₃ Ti/A356 composites from simulation and comparison with the results calculated by Tsai-Halpin equation; (b) Predicted yield strength (YS) from simulation and comparison with the results calculated by modified shear lag model and micromechanical approach; (c) Predicted elongation of Al ₃ Ti/A356 composites from simulation and comparison with experimental results of related works. (The surface in the image refers to a polynomial 2D fitting surface from the simulation results of RVEs with random particle distribution in this work, UST = ultrasonic treatment).....	108
Figure 7.1. (a) XRD spectra of Al2618 alloy and in-situ TiB ₂ /Al2618 composites (R35 samples, heat-treated); (b) Backscattered electron image (BSE) shows typical morphology of TiB ₂ particulates; (c) The size distribution of the in-situ TiB ₂ particulates (C8-R35 sample).....	114
Figure 7.2. OM images of the as-rolled Al2618 alloy and TiB ₂ /Al2618 composites taken from RD-TD plane (a) Al2618-R35, (b) C4-R35, (c) C8-R35; (d) Al2618-R70; (e) C4-R70; and (f) C8-R70.	115

Figure 7.3. BSE images of the as-rolled Al2618 alloy and TiB₂/Al2618 composites taken from RD-TD plane (a) Al2618-R35, (b) C4-R35, (c) C8-R35; (d) Al2618-R70; (e) C4-R70; and (f) C8-R70..... 116

Figure 7.4. OM images of the heat-treated Al2618 alloy and TiB₂/Al2618 composites (a) Al2618-R35, (b) C4-R35, (c) C8-R35; (d) Al2618-R70; (e) C4-R70; and (f) C8-R70..... 117

Figure 7.5. EDS analysis of as-rolled TiB₂/Al2618 composite (C8-R70 sample) (a) Electron image; (b) Elemental composition from the point analysis in figure (a) (in at. %); (c) Elemental mapping..... 118

Figure 7.6. EDS analysis of heat-treated TiB₂/Al2618 composite (C8-R60 sample) (a) Electron image; (b) Elemental composition from the point analysis in figure (a) (in at. %); (c) Elemental mapping..... 119

Figure 7.7. Uniaxial tensile properties of the as-rolled Al2618 and TiB₂/Al2618 composites; (a) Tensile stress-strain curves; (b) Statistical histogram..... 120

Figure 7.8. Uniaxial tensile properties of the heat-treated Al2618 and TiB₂/Al2618 composites; (a) Tensile stress-strain curves; (b) Statistical histogram..... 121

Figure 7.9. Typical fracture surfaces of the as-rolled Al2618 alloy and TiB₂/Al2618 composites; (a) Al2618-R35, (b) C4-R35, (c) C8-R35; (d) Al2618-R70; (e) C4-R70; and (f) C8-R70. 122

Figure 7.10. Typical fracture surfaces of the heat-treated Al2618 alloy and TiB₂/Al2618 composites; (a) Al2618-R35, (b) C4-R35, (c) C8-R35; (d) Al2618-R70; (e) C4-R70; and (f) C8-R70..... 123

ABSTRACT

Aluminum alloys have broad applications in aerospace, automotive, and defense industries as structural material due to the low density, high-specific strength, good castability and formability. However, aluminum alloys commonly suffer from problems such as low yield strength, low stiffness, and poor wear and tear resistance, and therefore are restricted to certain advanced industrial applications. To overcome the problems, one promising method is the fabrication of aluminum matrix composites (AMCs) by introducing ceramic reinforcements (fibers, whiskers or particles) in the metal matrix. AMCs typically possess advanced properties than the matrix alloys such as high specific modulus, strength, wear resistance, thermal stability, while remain the low density. Among the AMCs, particulate reinforced aluminum matrix composites (PRAMCs) are advantageous for their isotropic properties, ease of fabrication, and low costs. Particularly, the PRAMCs with in-situ particulate reinforcements have received great interest recent years. The in-situ fabricated particles are synthesized in an aluminum matrix via chemical reactions. They are more stable and finer in size, and have a more uniform distribution in the aluminum matrix and stronger interface bonding with aluminum matrix, compared to the ex-situ particulate reinforcements. As a consequence, the in-situ PRAMCs have superior strength and mechanical properties as advanced engineering materials for a broad range of industrial applications.

This dissertation focuses on the investigation of high strength aluminum matrix composites reinforced with in-situ particulates. The first chapter provides a brief introduction for the studied materials in the dissertation, including the background, the scope, the significance and the research questions of the study. The second chapter presents the literature review on the basic knowledge, the fabrication methods, the mechanical properties of in-situ PRAMCs. The strengthening mechanisms and strategies of in-situ PRAMCs are summarized. Besides, the micromechanical simulation is introduced as a complementary methodology for the investigation of the microstructure-properties relationship of the in-situ PRAMCs. The third chapter shows the framework and methodology of this dissertation, including material preparation and material characterization methods, phase diagram method and finite element modelling.

In Chapter 4, the microstructures and mechanical properties of in-situ Al_3Ti particulate reinforced A356 composites are investigated. The microstructure and mechanical properties of in-

situ 5 vol. % $\text{Al}_3\text{Ti}/\text{A356}$ composites are studied either taking account of the effects of T6 heat treatment and strontium (Sr) addition or not. Chapter 5 studies the evolution of intermetallic phases in the Al-Si-Ti alloy during solution treatment, based on the work of Chapter 4. The as-cast Al-Si-Ti alloy is solution treated at 540 °C for different periods between 0 to 72 h to understand the evolution of intermetallic phases. In Chapter 6, a three-dimensional (3D) micromechanical simulation is conducted to study the effects of particle size, fraction and distribution on the mechanical behavior of the in-situ $\text{Al}_3\text{Ti}/\text{A356}$ composite. The mechanical behavior of the in-situ $\text{Al}_3\text{Ti}/\text{A356}$ composite is studied by three-dimensional (3D) micromechanical simulation with microstructure-based Representative Volume Element (RVE) models. The effects of hot rolling and heat treatment on the microstructure and mechanical properties of an in-situ $\text{TiB}_2/\text{Al2618}$ composite with minor Sc addition are investigated in Chapter 7. $\text{TiB}_2/\text{Al2618}$ composites ingots were fabricated *in-situ* via salt-melt reactions and subjected to hot rolling. The microstructure and mechanical properties of the $\text{TiB}_2/\text{Al2618}$ composite are investigated by considering the effects of particle volume fraction, hot rolling thickness reduction, and heat treatment.

CHAPTER 1. INTRODUCTION

1.1 Background

High performance and low-weight structural materials are increasingly required in a wide range of industrial applications nowadays. As commonly applied lightweight alloys, aluminum alloys are promising candidate materials to fulfill the requirement. Aluminum alloys are advantageous for low density, high strength-to-weight ratio, good castability and formability, high electric and thermal conductivity and good corrosion resistance. Therefore, aluminum alloys have been widely used in a variety of industries, including aerospace, automotive, and defense industries. However, aluminum alloys commonly suffer from limitations for certain industrial applications due to their low yield strength, low stiffness, and poor resistance to wear and tear (Lloyd, 1994; McEvily Jr, 1994; Q. G. Wang & Davidson, 2001).

To overcome the problems, one promising way is the introduction of hard ceramic reinforcements (fibers, whiskers or particles) into the metal matrix, obtaining the so-called metal matrix composites (MMCs). MMCs consist of at least two chemically and physically distinct phases, suitably distributed to give properties that are not obtainable with/or any of the phases individually (Ibrahim et al., 1991; Miracle, 2005). Generally, MMCs have a fibrous or particulate phase distributed in an appropriate manner in a matrix. Compared to the matrix material, MMCs offer higher specific strength and stiffness, higher creep resistance and improved fatigue characteristics (Chawla & Chawla, 2013).

With the introduction of reinforcements in aluminum alloy matrices, AMCs are achieved with advanced properties such as high specific modulus, strength, wear resistance, thermal stability, and generally remain the low density, compared to the matrix counterparts (Lloyd, 1994; Mortensen & Llorca, 2010; S. Tjong & Ma, 2000). AMCs have drawn a great deal of research interest over the past 40 years, progressing from laboratory experiments to diverse applications across a number of commercial markets (Srivatsan et al., 2018; S. Tjong & Ma, 2000). The major applications of AMCs are in the automotive, aerospace, recreation, and infrastructure industries (Ceschini et al., 2017; Miracle, 2005; Suthar & Patel, 2018), some examples of the applications are shown as Fig. 1.1.

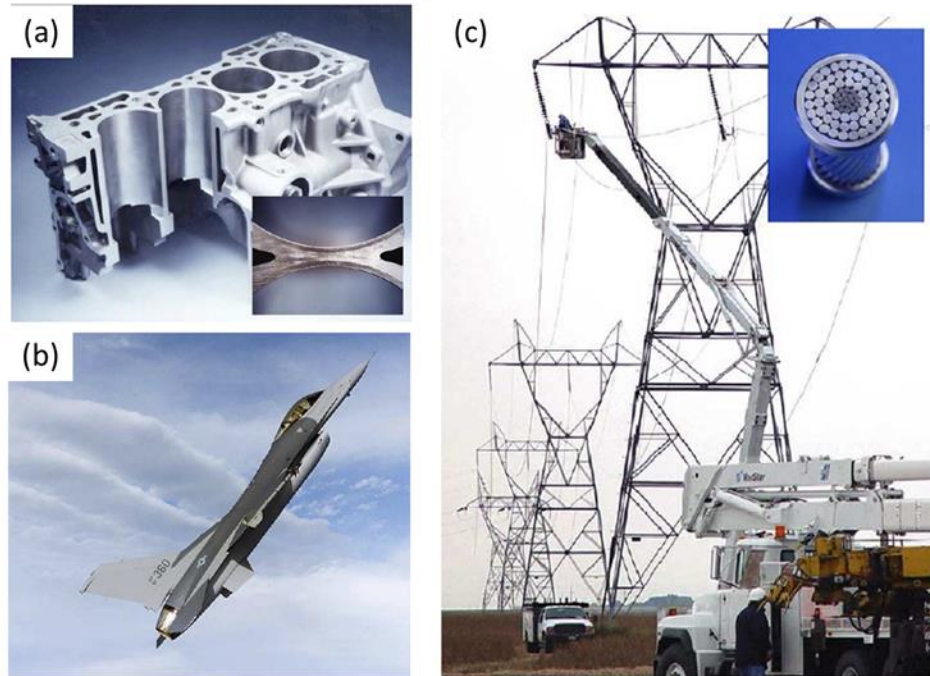


Figure 1.1. Examples of applications of AMCs in industries. (a) Honda Prelude 2.0l-cylinder block (Donaldson Steven L & Miracle Daniel B, 2001); (b) F-16 illustrating ventral fins on the bottom of the fuselage aft (rearward) of the wings (Donaldson Steven & Miracle Daniel, 2001); (c) Conductor cables of power transmission towers (Miracle, 2005).

Among various AMCs, particulate reinforced aluminum matrix composites (PRAMCs) have attracted an intensive research interest since the late 1980s (Srivatsan et al., 2018). Compared to AMCs reinforced with fibers and whiskers, PRAMCs are advantageous for their isotropic properties, ease of fabrication, and lower costs due to the relatively inexpensive ceramic particles (Ibrahim et al., 1991; S. Tjong & Ma, 2000). PRAMCs are potential candidates to fulfill the requirement of light weight and high strength in aviation and automotive industries (D.L. Chung, 2009). Additionally, particulate reinforced composites are normally inexpensive compared to continuous fiber reinforced composites (Chawla & Chawla, 2013). Numerous studies on PRAMCs have been reported, including various ceramic reinforcements such as SiC, B₄C, Al₃Ti, TiB₂, Al₂O₃, TiC and etc. embedded in aluminum and its alloys (Kang & Chan, 2004; Nukami & Flemings, 1995; Shorowordi et al., 2003; T. Wang et al., 2014; X. Wang et al., 2004; Z. Wang et al., 2011).

In conventional practice, the reinforcing particles are prepared separately prior to the fabrication of AMCs. These are known as ex-situ AMCs. The ex-situ fabricated particles are

generally coarse in size, with their dimensions limited by the starting powder size. The ex-situ particle powders, which tend to suffer from surface contamination, usually have poor wettability and weak interfacial bonding with the matrix (S. Tjong & Ma, 2000). In comparison, in-situ fabricated particles, which are synthesized in an aluminum matrix via chemical reactions, are thermodynamically stable, finer in size, and dispersed more uniformly. The size of in-situ particles can range from submicron to several microns in size. In-situ particles have clean and strong interfacial bonding with the matrix (S. Tjong & Ma, 2000; X. Wang et al., 2004). The benefits of in-situ AMCs versus ex-situ AMCs is that in-situ AMCs offer a promise in improving properties.

In summary, AMCs, especially the in-situ PRAMCs are potential lightweight and advanced engineering materials for a broad range of superior industrial applications as a substitution for common aluminum alloys and possibly some steels. The investigation of PRAMCs is greatly attractive and worthwhile for the applications in various industrial fields.

1.2 Scope of Study

This study focuses on the investigation of high strength aluminum matrix composites reinforced with in-situ particulates. The Al_3Ti and TiB_2 particulates are introduced into aluminum alloy matrices in-situ via metal-salt reaction, fabricating in-situ PRAMCs. The microstructure and mechanical properties of PRAMCs are studied. The strengthening mechanisms by the reinforcements are focused. Moreover, to further improve the mechanical properties of PRAMCs, heat treatment, alloy element addition as well as plastic deformation are employed and their effects on microstructure and mechanical properties are investigated accordingly. Furthermore, micromechanical simulation is applied to simulate the mechanical properties and fracture behavior of PRAMCs, in order to revealing the relationships between the microstructural features (particle size, fraction, special distribution and etc.) and mechanical properties. In the dissertation, the frequently applied aluminum alloys A356 and Al2618 are selected as matrices. The Al_3Ti and TiB_2 particulates are introduced into the aluminum alloy matrices in-situ, fabricating $\text{Al}_3\text{Ti}/\text{A356}$ and $\text{TiB}_2/\text{Al2618}$ composites as the investigated subjective materials.

1.3 Significance of Study

Aluminum alloys typically suffer from certain limitations due to their low yield strength, low stiffness, and poor resistance to wear and tear, and therefore cannot meet the strength and stiffness demand as structure material for certain industrial applications. The addition of ceramic hard particulate reinforcements to soft aluminum alloys can effectively increase the stiffness, strength and wear resistance at both ambient and elevated temperatures (Ceschini et al., 2017; Tearney et al., 1997). In addition, high strength PRAMCs can potentially replace steels with similar mechanical properties but with an evidently light weight, which is helpful to save energy and reduce the environmental impact from emission.

Besides, it is significant to investigate the microstructure-property relationship of PRAMCs, which has been the focus of research in this field. The microstructural features, such as grain size, particle properties, size, fraction, distribution, can result in different strengthening effects on the mechanical property of the composites via different strengthening mechanisms. Moreover, the mechanical properties of PRAMCs, such as stiffness, strength, ductility and fracture behaviors are all microstructure-dependent.

Furthermore, it is also necessary to investigate promising methods or strategies to further enhance the mechanical properties of PRAMCs. Typical strategies include heat treatment, adding alloying elements, as well as secondary deformation processing. The corresponding investigation is also significant.

1.4 Research Questions

The main research questions of this study are:

1. What are the potential strategies to obtain high strength PRAMCs?
2. How do the Al_3Ti and TiB_2 in-situ particulates affect the mechanical properties of aluminum alloys via the fabrication of PRAMCs.
3. How to predict the mechanical properties of PRAMCs from the microstructural features by simulation and subsequently setting up microstructure-property relationships?

1.5 Assumptions

The assumptions are as follows:

1. The control of samples: the samples are taken from the center of as-cast $\text{Al}_3\text{Ti}/\text{A356}$ composite ingots and $\text{TiB}_2/\text{Al2618}$ rolled sheets. It is assumed that both $\text{Al}_3\text{Ti}/\text{A356}$ ingots and $\text{TiB}_2/\text{Al2618}$ rolled sheets are homogeneous and representative in microstructure in their center location.
2. The control of the material ingots: The $\text{Al}_3\text{Ti}/\text{A356}$ and $\text{TiB}_2/\text{Al2618}$ composites are fabricated with controlled experimental parameters. It is assumed that for the same material, the microstructure and quality of different ingots are stable.
3. The experimental data from the material characterization comes from reliable equipment and sufficient tests. The results are assumed to reveal the microstructure and mechanical properties of the investigated materials.
4. Assumptions in micromechanical simulation: For the micromechanical simulation, it is assumed that the constitution (aluminum matrix and particulates) of the representative volume element (RVE) models are homogeneous and isotropic. The defects in the materials are also not considered.

1.6 Limitations

The limitations are as follows:

1. High strength aluminum matrix composites reinforced with Al_3Ti and TiB_2 in-situ particulates. However, only A356 and Al2618 alloys are taken as matrices for example. It may restrict the generalizability of the research findings.
2. The mechanical properties of the investigated materials are evaluated only by uniaxial tensile tests.
3. The accuracy of the experimental data from material characterization is dependent on the accuracy of equipment.
4. Some microstructure features are obtained by microstructure image analysis. The accuracy of the method could have statistical error, due to the limitation of the number of samples.
5. In the micromechanical simulation, the aluminum matrix and reinforcing particles are assumed to be homogeneous and isotropic. The effect of the grain size and texture of the matrix, as well as the variation of size and morphology of the particles are not considered.

1.7 Delimitations

The delimitations are as follows:

1. The current research will investigate aluminum matrix composites reinforced with Al_3Ti and TiB_2 in-situ particulates. Other particulate reinforcements as well as with Al_3Ti and TiB_2 ex-situ particulates are not involved.
2. The mechanical properties of PRAMCs will be the modulus, yield and tensile strength, elongation at room temperature, measured from uniaxial tensile tests. Other mechanical properties will not be investigated, such as wear, fatigue as well as high temperature mechanical properties.
3. The micromechanical simulation will be only conducted by finite element method (FEM) with a uniaxial tensile loading. Other simulation methods and loading types are not involved.

1.8 Summary

The chapter demonstrates a basic introduction of the research project: High strength aluminum matrix composites reinforced with Al_3Ti and TiB_2 in-situ particulates. The background, the scope and the significance of the study are firstly presented, leading the researching questions. Subsequently, the assumptions, limitations and delimitations of the research are pronounced. The next chapter will focus on literature review associated with the research project, including the introduction of PRAMCs, such as the fabrication and their mechanical properties. Moreover, the strengthening mechanisms and strategies in PRAMCs are reviewed, together with the introduction of micromechanical simulation method for PRAMCs.

CHAPTER 2. REVIEW OF LITERATURE

This chapter is a review of literature relevant to the research topic, including the overview, fabrication, mechanical properties of the PRAMCs, the strengthening mechanisms and strategy, and the micromechanical simulation method.

2.1 Overview of in-situ PRAMCs

AMCs refer to materials that have stiff ceramic particles, fibers or whiskers dispersed in a ductile aluminum matrix. The merits of the AMCs over conventional monolithic materials are enhanced strength, stiffness, hardness, wear resistance and etc. AMCs also result in weight savings due to the lightweight aluminum alloy matrix. Additionally, AMCs are relatively low-cost and have the flexibility in design (Ibrahim et al., 1991; Miracle, 2005; Suthar & Patel, 2018).

Among the AMCs, the alloys reinforced with ceramic particulates has been widely studied for decades. They are typically called as particulate reinforced aluminum matrix composites (PRAMCs). The PRAMCs are not only featured for their light-weight and outstanding mechanical properties, but also advantageous for low cost, isotropic properties and ease in fabrication, compared to other kinds of AMCs (Chawla & Shen, 2001; S. Tjong & Ma, 2000). Typical reinforcement particulates are ceramic particles, including carbides, nitrides, oxides and intermetallics. The studied matrix materials include and are not limited to commercial purity Al (Dan et al., 2018), 2xxx-series Al alloys (Al-Cu) (Nampoothiri et al., 2016), 6xxx-series Al alloys (Al-Mg-Si) (S. M. Ma et al., 2014), 7xxx-series Al alloys (Al-Zn-Mg-Cu) (Y. Ma et al., 2018), Al-Si alloys (M. Wang et al., 2014) and etc. The widely studied reinforcing particles are TiB_{2p} (S. M. Ma et al., 2014), Al_3Ti_p (Z. Liu, Rakita, et al., 2014), SiC_p (S. Tjong & Ma, 2000), and ZrB_{2p} (N. M. Kumar et al., 2016) etc.

The reinforcing particulates can be introduced into the aluminum matrix via two ways: ex-situ or in-situ. The ex-situ particulates are prepared separately prior to the composite fabrication. Comparatively, the in-situ particulates are synthesized in a metallic matrix by chemical reactions between elements or between elements and compounds during the composite fabrication. Thus, the two kinds PRAMCs are distinguished as ex-situ PRAMCs and in-situ PRAMCs, respectively. The ex-situ PRAMCs have limitations such as non-uniform distribution of reinforcing particles,

poor bonding, poor isometric properties, interface reaction, incomplete adhesion of reinforcement to the matrix and thermodynamic instability of reinforcement with the matrix. While in-situ PRAMCs can overcome those drawbacks with an uniform particle distribution, grain refinement of the matrix phase, clean interface, enhanced thermal stability and economy in processing over ex-situ PRAMCs (N. Kumar et al., 2016; S. Tjong & Ma, 2000). Because of the great potential that in-situ AMCs offer for widespread applications, a variety of in-situ PRAMCs have been developed for production during the past two decades.

Among the candidate ceramic reinforcements, in-situ TiB_2 and Al_3Ti particles have received great research interest. The in-situ TiB_2 particles have a hexagonal crystal structure. They possess strong covalent bonding, high strength and fatigue resistance. Al_3Ti is featured by low density ($\sim 3.36 \text{ g/cm}^3$), high Young's modulus (216GPa) and high oxidation resistance at the particle-matrix interface (R. Gupta et al., 2018; Nofar et al., 2009; Zeng et al., 2018). The intermetallic phase also has an excellent resistance to oxidation and corrosion in fluoride atmosphere well above the melting point of Al. With in-situ TiB_2 and Al_3Ti particles (or together), the grain size of aluminum matrix alloys is greatly refined (from several hundred microns to less than 100 microns) and thus the mechanical properties are greatly enhanced (Arnberg et al., 1982).

For instance, Al-5Ti-B master alloy (5 wt. % Ti and 1 wt. % B) is widely used as grain refiner in industry. The master alloy is usually added into melt in the total concentration of 0.005, 0.01, and 0.02 wt. % Ti to get fine equiaxed grains (Easton & StJohn, 1999). The family of Al-Ti-B refiners are produced by the reaction of Ti- and B-containing salts with liquid aluminum. The result is a matrix of cubic close-packed (ccp) α -Al containing particles of Al_3Ti and TiB_2 (X. Wang et al., 2015), as shown in Fig. 2.1. in which it is observed that large Al_3Ti particles remain inside the aluminum grain and small TiB_2 particles agglomerate at the grain boundaries.

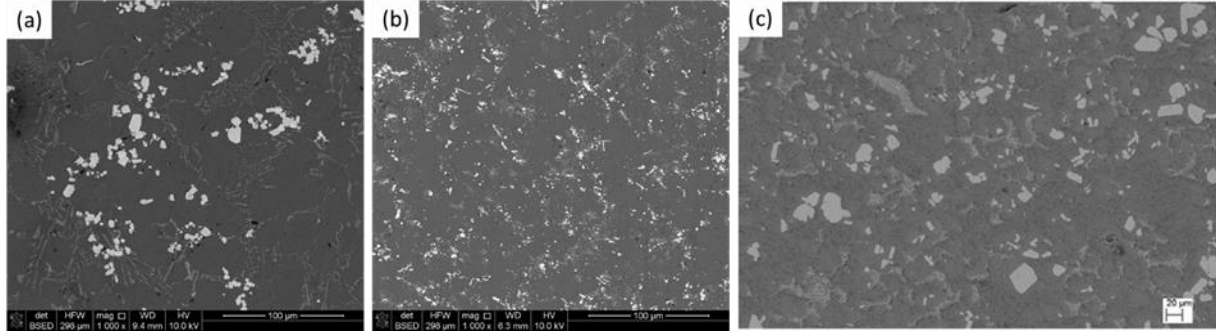


Figure 2.1. Microstructure of (a) $\text{Al}_3\text{Ti}/\text{A356}$ composite (S. Ma & Wang, 2019); (b) $\text{TiB}_2/\text{Al2618}$ composite (S. Ma et al., 2020); (c) Al-5Ti-1B master alloy with TiB_2 at the α -Al grain boundaries and Al_3Ti in α -Al grain centers (X. Wang et al., 2015).

It is indicated that Al_3Ti particles act as heterogeneous nucleation sites for α -Al grains and are situated inside α -Al grains after solidification through a peritectic reaction (Z. Liu et al., 2018). Al_3Ti has a strong bonding with Al due to an epitaxial growth in solidification. The tetragonal crystal structure of Al_3Ti ($a = 0.3848$ nm and $c = 0.8596$ nm) is a superlattice of Al comparable to that of α -Al ($a = 0.4049$ nm). As a result, the interfacial strains in both the a and c directions of Al_3Ti are small (+4.96% and -6.15%, respectively) (X. Wang et al., 2004). In comparison, TiB_2 particles are dispersed both inside Al grains and at grain boundaries. The intergranular TiB_2 particles are presumed to act as centers for the heterogeneous nucleation of α -Al grains when the alloy solidifies. In aluminum alloys refined by Al-Ti-B, the TiB_2 particle size obeys a log-normal distribution within the range between less than $0.1 \mu\text{m}$ to $5 \mu\text{m}$, which is smaller than Al_3Ti .

Due to the above benefits, the Al_3Ti and TiB_2 ceramic particle reinforcements have been applied in both wrought and foundry aluminum matrix alloys. Representative research associated with in-situ Al_3Ti particulates involve Z. Liu et al. (2018) and C. Yang et al. (2018). In these research, Al_3Ti particles generally play a role in refining the grain size, as well as increasing the stiffness, hardness and strength of the matrix materials. Besides, there are a large number of reports on understanding the strengthening effects of in-situ TiB_2 particles in various Al alloy matrices, such as Al-Cu (S. C. Tjong & Lau, 1999), Al-Si (M. Wang et al., 2014), Al-Cu-Mg (Tang et al., 2019), and Al-Mg-Si (S. M. Ma et al., 2014) alloys. It has shown that TiB_2 particles provide multiple particulate reinforcing effects due to the small size and excellent properties in aluminum matrix. The modulus, hardness and strength of the matrices are improved effectively.

2.2 Fabrication of in-situ PRAMCs with Al₃Ti and TiB₂

A variety of fabrication techniques have been evolved in order to obtain in-situ PRAMCs with optimized microstructure and properties. According to the starting phases in the in-situ reactions, the fabrication techniques can be categorized into four categories, as reported by S. Tjong & Ma, (2000). They are: (a) Solid-liquid reaction process; (b) Vapor-liquid-solid reaction process; (c) Solid-solid reaction process, and (d) Liquid-liquid reaction process.

The study of fabrication of Al-Ti-B alloys goes ahead continuously. The fabrication of Al-Ti-B composites (master alloys) is typically realized either by solid-liquid reaction processes or solid-solid reaction processes (N. Kumar et al., 2016). The former includes the methods such as Self-propagating high-temperature synthesis (SHS), Exothermic dispersion (XDTM), Reactive hot pressing (RHP), Flux-assisted synthesis (FAS). The latter involves the methods such as mechanical alloying (MA) and severe plastic deformation (SPD) (S. Tjong & Ma, 2000).

2.2.1 Solid-Liquid Reaction Processes

This process has been widely used to fabricate in-situ MMCs. In the solid-liquid reaction process, reactants react in situ to form reinforcing phases in the presence of a liquid metallic phase. The process is a solvent-assisted reaction wherein the reinforcing particles are generated in the solvent medium via diffusion of the components. The most common approaches via solid-liquid reaction processes are shown as follows:

2.2.1.1 Exothermic Dispersion (XDTM)

In this process, powders of elemental components of high temperature (ceramic) phases (X and Y) are heated in the presence of a third metallic phase (A) above the melting point of A but well below the temperature required to produce ceramic phase XY. An exothermic reaction takes place between X and Y resulting in the formation of submicroscopic hardening particles in the solvent phase. Thus, a master alloy containing a high volume fraction of ceramic reinforcement (about 20~75 vol. %) is produced, as shown in Fig. 2.2.

For instance, Kuruvilla et al. (1990) have fabricated in-situ TiB₂ reinforced Al composite using XD process. Powder blends of Ti, Al and B are first cold-isostatically pressed at a pressure of 200 MPa and subsequently degassed in vacuum at 723 K for 1 h. The Al-Ti-B compact is then

heated to 1073 K in an argon atmosphere and held at that temperature for 15 min. The resulting porous composite is canned and section-rolled into rods of 6 mm in diameter. TiB_2 particles with a size of $\sim 1 \mu\text{m}$ are formed in situ. In addition, some coarse Al_xTi particles are formed in the composite, too.

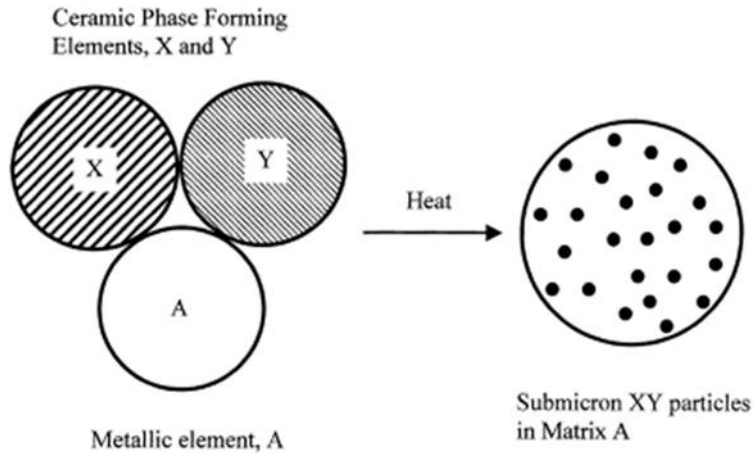


Figure 2.2. Schematic figure for the fabrication XD dispersion-hardened composites. (S. Tjong & Ma, 2000)

2.2.1.2 Reactive Hot Pressing (RHP)

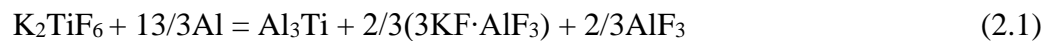
The Reactive Hot Pressing (RHP) process has been developed by Z. Y. Ma et al. (1993) for the fabrication of AMCs reinforced with TiB_2 particulates. It encompasses both the exothermic conversion of reactants to in-situ reinforcements and the subsequent hot compaction of the porous composite product. Thus, dense Al-based composites are produced in one processing step. In this process, stoichiometric Ti and B powders of TiB_2 , and an appropriate amount of Al powders, are blended thoroughly and cold-compacted to a theoretical density of 65%. The as-compacted green billet is heated to above 1073 K in vacuum and maintained for 10 min, then cooled down to 873 K and hot-pressed. This process results in products with a theoretical density of nearly 100%. The dense as-pressed composites can be subsequently subjected to extrusion or rolling. TiB_2 particulates with a size of $0.1\sim 5 \mu\text{m}$ are formed in situ.

2.2.1.3 Flux-Assisted Synthesis

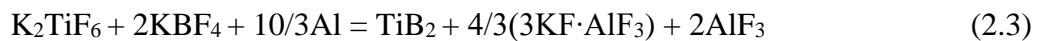
A patented process termed Flux-Assisted Synthesis (FAS) (also known as mixed-salt reaction or reaction cast) was developed by the London Scandinavian Metallurgical Company (LSM) to produce in-situ aluminum matrix composites. The reaction of fluoride salts at a low melt temperature (750~800 °C) utilizes an exothermic reaction, as shown in Fig. 2.3. Fluoride salts reaction is advantageous in achieving a clean melt. Besides, the reaction products and unreacted salt float on the melt and then can be easily removed from the melt. This is a very simple and economic technique, which is limited to a low volume fraction of reinforcement particles. The maximum amount of reinforcements which can be dispersed into the melt depends on the viscosity of the melt (S. Tjong & Ma, 2000).

Al₃Ti can be synthesized in-situ via FAS, too. In this method, only K₂TiF₆ salt is added into an Al melt to obtain Al₃Ti as the reaction product (Reaction 2.1). The melt is normally stirred for a complete reaction. Ultrasonic vibration can be applied for a better distribution of the reinforcing particles throughout the molten metal (C. Yang et al., 2018). After the removal of slag, the Al₃Ti/Al melt is poured into a permanent mold to form a PRAMC casting.

Another production route is achieved by adding pure Ti powders into an Al melt which leads to Reaction 2.2. Al₃Ti will first form at the surface of Ti powder and Al₃Ti particles at the reaction layer will be rapidly peeled off in the liquid Al. The reaction will continue through the Ti powders until the completion of Reaction 2.2. (Z. W. Liu et al., 2014).



In-situ TiB₂ is commonly synthesized via the mixed salt-metal reactions. Mixed K₂TiF₆ and KBF₄ salts are added into an Al melt for Reaction 2.3. The reaction temperature is typically set at 850 °C and the reaction is allowed to continue for 15 to 60 minutes with mechanical stirring (X. Liu et al., 2017; M. Wang et al., 2014). After the removal of the slag, the melt is poured into a permanent mold to produce a casting ingot.



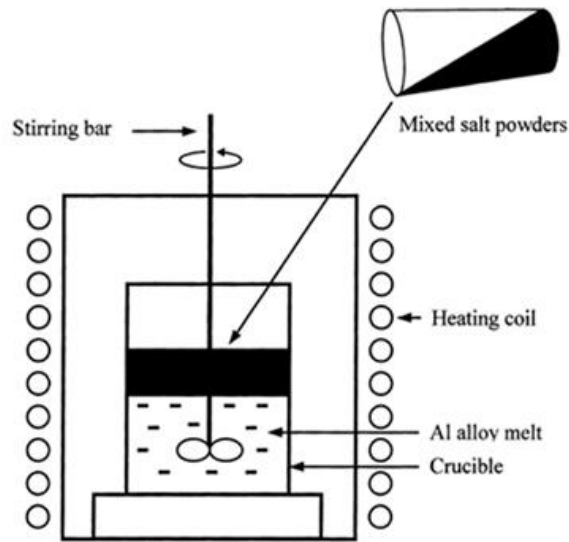


Figure 2.3. Schematic figure showing an apparatus of fabricating in-situ MMCs by flux-assisted synthesis. (S. Tjong & Ma, 2000)

2.2.2 Solid–Solid Reaction Process

Mechanical Alloying (MA) is a solid state powder processing method which involves repeated cold drawing and fracturing of particles as a result of high energy ball-sample collisions. Fine-grained alloy powders can be produced in metal-metal and metal-ceramic systems. The master alloys by mechanical alloys are much more effective compared to conventional Al-Ti and Al-Ti-B master alloys, attributed to the formation of nanocrystalline Al_3Ti and TiB_2 particles, which enhance the grain refining efficiency. However, the disadvantages of MA are high production cost and low production rate. Examples are the work that were done by Basiri Tochae et al. (2016) and Tahamtan et al. (2014). An in-situ powder metallurgy technique of fabricating near net shape particulate $\text{Al}_3\text{Ti}/\text{Al}$ composite is developed. Al_3Ti particles are generated in aluminum matrix by solid state reactive diffusion of homogenous blended pure Ti and Al powders. After 5 h sintering at $600\text{ }^\circ\text{C}$, Al_3Ti intermetallic particles are formed as the reinforcing phase.

A recent work has proposed a novel method for the fabrication of in-situ $\text{Al}_3\text{Ti}/\text{Al}$ composites (Hsu et al., 2006). In the work, aluminum reinforced with a large amount of in-situ Al_3Ti particles are fabricated from Al-Ti elemental powder mixtures via friction stir processing (FSP). The method combines the hot working nature of FSP and the exothermic reaction between Al and Ti. It shows that FSP can provide severe deformation to promote mixing and refining the

constituent phases in the material. Moreover, elevated temperature is applied to facilitate the formation of in-situ Al_3Ti . The products have a submicron-grained structure and nanometer-sized in-situ Al_3Ti particles.

Another work by Safiri et al. (2019) illustrates a fabrication method of Al- Al_3Ti Composite via in-situ Accumulative Roll Bonding (ARB). Ti particles are dispersed throughout Al foils by accumulative roll bonding. The reaction between the particles and the matrix is then activated thermally by post-rolling annealing. The in-situ reaction is promoted by mechanical activation by ARB and thermal activation due to annealing. The obtained composites show that the majority of faceted particles become spherical in shape at high temperatures during the annealing process. Particles are refined to as small as 250 nm.

2.3 Mechanical properties of PRAMCs

PRAMCs are promising as structural materials with the combinations of physical and mechanical properties of the matrix and the reinforcements, which are not achievable with monolithic alloys.

2.3.1 Tensile Behavior

For the PRAMCs, the introduction of reinforcement particles can generally increase the elastic modulus (E) and strength (YS and UTS). But the ductility is typically lower than the unreinforced aluminum matrix. And in general, with an increase in volume fraction, higher elastic modulus, yield and tensile strengths are observed, because of load transfer to the reinforcements. The work hardening rate increases with increasing volume fraction of reinforcement, too (X. Gao et al., 2020). However, the ductility becomes lower. The tensile elongation decreases rapidly with the addition of reinforcing particles. It is suggested that the low ductility of the composites is associated with particle cracking, especially with coarse particle size. Moreover, particle agglomeration also leads to a significant decrease in the elongation since a high stress concentration is generated within those areas. Microstructurally, the reinforcing particles contribute to the earlier onset of void nucleation and accelerating the coalescence of voids, resulting in a low ductility compared to the unreinforced matrix. The rather limited ductility is a major problem of the mechanical properties of composites (Chawla & Shen, 2001).

Additionally, it should be noted that the mechanical properties of PRAMCs are microstructural-dependent. The particle size is an influential factor. According to related work (Chawla et al., 1998; Manoharan & Lewandowski, 1992), the effect of particle size on tensile behavior indicate an increase in ductility with a decrease in particle size. Particle fracture is more prevalent in coarser particles. Moreover, tensile properties increase with the decrease of particle size due to the increase of particle fracture strength with the decrease of particle size (Ghosh & Moorthy, 1998; S. Ma et al., 2019), since larger particles possess a higher possibility of having defects inside. Furthermore, a smaller particle size can also enhance the contributions of different strengthening effects by the reinforcements. Another microstructural factor is the homogeneity of composite materials. A uniform distribution of reinforcement in PRAMCs is essential to achieve effective strengthening, while non-uniform distribution of reinforcement could result in lower ductility, strength and toughness of the composites (Mishnaevsky et al., 2004; Z. Wang et al., 2011).

2.3.2 Other mechanical properties

Apart from the tensile properties. Other mechanical properties of PRAMCs associated to the addition of the reinforcement are shown briefly as follows.

Hardness: It is discovered that as the increased content of reinforcements in the matrix material, the hardness of the composites is also increasing, due to the high hardness of the ceramic particles (G. B. V. Kumar et al., 2011).

Wear property: It is well known that the aluminum alloys exhibit poor wear resistance owing to their softness. Generally, ceramic reinforcing particles have a beneficial effect in improving the wear resistance of aluminum alloys. The PRAMCs typically have better wear resistance than the unreinforced matrix alloys (Nofar et al., 2009).

Fracture toughness: The fracture toughness of PRAMCs is decreased with the increase of reinforcement, mirroring to some extent the tensile elongation, which is decreasing with increasing reinforcement (Kurşun et al., 2016).

Creep Behavior: In general, the addition of a high stiffness reinforcement greatly increases the creep resistance over the unreinforced alloy (Chawla & Shen, 2001).

Fatigue Behavior: The monolithic aluminum alloys have inadequate fatigue resistance for many applications. The addition of a high stiffness particulate ceramic reinforcement results in a

substantial increase in fatigue resistance (G. B. V. Kumar et al., 2011). Chawla & Shen (2001) also suggest that low cycle fatigue behavior of PRAMCs to be somewhat worse than unreinforced alloys due to the lower ductility of the composites, whereas the high cycle performance is improved because of the higher modulus.

2.3.3 Ex-situ vs In-situ

The homogeneity of composite materials is of crucial importance for high-performance engineering applications such as those in the automotive and aircraft industries. Compared to ex-situ PRAMCs, in-situ PRAMCs are advantageous with a uniform distribution of particles, fine of the matrix, clean interface and stronger interface bonding between the reinforcement and the matrix. As a result, it is believed that the in-situ PRAMCs possess superior mechanical properties than the ex-situ PRAMCs.

The tensile properties of in-situ and ex-situ TiB_2/Al MMCs are compared by Kuruvilla et al. (1990). Their results show that the strength, modulus and hardness of the in-situ TiB_2/Al composite are much higher than that of in the ex-situ composite, although the ex-situ composite exhibits considerably improved properties compared to unreinforced aluminum alloys. The tensile and yield strengths of the in-situ TiB_2/Al composite are twice as high as that of the ex-situ composite. Moreover, the modulus of the in-situ composite is almost double that of unreinforced matrix. It is suggested that the enhanced mechanical properties of the in-situ composite are mainly attributed to the uniform dispersion of the high modulus TiB_2 particles and their well bonding to the matrix.

AMCs reinforced with in-situ TiB_2 are expected to exhibit better wear performance than those reinforced with SiC or Al_2O_3 particles. It is found that TiB_2 particles formed in-situ in metal matrices have a strong particle-matrix bonding. Therefore, it reduces the pull-out of particles from the AMCs during sliding. It is also noted that the in-situ PRAMCs, particularly the composites reinforced with TiB_2 particles, exhibit higher strength, modulus, creep and wear resistance than conventional ex-situ composites (S. Tjong & Ma, 2000).

Table 2.1 compares the mechanical properties of AMCs reinforced with in-situ Al_3Ti and TiB_2 particles from published work. Both YS and UTS are enhanced effectively by the reinforcements. The strength is generally increased with the increase of particle fraction. For elongation, in general, the elongation decreases with the increase of the content of particle.

However, some research work show that the elongation goes up with the increase of particle amount in Al₃Ti reinforced composites, especially for the composites treated by ultrasound during casting, which refines the grain size and disperses particles more uniformly, therefore the ductility is improved simultaneously with strength.

Table 2.1. Mechanical properties of PRAMCs with in-situ Al₃Ti and TiB₂ reinforcements from related researches.

Materials	Treatment	YS /MPa	UTS /MPa	Elongation /%	Refs.
T6-A356		195	228	1.95	Z. Liu et al. (2018)
T6-A356/1.5 wt.% Ti	Casting	225	282	3.44	
T6-A356/3.0 wt. % Ti		252	310	4.73	
Al6061		59	130	7.7	Gupta et al. (2018)
Al6061/2.7wt. %Al₃Ti	Ultrasonic	66	175	13.8	
Al6061/5.4 wt. %Al₃Ti	assisted casting	74	188	16.5	
Al6061/8.1wt.% Al₃Ti		84	208	23.5	
A356		113	207	6.6	S. Ma & Wang, (2019)
A356/5vol.%Al₃Ti	Casting	124.6	210.2	3.6	
T6-A356		216.3	283.5	6.7	
T6-A356/5vol.%Al₃Ti		229.2	280.5	5.3	
A356		199.8	232	11.1	M. Wang et al. (2014)
A356/2.12vol.%TiB₂	As-cast	209.4	235.4	7.81	
A356/4.66vol.%TiB₂		212.8	252.1	7.36	
A356/8.37vol.%TiB₂		217.6	258.5	2.73	
A356		246.2	326.2	13.91	
A356/2.12vol.%TiB₂	T6	304.7	375.3	4.88	
A356/4.66vol.%TiB₂		317.4	377	1.9	
A356/8.37vol.%TiB₂		347.4	391.9	1.32	

2.4 Strengthening Mechanisms

The Young's modulus of PRMMCs can be agreeably predicted with the Tsai-Halpin Equation as Eq. 2.4, which is associated with the Young's modulus and volume fraction of particles (Halpin & Kardos, 1976).

$$E_c = \frac{E_m(1+2s\eta V_p)}{(1-\eta V_p)} \quad (2.4)$$

The parameter η is calculated by the following equation (Eq. 2.5).

$$\eta = \frac{E_p/E_m - 1}{E_p/E_m + 2s} \quad (2.5)$$

Where E_p and E_m are the Young's modulus of reinforcing particles and matrix, respectively. s is the average aspect ratio of particles. V_p is the volume fraction of particles.

YS and UTS are enhanced due to the addition of reinforcing particles. Typical strengthen mechanisms of PRAMCs could be concluded as follows (Hsu et al., 2006; M. Wang et al., 2014):

1. Thermal expansion coefficient (CTE) mismatch strengthening due to the mismatch of thermal expansion coefficient between matrix and reinforcements.
2. Orowan strengthening via dispersed particles in the matrix. If particles are small enough in size and dispersed uniformly, this effect will be enhanced.
3. Grain boundary strengthening through the Hall-Petch relation. Generally, if the grain size is small, the effect will be enhanced.
4. Load-bearing strengthening through strong particle-matrix interfacial bonding.

The yield strength is greatly influenced by the microstructural features of the composites. Micromechanically, the contributions of each strengthening mechanism by the introduction of particles, including load bearing strengthening $\Delta\sigma_{\text{Load}}$, grain refinement strengthening $\Delta\sigma_{\text{gf}}$, CTE mismatch strengthening $\Delta\sigma_{\text{CTE}}$, and Orowan strengthening $\Delta\sigma_{\text{Orowan}}$, can be estimated as follows.

Load bearing strengthening ($\Delta\sigma_{\text{Load}}$) attributes to load transfer to the reinforcements from the matrix, resulting in improved YS in composites. The in-situ particles, such as Al_3Ti , and TiB_2 ,

which form strong bonding to the matrix, the strengthening effect of $\Delta\sigma_{\text{Load}}$ can be calculated by Eq. 2.6. (Kim et al., 2013; Ramakrishnan, 1996; Sekine & Chent, 1995)

$$\Delta\sigma_{\text{Load}} = 0.5sV_p\sigma_m \quad (2.6)$$

where σ_m is the YS of aluminum matrix, s and V_p is aspect ratio and the volume fraction of the reinforcement particles, respectively.

CTE mismatch strengthening refers to geometrically necessary dislocations accommodating the mismatch in coefficient of thermal expansion between reinforcements and matrix during cooling. The increased dislocation density gathered at the interfacial zones provides addition strengthening as shown in Eq. 2.7: (Kapoor et al., 2010)

$$\Delta\sigma_{\text{CTE}} = \beta G_m b \sqrt{\rho^{\text{CTE}}} \quad (2.7)$$

where β is a constant; G_m is the shear modulus of the matrix; b is the Burgers vector of the dislocations; and ρ^{CTE} is the dislocation density from CTE mismatch, estimated by the Eq. 2.8. (S.-Z. Lu & Hellawell, 1995)

$$\rho^{\text{CTE}} = \frac{A\Delta\alpha\Delta T V_p}{bd_p(1-V_p)} \quad (2.8)$$

where E_m and ν are Young's modulus and Poisson's ratio of the alloy matrix respectively; A is a constant; $\Delta\alpha$ is the CTE difference between the matrix and reinforcements; ΔT the difference between processing and room temperature; V_p is the volume fraction of reinforcing particles; and d_p is the average size of particles. From Eqs. 2.7 and 2.8, smaller-sized particles show more effective CTE mismatch strengthening.

The grain size of aluminum alloys can also be refined by the introduction of reinforcements acting as heterogeneous nucleation sites. The strengthening effect of grain refinement is generally expressed by Hall-Petch relationships as Eq. 2.9, where k is the Hall-Petch coefficient, d is the average grain size of the composites and d_0 is the average grain size of the original alloy matrix (Pande & Cooper, 2009).

$$\Delta\sigma_{gf} = k \left(d^{-\frac{1}{2}} - d_0^{-\frac{1}{2}} \right) \quad (2.9)$$

The Orowan strengthening effect arises from the interaction between reinforcements and the motion of dislocations in the matrix. In general, the particle size should be smaller than 1 μm to activate this mechanism. The Orowan-Ashby equation (Sanaty-Zadeh, 2012) is used to describe this strengthening effect. (Eq. 2.10)

$$\Delta\sigma_{Oro} = \frac{0.4MG_m b \ln(\sqrt{\frac{2}{3}}d_p/b)}{\pi\lambda \sqrt{1-\nu}} \quad (2.10)$$

where M is the mean orientation factor. λ is interparticle spacing, related to the particle size and fraction by Eq. 2.11.

$$\lambda = \sqrt{\frac{2}{3}}d_p \left(\sqrt{\frac{\pi}{4V_p}} - 1 \right) \quad (2.11)$$

The contribution from each mechanism above can be summed up to obtain the final yield strength of the composites as Eq. 2.12.

$$\sigma_c = \sigma_m + \Delta\sigma_{Load} + \Delta\sigma_{CTE} + \Delta\sigma_{gf} + \Delta\sigma_{Oro} \quad (2.12)$$

Based on the strengthening mechanisms above, it is expected that the mechanical properties of PRAMCs can be improved with the refinement of particle size and distribution. Following the guidance, numerous research works have been conducted in producing in-situ PRAMCs with enhanced mechanical properties, such as high strength and improved ductility. Several strategies have been proposed, such as ultrasonic treatment of melt, precipitation strengthening by heat treatment, adding alloying elements, secondary mechanical processing and etc.

In the solid-liquid reaction processes, such as FAS, it is crucial to disperse the salt into the melt uniformly for complete reaction. As a result, effective melt stirring is necessary. Z. Liu et al.

(2018) and C. Yang et al. (2018) have applied ultrasonic treatment (UST) to the melt to assist dispersing the solid phase (Ti powder or salt) and obtaining the in-situ $\text{Al}_3\text{Ti}/\text{A356}$ composites. Their results show that the ultrasonic treated $\text{Al}_3\text{Ti}/\text{A356}$ composites achieve high strength and elongation compared to the untreated composites. Microstructurally, the particle size is refined and particles are more uniformly distributed with UST.

Heat treatment is widely applied in heat-treatable aluminum alloys. The yield strength and ultimate strength can be effectively enhanced by precipitation strengthening. For the PRAMCs with heat-treatable aluminum alloy matrices, heat treatment can be also applied as same as for the monolithic alloys, as reported in $\text{TiB}_2/\text{A356}$ (M. Wang et al., 2014) and $\text{Al}_3\text{Ti}/\text{A356}$ composites (S. Ma & Wang, 2019).

Several alloying elements play an effective role in enhancing the mechanical properties of Al alloys, such as Sr, Sc, rare earth elements etc. For instance, Sr can refine the eutectic Si phase in A356 alloy and result in the improvement of mechanical properties (Timpel et al., 2012; Q. G. Wang & Davidson, 2001). Sc acts as nucleation zone for Al alloys by forming Al_3Sc primary phase and refine the grain size. Moreover, heat treatment can precipitate Al_3Sc , providing further enhancement of the mechanical properties (Pramod et al., 2015; K. Yu et al., 2004). As a consequence, such alloying elements are expected to play a similar role in the in-situ PRAMCs. For example, Garcia-Hinojosa et al. (2004) have studied the effect of Sr addition on an Al–7Si–10 vol.% SiC_p cast composites, showing the refinement of Si phase with Sr addition. Pramod et al. (2015) studied the effect of Sc on the properties of in-situ $\text{TiB}_2/\text{A356}$ composites. Their results show that Sc modifies the eutectic Si. Sc addition refines the grain size and increases the hardness of in-situ $\text{TiB}_2/\text{A356}$ composites.

Secondary mechanical processing is also widely applied for the improvement of the performance of Al alloys, such as rolling, extrusion and other deformation methods. For the PRAMCs, due to their isotropic property, they can be typically deformed as same as for the Al alloy matrices. With secondary mechanical processing, the porosity of the PRAMCs can be reduced. Besides, the particles can be made into a finer size and distribution due to the plastic deformation. The plastic deformation also results in work hardening of the Al matrix. As a result, the microstructure of the PRAMCs is refined and the mechanical properties are enhanced accordingly. For instance, S. M. Ma et al. (2014) have studied the effect of friction stir processing (FSP) on the microstructure and mechanical properties of a $\text{TiB}_2/\text{Al-Mg-Si}$ composite. It is

indicated that the friction stir processing refines the grain size and the distribution of TiB_2 and therefore evidently improves the yield and tensile strengths of the composites. R. V. Kumar et al. (2018) have studied the influence of hot rolling on the microstructure and mechanical behavior of Al6061-ZrB₂ in-situ metal matrix composites. Their results also conclude that a hot rolled composites displayed improvement in ductility and strength when compared with that of as-cast counterparts.

2.5 Micromechanical simulation of PRMMCs

From above sections, it is acknowledged that the mechanical properties of PRMMCs are related closely to the microstructural characteristics. To investigate the microstructure-property relationship of PRMMCs, experimental, analytical and numerical simulation methodologies can be employed (J. Zhang et al., 2016). Numerical simulations are conducted by microstructure-based models, in which the microstructural features of the composites are considered parametrically, such as size, fraction, distribution, morphology of the reinforcing particles. Compared to the experimental and the analytical methods, numerical simulation is advantageous for the following reasons: Firstly, it reduces the cost from mechanical tests greatly. In addition, the influence of reinforcement characteristics, such as size, fraction, distribution, morphology, can be investigated parametrically. Moreover, the details of microscale stress–strain fields and damage evolution are accessible via numerical models (Qing, 2013a).

The numerical modeling of PRMMCs can be realized by using unit cell model (Eckschlager & Han, 2002; Sung et al., 2009) or representative volume elements (RVE) model containing multiple particles (S. Ma et al., 2019; Qing, 2013b). Representative volume element (RVE) refers to a volume large enough to be statistically representative of the microstructural features of PRMMCs, such as particle size, fraction, morphology and distribution, while also small enough to be considered as a volume element of continuum mechanics (Kanit et al., 2003). In addition to experimental study, microstructure-based simulations show a great potential in predicting the mechanical properties of materials based on RVE models. Generally, the RVE models with multiple particles can provide more accurate and detailed results for the simulation of PRMMCs, compared to the unit cell models, though the unit cell model is easy to generate.

The geometry of multi-particle RVE models can be generated based on realistic microstructure (Jagadeesh & Setti, 2020) or computationally with the RVE generation software.

The multi-particle RVE models are subsequently submitted to numerical calculation, such as finite element modelling (FEM) (Chawla et al., 2004; Jagadeesh & Setti, 2020; Qing, 2013b). Finite element (FE) micromechanical simulations on the microstructure-based RVE have been widely adopted to study the mechanical behavior of multiphase materials, such as dual-phase steels (DPs) and metal matrix composites (Qing, 2013a; Ramazani, Pinard, et al., 2013; Sun et al., 2009). With FE micromechanical simulations, microscale stress–strain fields and damage evolution can be accessed during a loading process (Qing, 2013a). Fig. 2.4 shows some examples of multi-particle RVE models for micromechanical simulation.

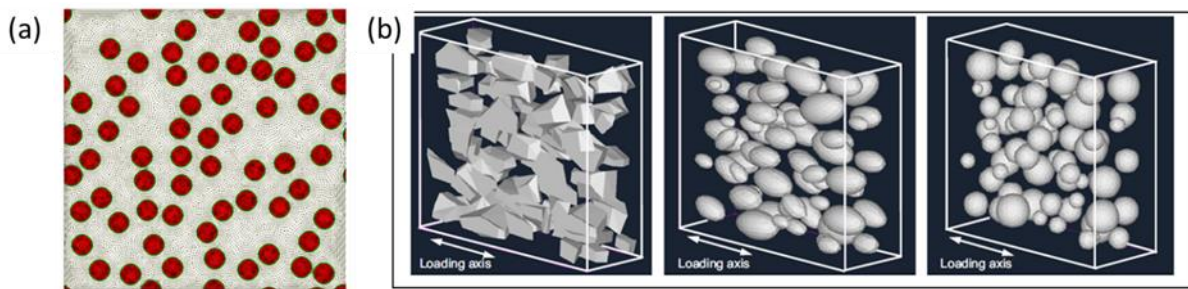


Figure 2.4. (a) 2D multi-particle RVE model with round inclusions (Qing, 2013b); (b) 3D multi-particle RVE models with different particle morphology (Chawla et al., 2006).

Typical procedure for micromechanical simulations of the microstructure-based RVE by FEM is shown briefly in the flow chart as Fig. 2.5. The first step is the generation of RVEs. Two-dimensional (2D) and three-dimensional (3D) RVEs can be adopted for the FE simulation. 2D simulation is more attractive than 3D for less time requirement for calculation. However, it cannot be fully representative of the 3D structure and stress-strain states. Therefore, the mechanical properties of composites are not precisely predicted. In comparison, simulations with 3D RVE show a higher accuracy according to related works (Ramazani, Mukherjee, Quade, et al., 2013; Saraev & Schmauder, 2003).

Subsequently, the constitutive behaviors are given to the constitution (matrix, reinforcements and interface), including the elastic and/or plastic deformation behaviors and damage behaviors. Then the model geometric and constitutive behaviors are input into the FE software for meshing. For 2D simulation, plane strain or plane stress type elements are typically applied (Zhou et al., 2015), while for 3D simulation, 3D cubic or tetrahedron elements are commonly used. It should be noted that the mesh density is quite influential on the results of the

simulation until mesh density is large enough. Therefore, the mesh density dependence should be conducted in the RVE simulation. Finally, loading and boundary conditions (BCs) are exerted on the RVE model to simulate the deformation of the composites. The boundary conditions (BCs) used on RVE involve symmetrical boundary condition (SBC), homogenized boundary condition (HBC) and periodic boundary condition (PBC) from literatures (G. Chen et al., 2018; Qing, 2013a).

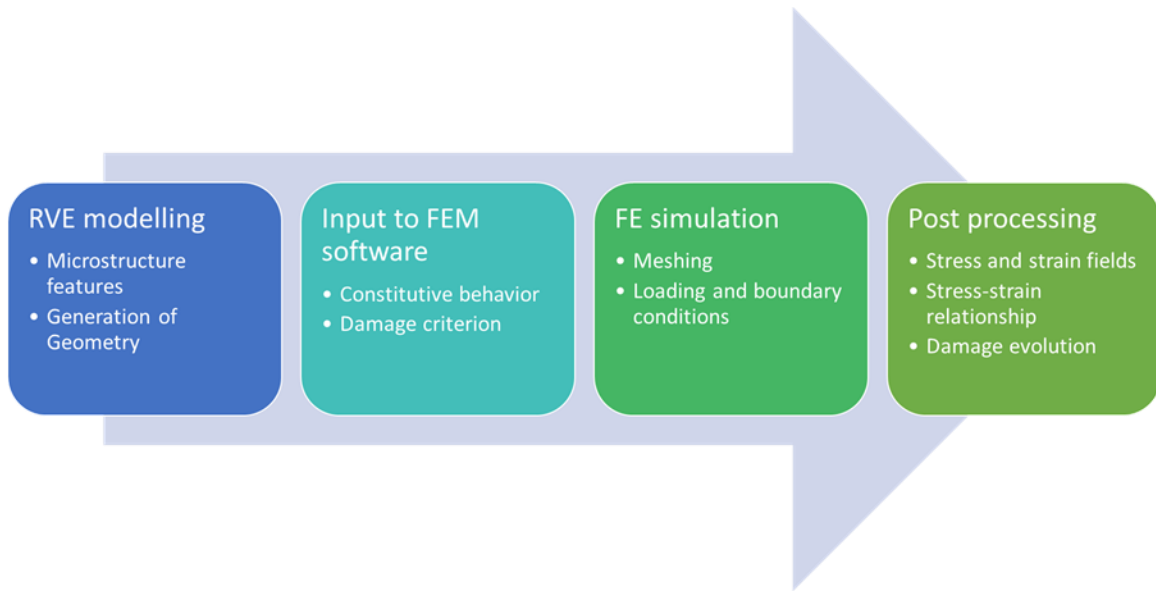


Figure 2.5. Flow chart showing typical procedure for micromechanical simulations on the microstructure-based RVE by FEM.

There are numerous simulation work focusing on the mechanical properties of PRAMCs with microstructure-based RVE models. For instance, Qing (2013a) has conducted a 2D RVE simulation on the mechanical properties of PRAMCs, which involves the constitutive behavior and damage mechanisms of matrix, particles and their interfaces. The effect of boundary conditions on the simulation results are also included.

J. Zhang et al. (2016) have simulated the deformation and damage processes of SiC_p/Al composites under tension. The RVE is based on a 3D realistic microstructure. The fracture of Al matrix, SiC particles and their interfaces are modelled. The simulation results show a satisfactory prediction of the tensile behavior of the composites.

Weng et al. (2019) have conducted a thorough study on the effects of interface damage, particle size and morphology on tensile behavior of particle reinforced composites with 3D multi-

particle FE model. They have adopted strain-gradient plasticity to evaluate the size-dependent strengthening effect on matrix, which shows a good agreement with experiments when consistent geometrical and material parameters are used.

2.6 Summary

This chapter presents a review of literatures on the in-situ PRAMCs. An overview of in-situ PRAMCs about its definition, features and application is made, especially for AMCs with Al_3Ti and TiB_2 particle reinforcements. Then typical fabrication methods of the in-situ PRAMCs are introduced, involving solid–liquid and solid–solid reaction processes. The mechanical properties of PRAMCs are summarized, such as the strength, stiffness, ductility and other properties. Subsequently, the strengthening mechanisms by the particle reinforcements are introduced. Based on these mechanisms, several strategies for enhancing the mechanical properties of the PRAMCs are proposed according to literature. Finally, a micromechanical simulation method is introduced in order to investigate the microstructure-properties relationship of PRAMCs. A brief flow chart for micromechanical simulation with microstructure-based RVE models is illustrated. This chapter introduces the basic knowledge and also indicates potential methodologies for obtaining high strength in-situ PRAMCs.

CHAPTER 3. FRAMEWORK AND METHODOLOGY

This chapter involves the framework and methodology associated with the fabrication, the mechanical properties and microstructures of the PRAMCs in this study. The experiment design, the material characterization methods and the micromechanical simulation methods will be demonstrated in this chapter.

3.1 Research Approach

An in-situ $\text{Al}_3\text{Ti}/\text{A356}$ composites and an in-situ $\text{TiB}_2/\text{Al2618}$ composites are taken as two examples to investigate their mechanical properties and microstructures, aiming to obtain in-situ PRAMCs with high strength and enhanced mechanical properties. $\text{Al}_3\text{Ti}/\text{A356}$ and $\text{TiB}_2/\text{Al2618}$ composites will be fabricated in-situ via melt-salt reactions. Rolling deformation will be done on the $\text{TiB}_2/\text{Al2618}$ composites, as Al2618 is a wrought alloy. The as-cast $\text{Al}_3\text{Ti}/\text{A356}$ composites or $\text{TiB}_2/\text{Al2618}$ composites will be heat treated to investigate the effects of heat treatment.

The samples of the investigated composites will undergo tensile test and hardness test to characterize their mechanical properties. The microstructures of the samples will be characterized by X-ray Diffraction (XRD), Optical Microscopy (OM), Scanning Electron Microscopy (SEM), and Transmission Electron Microscopy (TEM).

Micromechanical simulation will be conducted to investigate the microstructure-properties relationship of PRAMCs. RVE models based on the microstructure of the in-situ $\text{Al}_3\text{Ti}/\text{A356}$ composites in this study will be generated. The models will be submitted to the finite element simulation software ABAQUS for simulation.

3.2 Materials Preparation

3.2.1 In-situ synthesis

For the fabrication of in-situ $\text{Al}_3\text{Ti}/\text{A356}$ composites, K_2TiF_6 salt is added into an A356 aluminum melt for Reaction 2.1. The targeting amount of in-situ Al_3Ti reinforcing particulates is 5 vol. %. The temperature for reactions is set as 780 °C, aiming to synthesize small-sized blocky Al_3Ti particulates. The temperature is measured by a K-type thermocouple. The melt is stirred

mechanically by a graphite rod for 10 min for a complete reaction. An Al-10 wt. % Sr master alloy is added subsequently into some of the melts to introduce 0.02 wt. % Sr (200 ppm) with a holding time of 30 min to study the effects of Sr on the composites. After removing the slag completely, approximately 0.5 wt. % pure magnesium is added into the melt to replenish the loss of Mg by forming MgF_2 during salt-aluminum reactions. Then the $Al_3Ti/A356$ melts (with or without Sr addition) are poured into a preheated ($250\text{ }^\circ\text{C}$) permanent steel mold at $730\text{ }^\circ\text{C} (\pm 10\text{ }^\circ\text{C})$ and cooled down to room temperature in air.

In-situ $TiB_2/Al2618$ composites are produced via chemical reactions of a mixture of KBF_4 and K_2TiF_6 salts with the alloy melt in an induction furnace at $730\text{ }^\circ\text{C}$ for 30 min. The melt is stirred by electromagnetic field and the slag is removed. The particle weight percentage (wt. %) are set as 0 % (with no salt addition), 4 % or 8 % (noted as Al2618, C4, and C8, respectively). Then the alloy and composite ingots are remelted at $780\text{ }^\circ\text{C}$ in an electrical resistance furnace and poured at $730\text{ }^\circ\text{C}$ into a preheated steel mold ($400\text{ }^\circ\text{C}$) with a cavity dimension of $120\text{ mm} \times 20\text{ mm} \times 6.7\text{ mm}$. The cast sheets are prepared for additional rolling.

3.2.2 Rolling

A laboratory rolling mill is employed for hot rolling process as shown in Fig. 3.1. The cast sheets of in-situ $TiB_2/Al2618$ composites are annealed at $480\text{ }^\circ\text{C}$ for 1 h in the heat treatment oven in Fig. 3.2. Then the sheets are taken out and immediately subjected to rolling in one direction. The thickness reduction of each pass is approximately 0.5 mm. The final thickness of the sheets after rolling is set as $4.2 \pm 0.1\text{ mm}$ and $2.0 \pm 0.1\text{ mm}$, equivalent to 35 % and 70 % thickness reduction (noted as R35 and R70) by multiple passes. The sheets are annealed at $480\text{ }^\circ\text{C}$ for 10 min between the passes for reheating.



Figure 3.1. The laboratory rolling mill for rolling process.



Figure 3.2. Heating oven for heat treatment of the samples.

3.2.3 Heat treatment

All the heat treatment of the composites is conducted in the heat treatment oven (Lindberg Blue M, Thermo Scientific Co.) in Fig. 3.2. For the in-situ $\text{Al}_3\text{Ti}/\text{A356}$ composites, a T6 heat treatment is conducted on a portion of as-cast samples as the following procedure: solution treatment $540\text{ }^\circ\text{C}$ for 4 h and quenching into room temperature water ($25\text{ }^\circ\text{C}$), followed by artificial aging at $155\text{ }^\circ\text{C}$ for 6 h. For the as-rolled in-situ $\text{TiB}_2/\text{Al2618}$ composites, the heat treatment is

conducted with the following steps: solid solution at 530 °C for 5 h and water quenched, followed by an artificial aging for 20 h at 195 °C.

3.3 Mechanical Properties Characterization

The mechanical properties of the investigated composites are evaluated by uniaxial tensile test. The Al₃Ti/A356 composites are casted in a permanent steel mold made for producing dog-bone shape samples for tensile tests. The dog-bone shaped ingots are ground and polished to a rectangular gage section with the section area of 6 mm ×6 mm, according to the ASTM-B557M standard (ASTM-B557M, 2015). The gauge length is 25.4 mm. The as-rolled and heat-treated TiB₂/Al2618 composites sheets are cut into dog-bone shaped tensile samples along the rolling direction. The gauge length is 25.4 mm and the width is 6 mm. The thickness is remained as the rolling thickness. For all samples, uniaxial tensile tests are conducted on an ATS-900 machine at room temperature with a strain rate of 10⁻³ s⁻¹. A minimum number of three samples are tested repeatedly for each as-cast or heat-treated samples.

3.4 Microstructure Characterization

3.4.1 X-ray Diffraction

In order to identify the phases in the composite samples. X-ray diffraction is conducted on the samples with a Bruker-D8 Focus Machine. The tests are conducted with a Cu-K radiation by a scan step of 0.02° in the 2θ range of 20° ~ 90°. The samples are polished for testing. After obtaining the diffraction patterns, the peaks are found and indexed by using the corresponding standard patterns to identify the phases.

3.4.2 Optical Microscopy

The microstructures of composites are characterized by using a Leica DM-LM/P optical microscope (OM) with a magnification up to 1000×. For the preparation of the samples, the samples are cut with a hand saw and mounted in Bakelite. Then the sample surfaces are ground gradually by using SiC sand papers with the grit numbers of 180, 400, 1200, 2500. Subsequently, the samples are polished firstly with 1 μm alumina polishing suspension, following by the 0.05 μm

silica polishing suspension. Finally, to reveal a clearer microstructure, some of the samples are etched for 10~20 s by the Keller's reagent (2.5 ml HNO₃, 1.5 ml HCl, 1.0 ml HF and 95 ml H₂O) and washed by using purified water.

3.4.3 Scanning Electron Microscopy

Scanning Electron Microscopy (SEM) is carried out by using a Quanta 3D field emission scanning electron microscope (FESEM) equipped with an energy dispersive X-Ray spectrometer (EDS), intending to observe the microstructures of the composites with large magnification ($\geq 1000\times$). The samples are ground and mechanically polished for backscattered electron (BSE) analysis under SEM to reveal the distribution of reinforcing particulates and intermetallic phases. Besides, Keller's reagent is applied to etch the polished samples for secondary electron (SE) analysis under SEM to observe the morphologies of constitutive phases. The EDS analyses are conducted for point and mapping analyses of the elements in the composite samples with the Aztec software.

3.4.4 Transmission Electron Microscopy

Transmission Electron Microscopy (TEM) is conducted for observing the details of the Al-Ti-Si ternary intermetallic phases in the Al₃Ti/A356 composites with higher magnification than SEM. TEM foils are prepared from a polished Al₃Ti/A356 composite sample with a scanning electron microscope (SEM) and dual focused ion beam (FIB) (Helios Nanolab DualBeam, FEI). The final cleaning step is performed with a beam current of 50 pA and a voltage of 10 keV to minimize FIB-induced damage. The FEI Titan 80-300TM equipped with a monochromator, an image aberration corrector, and a PHENIX energy dispersive X-ray spectrometer (EDS), has been used to characterize the phase structure and chemical distribution. The combined error of EDS analysis is limited to $\pm 0.5\%$. TEM bright field images, scanning transmission electron microscopy (STEM) high-angle annular dark-field (HAADF) images and high-resolution transmission electron microscopy (HRTEM) images are taken to reveal the microstructure of the sample. Fast Fourier Transform (FFT) of different areas in the HRTEM images, as well as interplanar crystal spacing measurement are conducted by using the Digital MicrographTM software. Electron

diffraction patterns are simulated using CryTBox software for indexing phases, by taking crystal structures and lattice parameters from references (Klinger, 2017).

3.4.5 Quantitative Image Analysis

Quantitative image analysis is conducted using the Image J software to obtain the size distribution and the morphology features of the reinforcing particles. The average grain sizes of α -Al grains in different samples are measured according to a line interception method according to the ASTM-E112 standard (ASTM-E112, 2013). For the as-cast samples, the average grain size $\bar{D} = 1.5\bar{l}$, \bar{l} is the average line interception length.

3.5 Thermodynamic Calculations

To help understanding the formation of Al-Ti-Si ternary intermetallic phases in the Al₃Ti/A356 composites through heat treatment, thermodynamic calculations of Al-Si-Ti system are carried out by using Pandat softwareTM. With the updated Al-Si-Ti database in the software, isothermal sections of Al-Si-Ti ternary system can be calculated at a certain temperature. Additionally, the evolution of phase fractions can be simulated under an equilibrium condition and Scheil condition, respectively, given a certain element composition.

3.6 Finite Element Modelling

A three-dimensional (3D) micromechanical simulation will be conducted by using the ABAQUS finite element simulation software, taken the Al₃Ti/A356 composite as an example. 3D RVEs based on the microstructure of the Al₃Ti/A356 composites are geometrically generated by using the RVE generation software Digimat/FE. The geometries of the generated RVEs are input into the Abaqus/CAE software. The constitutive behaviors of the RVE are input through the material module, such as the density, the elastic modulus, work-hardening behavior and the damage properties. Then the RVE models are meshed in the Abaqus/CAE software with the general linear 3D solid elements (C3D4). In the assembly module, the whole RVE is taken as a single assembly. Loading and boundary conditions are exerted on the meshed models via the loading module. The ductile failure and post failure behavior above are realized by using an Abaqus/Explicit subroutine VUSDFLD. Finally, the deformation of the RVE models is simulated

using Abaqus/Explicit under the given loading and boundary conditions. After simulation, the output data can be visualized in Abaqus/CAE, showing the stress, strain fields and damage evolution in RVE models.

3.7 Summary

This chapter outlines the framework and methodologies of this study. In-situ $\text{Al}_3\text{Ti}/\text{A356}$ composites and in-situ $\text{TiB}_2/\text{Al2618}$ composites will be fabricated via the salt-metal methods. The as-cast composites will be subjected to further rolling deformation and/or heat treatment. The mechanical properties of the composites will be evaluated by tensile test and hardness test. The microstructures of the composites will be characterized by X-ray Diffraction (XRD), Optical Microscopy (OM), Scanning Electron Microscopy (SEM), and Transmission Electron Microscopy (TEM). Quantitative image analysis will be conducted to obtain the microstructural features of the composites quantitatively. Thermodynamic calculations will be conducted to help understanding the formation of Al-Ti-Si ternary intermetallic phases in the $\text{Al}_3\text{Ti}/\text{A356}$ composites. Finally, a 3D micromechanical simulation will be conducted by using the ABAQUS finite element simulation software, taken the $\text{Al}_3\text{Ti}/\text{A356}$ composite as an example.

CHAPTER 4. MICROSTRUCTURES AND MECHANICAL PROPERTIES OF IN-SITU Al_3Ti PARTICULATE REINFORCED A356 COMPOSITES

This chapter was reprinted, with journal permission, from Ma, S., & Wang, X. (2019). Mechanical properties and fracture of in-situ Al_3Ti particulate reinforced A356 composites. *Materials Science and Engineering A*, 754(January), 46–56. <https://doi.org/10.1016/j.msea.2019.03.044>

4.1 Introduction

Al-Si type foundry alloys have a broad application in the automotive and aerospace industries due to their excellent castability, superior corrosion and wear resistance in addition to high strengths, particularly after heat-treatment (Lin et al., 2018; Lloyd, 1994; Q. G. Wang & Davidson, 2001). To further improve the modulus and strength of Al-Si alloys for critical structural applications, reinforcing particulates, such as TiB_2 , SiC and Al_3Ti , have been introduced to produce particulate reinforced Al-Si alloy-based composites (Amirkhanlou & Niroumand, 2011; Z. Liu et al., 2018; M. Wang et al., 2014). Amongst the reinforcements, Al_3Ti intermetallic phase is advantageous over others for its low density, high modulus, excellent wettability and, therefore, strong direct bonding to the Al-alloy matrix (R. Gupta et al., 2018; X. Wang et al., 2004; Zeng et al., 2018). Furthermore, Al_3Ti particulates generally exist inside α -Al grains through a peritectic reaction in solidification rather than segregate along the α -Al grain boundaries, resulting in a strong interfacial bonding between the reinforcing particulates and the Al matrix (Z. Liu et al., 2018). The peritectic reaction not only eliminates the degradation of ductility due to the segregation of reinforced particulates at the grain boundaries but also results in the grain refinement of the Al matrix (C. Yang et al., 2018).

In-situ Al_3Ti particulates can be produced by either a K_2TiF_6 -Al reaction route or by the addition of pure Ti powders into an Al melt (Z. Liu et al., 2018; C. Yang et al., 2018). As reported, refining the size and spheroidizing the in-situ Al_3Ti particulates improve the mechanical properties of Al_3Ti particulate reinforced Al composites. However, in general, the in-situ Al_3Ti particulates are large in size ($> 50 \mu\text{m}$) with unfavorable morphology in pure Al, especially when the reaction happened at comparatively high temperatures (H. Yu et al., 2006). Small-sized ($< 5 \mu\text{m}$) in-situ Al_3Ti particles are able to be produced in pure Al at a comparatively low reaction temperature of $730 \text{ }^\circ\text{C}$ (Z. Liu et al., 2012). Meanwhile, it is reported that fine blocky ($\sim 5 \mu\text{m}$) in-situ Al_3Ti

particles were produced in an Al-Si alloy. It is suggested that Si atoms around Al_3Ti nuclei in the melt decrease the diffusion rate of Ti onto the Al_3Ti nuclei, resulting in a reduced growth speed of the Al_3Ti particles (Z. Liu, Wang, et al., 2014). The reactions of Si and Al_3Ti are encountered in both casting and grain refinement practices, undesirably though. The poisoning of Al-Ti-B type master alloys is caused by the presence of Si in Al alloys, evidencing of interactions of Si with Al_3Ti (Tahiri et al., 2018) and the formation of $(\text{Al},\text{Si})_3\text{Ti}$ phase are reported (T. J. Chen et al., 2018; X. Gao et al., 2015; Xiao et al., 2018; C. Yang et al., 2018).

Furthermore, the mechanical properties of Al-Si casting alloys are largely dependent on the size and morphology of eutectic Si phase (Kobayashi, 2000). It has been reported that a small amount (~200 ppm) of Sr modifies coarse plate-shaped eutectic Si into a globular-fibrous morphology (Dahle et al., 2005; Timpel et al., 2012), resulting in an evident enhancement of mechanical properties, especially the elongation (Basavakumar et al., 2008; Closset & Gruzleski, 1982). The beneficial effects of adding Sr are reported applicable to cast SiC/Al-Si composites (Garcia-Hinojosa et al., 2004). It is also revealed that the modification of Al-Si eutectic phase by Sr addition promoted the incorporation of SiC particles in the Al-Si alloy matrix. However, information on the addition of Sr into in-situ $\text{Al}_3\text{Ti}/\text{A356}$ composites is rarely available. It is necessary to understand the effects of Sr addition on the formation and dispersion of Al_3Ti phase, and therefore improving the mechanical properties of the in-situ $\text{Al}_3\text{Ti}/\text{A356}$ composites.

From above, this chapter investigates the experimental works on the fabrication of an in-situ 5 vol. % $\text{Al}_3\text{Ti}/\text{A356}$ composites. The microstructure and mechanical properties of composites are investigated in detail, taking account of the effects of T6 heat treatment and strontium (Sr) addition.

4.2 Experiment

The A356 ingot with a weight of about 500 g was firstly melted in the furnace at 900 °C. K_2TiF_6 salt was added into an A356 aluminum melt, targeting at a 5 vol. % in-situ Al_3Ti reinforcing particulates. The chemical composition of the A356 alloy was Si 7.44, Fe 0.11, Mg 0.31, Ti 0.005 and balanced Al in wt. %. The temperature for reactions was set as 780 °C, aiming to synthesize small-sized blocky Al_3Ti particulates. The melt was stirred mechanically by a graphite rod for 10 min for a complete reaction. An Al-10Sr master alloy was added subsequently into some of the melts to introduce 0.02 wt. % Sr (200 ppm) with a holding time of 30 min to study the effects of

Sr on the composites. After removing the slag completely, approximately 0.5 wt. % pure magnesium was added into the melt to replenish the loss of Mg in the form of MgF_2 during salt-aluminum reactions. Then the $Al_3Ti/A356$ melts (with or without Sr addition) were poured into a preheated (250 °C) permanent steel mold at 730 °C (± 10 °C) and cooled down to room temperature in air. The permanent steel mold was made for producing dog-bone shape samples for tensile tests. T6 heat treatment was conducted on a portion of as-cast samples with the following procedure: solution treatment 540 °C for 4 h and quenching into room temperature water (25 °C), followed by artificial aging at 155 °C for 6 h. For comparison, as-cast and T6 heat-treated A356 alloy specimens were also prepared with the same casting and T6 treatment procedures as those of the $Al_3Ti/A356$ composites.

The dog-bone shaped ingots were ground and polished to rectangular gage sections with the section area of 6 mm \times 6 mm. The gauge length was 25.4 mm. Uniaxial tensile tests were conducted on an ATS-900 machine at room temperature with a strain rate of $10^{-3} s^{-1}$. A minimum number of three samples were tested for each as-cast or T6 heat-treated materials. The microstructures and fracture surfaces of the specimens were characterized by a Quanta 3D field emission scanning electron microscope (FESEM) equipped with an energy dispersive X-Ray spectrometer (EDS). The samples were ground and polished for backscattered electron image (BSE) analysis. The EDS analysis was conducted with accelerating voltage of 10 kV for both point and mapping analyses with an Aztec software. TruMap mode was selected in EDS mapping to distinguish elements with near identical peaks. Image J software was used for quantitative image analysis to characterize the size and morphology of Si and Al_3Ti particulates.

4.3 Microstructure Analysis

4.3.1 SEM analysis

The typical microstructures of as-cast and T6 treated A356 alloy and $Al_3Ti/A356$ composites without or with Sr addition are shown in Fig. 4.1. From Figs. 4.1(b), (c), (e) and (f), the in-situ Al_3Ti particulates in the composites are generally blocky in shape forming agglomerates partially both inside the Al grains and at the Al grain boundaries. The eutectic Si phase in as-cast A356 is normally coarse in size and needle-shaped, as shown in Fig. 4.1(a). In comparison, in $Al_3Ti/A356$ composites, despite the needle-shaped eutectic Si phase still exists, the morphology is

mainly refined to finer sizes with a smaller average aspect ratio. That is attributed to the existence of Al_3Ti particulates at the Al grain boundaries, acting as obstacles to the growth of eutectic Si phase. With Sr addition, the eutectic Si phase is modified into a short fibrous morphology with circular cross section areas, as presented in Fig. 4.1(c). T6 heat treatment refined the eutectic Si phases both in the A356 alloy and in the composites into round Si particles, as shown in Figs. 4.1(d)~(f). However, the Si particles in the A356 alloy after T6 treatment still show in a coarse size and a large aspect ratio. Comparatively, the Si particles in the composites are finer in size with a better circularity. The reason is that the as-cast composites have finer eutectic Si phase than that in as-cast A356 alloy. Therefore, after identical T6 treatment, the finer eutectic Si phase has a higher tendency to be spheroidized.

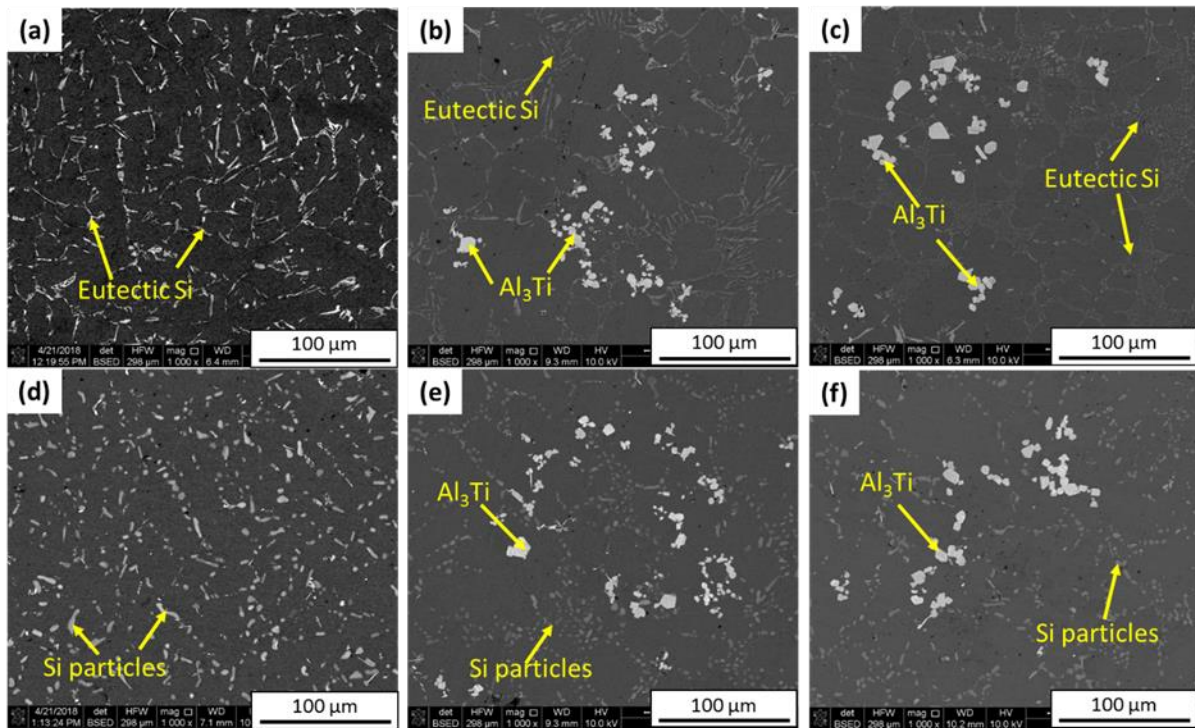


Figure 4.1. Backscattered electron images of as-cast (a) A356 alloy, (b) $\text{Al}_3\text{Ti}/\text{A356}$ and (c) $\text{Al}_3\text{Ti}/\text{A356-Sr}$ composites; and T6 treated (d) A356, (e) $\text{Al}_3\text{Ti}/\text{A356}$ and (f) $\text{Al}_3\text{Ti}/\text{A356-Sr}$ composites.

The results of detailed quantitative image analysis about the sizes and aspect ratios of the Si and Al_3Ti particulates are presented in Fig. 4.2, for which at least 1000 particles were measured for each sample. From the measurement, the diameter of Al_3Ti particulates falls within 2~20 μm

with an average size of 5~6 μm in all composites. The aspect ratio of Al_3Ti particulates ranges from 1~2, close to an equiaxed morphology. The effects of both T6 treatment and Sr addition on the size and the morphology of Al_3Ti particulates are limited. From Figs. 4.2(c) and (d), both the average diameter and aspect ratio of Si particles are reduced in the presence of Al_3Ti particles and are further reduced by Sr addition, especially for the as-cast samples.

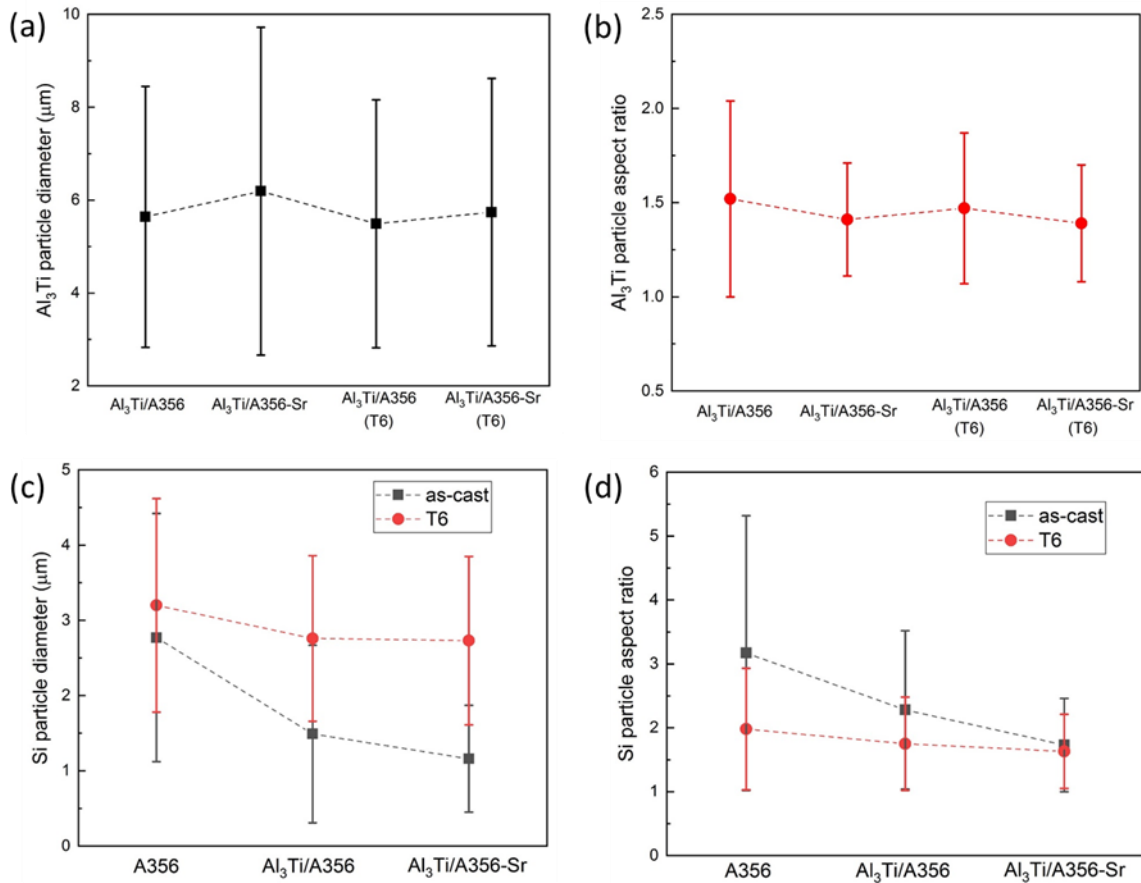


Figure 4.2. Statistics of (a) average particle diameter and (b) average aspect ratio of Al_3Ti particles; (c) average particle diameter and (d) average aspect ratio of Si particles in different samples.

4.3.2 EDS analysis

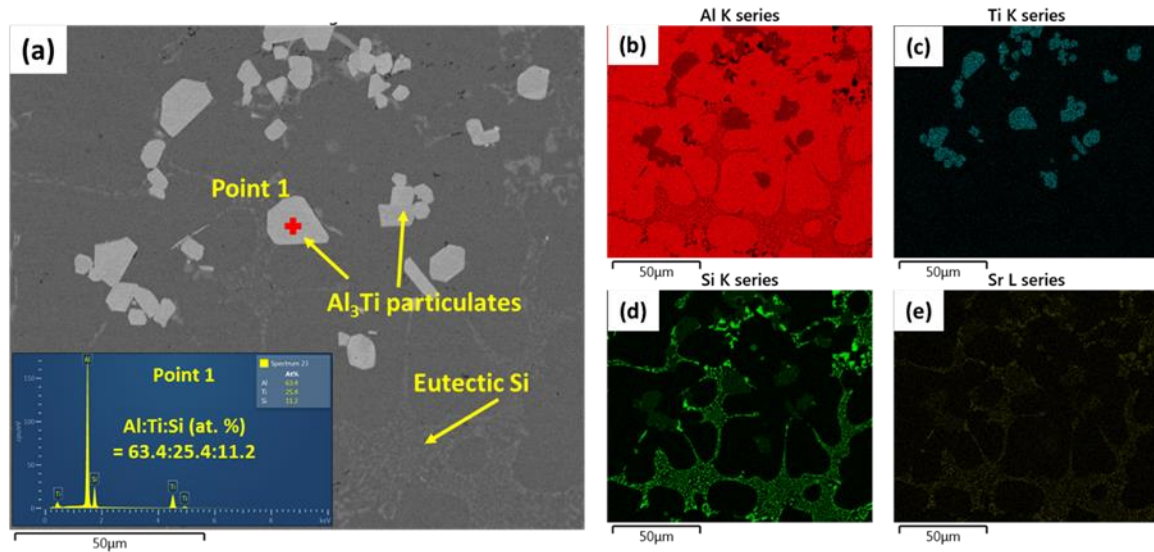


Figure 4.3. EDS analyses of as-cast Al₃Ti/A356-Sr composite (a) Back scattered electron image with an inserted EDS spectrum from point 1 on an Al₃Ti particle; (b)~(e) Elemental mapping of Al, Ti, Si and Sr elements, respectively.

The results of EDS elemental mapping are presented in Figs. 4.3 and 4.4, showing the distributions of elements in as-cast and T6 treated Al₃Ti/A356 composites, respectively. Comparing Figs. 4.3(d) to 4.3(e) and Figs. 4.4(d) to 4.4(e), it is obvious that Sr is mainly associated with Si in both as-cast and T6 treated samples. However, Sr is rarely detected in association with Al₃Ti particulates in all the composite samples.

According to relevant work on in-situ Al₃Ti particulate reinforced Al-Si alloy matrix composites (X. Gao et al., 2015; Z. Liu et al., 2018; Z. Liu, Wang, et al., 2014), Si element is commonly found in Al₃Ti particulates by forming an (Al,Si)₃Ti phase through the substitution of Al, owing to an energy stabilization effect according to first-principle calculations (C. Yang et al., 2018). In this study, the compositions of Al₃Ti particulates in the composites were measured by EDS point analysis. The results revealed that the atomic ratio of Al:Ti:Si was 63.5: 25.4: 11.1 (the standard deviation of each element was < 0.1 at. %) as presented in the spectrum of Point 1 in Fig. 4.3(a) for an as-cast sample. According to first-principle calculations by others, the amount of Si can reach as high as 12.5 at. %, while the amount of Si in (Al,Si)₃Ti is normally in the range of 9~11 at. % from experimental results (C. Yang et al., 2018). The Si content is close to the upper

limit of this range in the present study. In addition, the content of Ti (25.4 at. %) is in coincidence with an $(\text{Al,Si})_3\text{Ti}$ phase, which is therefore assumed the product.

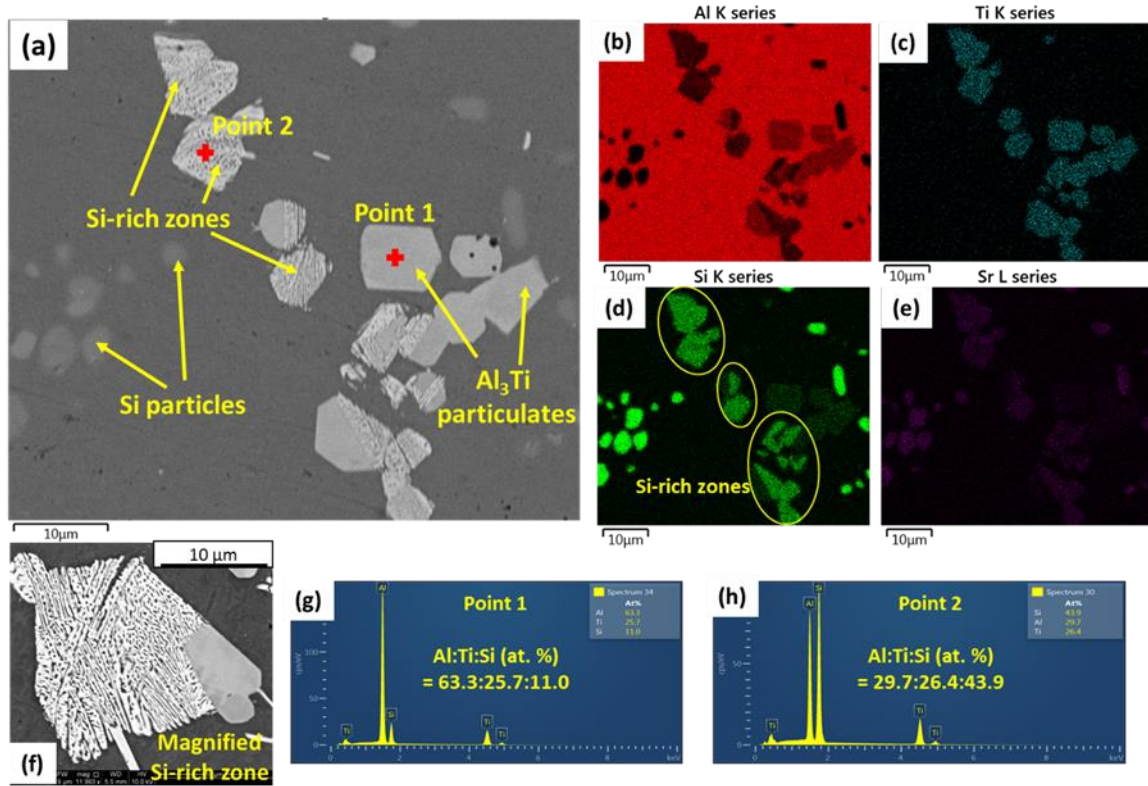


Figure 4.4. EDS analysis of a T6 treated $\text{Al}_3\text{Ti}/\text{A356-Sr}$ sample (a) Back scattered electron image with an inserted image shows the magnified structure of Si-rich zone); (b)-(e) Elemental mapping of Al, Ti, Si and Sr, respectively; (f) a magnified SEM image showing the structure of a Si-rich zone; (g) and (h) spectra of point 1 and point 2 in figure (a), respectively.

For the T6 treated samples, similar EDS point analysis spectra were collected from randomly chosen Al_3Ti particulates, represented by Point 1 in Fig. 4.4(a). These particulates have almost an identical composition to the Al_3Ti particulates in the as-cast samples, suggesting the same $(\text{Al,Si})_3\text{Ti}$ phase after T6 treatment. However, Si-rich zones were detected in the Al_3Ti particulates after T6 treatment, as noted in Figs. 4.4(a) and 4.4(d). The atomic ratio of Al:Ti:Si in such zones was $29.9 \pm 3.7: 26.1 \pm 1.6: 44.0 \pm 2.2$ from EDS point analysis, such as Point 2. From a magnified image of an Al_3Ti particle, as in Fig. 4.4(f), the Si-rich zone has a complex lath-shaped network structure obviously different from the $(\text{Al,Si})_3\text{Ti}$ phase before T6 treatment.

4.4 Mechanical Properties

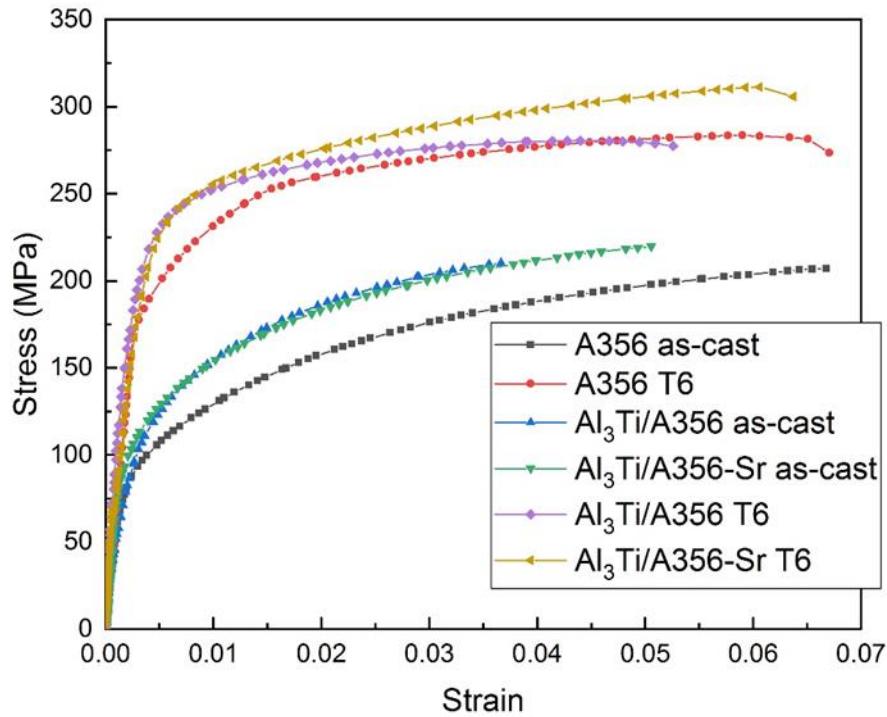


Figure 4.5. Stress-strain curves of A356 and Al₃Ti/A356 composites

The tensile stress-strain curves of the A356 alloy and the in-situ Al₃Ti/A356 composites are shown in Fig. 4.5, while the mechanical properties (yield strength (YS) at 0.2 % residual plastic strain, ultimate tensile strength (UTS) and EL% (Elongation)) are presented in Table 4.1.

In general, the introduction of Al₃Ti particulates improves the YS by 5~10 MPa in the as-cast samples and by 10~20 MPa in the T6 treated samples. The elongation of both as-cast and T6 treated Al₃Ti/A356 composites is evidently lower than that of the A356 alloy. The decreased ductility is due to the agglomeration of hard Al₃Ti particulates, which results in stress concentration and internal cracks at a comparatively small strain. However, with Sr addition, the elongation of the Al₃Ti/A356 composites is improved. The elongation of T6 treated Al₃Ti/A356-Sr composite is even comparable to that of the T6 treated A356 alloy. The increase of elongation is attributed to the refined morphology and size of eutectic Si phase by Sr modification, which eliminate the stress concentration caused by coarse Si phase or particles. Accordingly, the ultimate

tensile strength (UTS) of the composites are increased at the same time. From Table 4.1, the UTS of as-cast and T6 treated Al₃Ti/A356-Sr composites is 6.1 % and 9.8 % higher than that of A356 alloy at corresponding state, respectively.

Table 4.1. Tensile properties of A356 alloy and Al₃Ti/A356 composites

Samples	As-cast			T6		
	A356	Al ₃ Ti/A356	Al ₃ Ti/A356-Sr	A356	Al ₃ Ti/A356	Al ₃ Ti/A356-Sr
YS /MPa	113.0	124.6	118.2	216.3	229.2	237.5
UTS /MPa	207.0	210.2	219.7	283.5	280.5	311.2
El /%	6.6%	3.6%	5.1%	6.7%	5.3%	6.4%

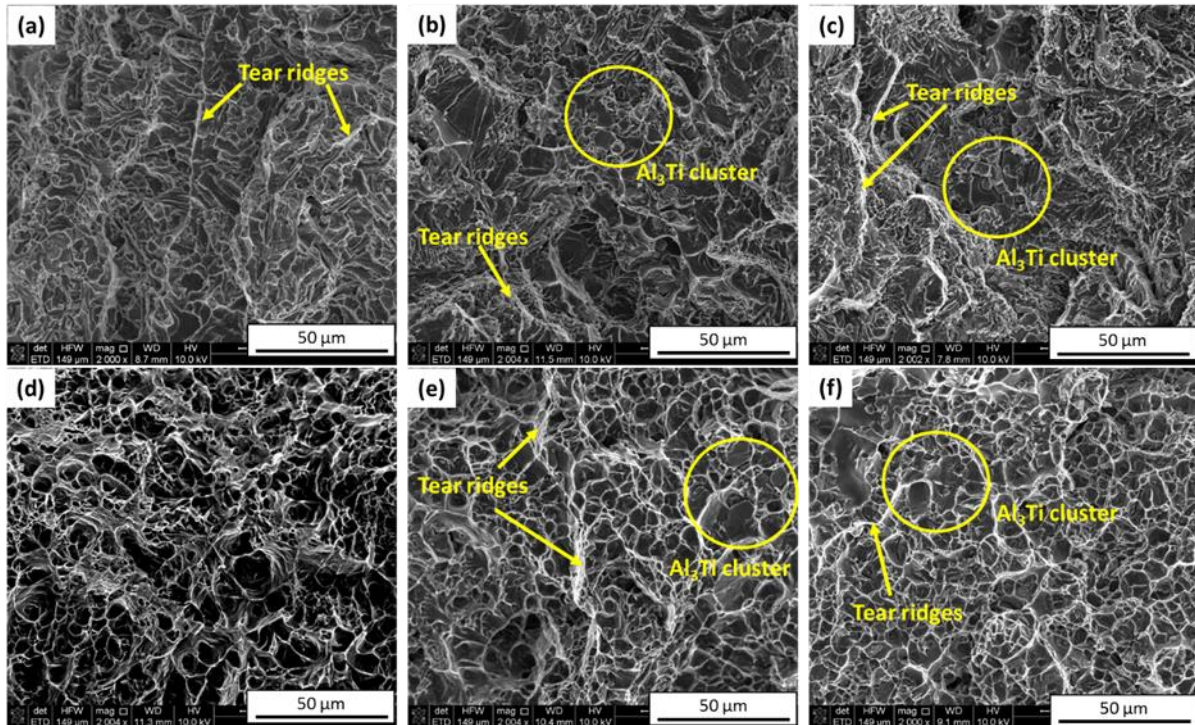


Figure 4.6. Typical fracture surface of as-cast (a) A356 alloy, (b) Al₃Ti/A356 and (c) Al₃Ti/A356-Sr composites; and T6 treated (d) A356, (e) Al₃Ti/A356 and (f) Al₃Ti/A356-Sr composites.

The fracture surfaces of as-cast A356 and composites samples are presented in Figs. 4.6(a)~(c). For A356 alloy, it was common to see a number of elongated dimples, indicating needle shaped Si phase near the surface. In comparison, elongated holes were hardly seen on the fracture

surfaces of the composites. A large number of equiaxed tiny dimples appear on the fracture surface instead, especially for the Sr modified composites, which is attributed to the refined Si particles. Furthermore, the agglomerations of Al₃Ti particulate were observed inside portions of the large holes. For all the three as-cast samples, tear ridges were found on the fracture surface, indicating a quasi-cleavage fracture (C. Yang et al., 2018).

Figs. 4.6(d)~(f) show the typical fractography of T6 treated A356 and composites samples. The dominate feature on the fracture surfaces are equiaxed dimples, in which spheroidized Si were found. Comparatively, the size of the dimples is the largest in A356 and the finest in Al₃Ti/A356-Sr, which is in accordance with the corresponding Si particle sizes in these samples. In addition, large holes appeared in the composites caused by the agglomerations of Al₃Ti particulates. Tear ridges still appeared on the fracture surfaces of Al₃Ti/A356 composites but rarely on that of A356 sample.

4.5 Discussions

4.5.1 Effect of Sr addition

In Al-Si casting alloys, Sr plays an important role in modifying eutectic Al-Si phase. Related research (J. H. Li et al., 2015) has proposed that Sr element is entrapped in the eutectic Si phase, forming an Al₂Si₂Sr phase or Sr-rich clusters. The entrapped Sr promotes the formation of multiple twins in a Si crystal, restricting the growth of Si plates and promoting branching. The EDS results in Figs. 4.3 and 4.4 revealed that Sr is mainly in association with Si phase in both as-cast and T6 treated composites samples, in agreement with other findings on the effects of Sr on Al-Si casting alloys. However, Sr is rarely detected in association with Al₃Ti particulates in both as-cast and T6-state. The result is in agreement with the absence of interaction between Ti and Sr at a Ti level up to 0.5 % as reported by Samuel et al. (2014). Others have also proposed that Ti does not react with Sr regardless of the amount of Ti or holding time (Tahiri et al., 2018). From the microstructure of Sr modified as-cast Al₃Ti/A356 composites in Fig. 4.1(c) and the statistics in Fig. 4.2, coarse eutectic Si phase are modified to smaller size and aspect ratio in the two dimensional images by Sr addition, similar to the modifying effect of casting Al-Si alloys without the introduction of reinforced particulates (Closset & Gruzleski, 1982; Tahiri et al., 2018). Meanwhile, the size and morphology of Al₃Ti particulates are almost unchanged regardless of the

Sr addition. As a result, Sr is entrapped in eutectic Si phase as a modifier but without a direct interaction with Al_3Ti particulates in the $\text{Al}_3\text{Ti}/\text{A356}$ composites.

As to the mechanical properties, the addition of Sr evidently improves the ductility of $\text{Al}_3\text{Ti}/\text{A356}$ composites by modifying the coarse plate-shaped eutectic Si phase to fine globular-fibrous morphology. The average Si particle size and aspect ratio are reduced. As a result, for each modified Si particle, particle cracking becomes difficult compared with the unmodified Si plates (Caceres & Griffiths, 1996; Rao et al., 2018). From the fractography analysis in Fig. 4.6, fine equiaxed dimples are observed more frequently on the fracture surface of $\text{Al}_3\text{Ti}/\text{A356}$ -Sr composite, indicating a better ductility. Summarizing the fracture surface observation as well as the mechanical properties of the samples in Table 4.1, the refinement of Si particles by Sr reduces the probability of the cracking of Si particles and extends the ductility of the $\text{Al}_3\text{Ti}/\text{A356}$ composites.

4.5.2 Effect of Al_3Ti

Comparing the Si morphology of A356 alloy and $\text{Al}_3\text{Ti}/\text{A356}$ composites at both as-cast and T6 states in Fig. 4.1 as well as the statistics in Fig. 4.2(c), the introduction of Al_3Ti reinforcements effectively reduced the size of Si, even without Sr modification. That could be attributed to two reasons. On one hand, Al_3Ti particulates in the interdendritic regions act as obstacles which restricts the growth of Si in composites. From the microstructure of $\text{Al}_3\text{Ti}/\text{A356}$ composites in Fig. 4.1(b), the Al_3Ti particulates at the interdendritic regions could block the growth of the adjacent Si plates. In comparison, coarse needle-shaped Si particles are still commonly observed if no Al_3Ti particulates exist in interdendritic regions. On the other hand, Si element can substitute Al in Al_3Ti particulates by forming an $(\text{Al},\text{Si})_3\text{Ti}$ phase by 9~11 at. % as mentioned in Section 4.3.2. In other words, plenty of solute Si are consumed by participating in the formation of the in-situ Al_3Ti particulates. As a result, the total concentration of Si for forming eutectic Si phase is reduced, which also restricts the growth of eutectic Si.

Moreover, the enrichment of Si in Al_3Ti also decreases the diffusion rate of Ti in liquid Al onto the surface of the Al_3Ti particulates and therefore restricts the growth of the Al_3Ti particulates (Timpel et al., 2012), promoting the formation of small sized in-situ Al_3Ti particulates in A356 alloys. Furthermore, the capability of the Al_3Ti particles in nucleating α -Al grains in solidification is adversely affected by the enrichment of Si in/on the Al_3Ti particulates, resulting in the

segregation of Al₃Ti particulates at the α -Al grain boundaries. The segregation of Al₃Ti particulates in an Al-Si alloy is predictable by thinking of the poisoning of Al-Ti-B type grain refiners by Si in Al (X. Liu et al., 2017).

The blocky and rather small-sized Al₃Ti plays an effective role in improving the yield strength. For the Al₃Ti/A356 alloys, the increases of YS are mainly attributed to the load bearing strengthening, coefficient of thermal expansion (CTE) mismatch strengthening, as demonstrated by other investigations (M. Wang et al., 2014; C. Yang et al., 2018). Other strengthening mechanisms, such as the grain refinement strengthening and Orowan strengthening, do not show evident strengthening effect in this study. The grain refinement strengthening is normally expressed by Hall-Petch relationships as $\Delta\sigma_{gf} = k\Delta(d^{-0.5})$, where k is the Hall-Petch coefficient and d is the average grain size (Pande & Cooper, 2009). In this work, the change of α -Al grain size in A356 is not obvious by Al₃Ti or Sr addition. The statistics show the average grain size ranges from ~40 to ~50 μm for all the as-cast and T6 alloys and composites samples. Since Al alloys have a low Hall-Petch coefficient ($k=68 \text{ MPa}\cdot\mu\text{m}^{-0.5}$) (C. Yang et al., 2018), the grain size change has a limited influence on the yield strength ($< 1.1 \text{ MPa}$) within a 10 μm difference, compared to the strengthening effect of CTE and load bearing strengthening. Moreover, the large ($> 1 \mu\text{m}$) Al₃Ti particulates are unlikely to activate Orowan strengthening mechanism (M. Wang et al., 2014).

The load bearing strengthening ($\Delta\sigma_{\text{Load}}$) refers to the load transfer to the reinforcement through the interface between Al₃Ti reinforcement and the matrix. As a result, the applied load to reach the yielding point is improved. The strengthening effect of $\Delta\sigma_{\text{Load}}$ can be calculated as Eq. 2.6, where σ_m is the YS of matrix material, taken as the YS values of as-cast or T6-state A356 alloy in this research from Table 4.1, V_p is the volume fraction of Al₃Ti particulates.

The CTE mismatch strengthening is caused by the formation of geometrically necessary dislocations accommodating the mismatch in coefficient of thermal expansion between Al₃Ti and matrix during cooling. Its contribution is predicted by Eq. 2.7, where β is a constant of 1.25; G_m is the shear modulus of the matrix; b is the Burgers vector of the dislocations; ρ^{CTE} is the dislocation density induced by the CTE mismatch. ρ^{CTE} can be estimated by Eq. 2.8, where E_m and ν are Young's modulus and Poisson's ratio of alloy matrix, respectively; A is a constant that equals to 12; $\Delta\alpha$ is the CTE difference between the A356 matrix and Al₃Ti; ΔT is the difference between the pouring temperature (or quenching temperature for T6 state) and room temperature; d_p is the average Al₃Ti particulate size; and V_p is the volume fraction of Al₃Ti particulates. The

values of these parameters in the current study are given as: $E_m = 70$ GPa; $\nu = 0.33$ (Ghosh & Moorthy, 1998); $b = 0.286$ nm; $\Delta\alpha = 11 \times 10^{-6}$ K⁻¹ (Z. Liu et al., 2018); $\Delta T = 700$ K (for T6 state $\Delta T = 510$ K); $V_p = 0.05$; d_p equals to the corresponding average Al₃Ti particulate size shown in Fig. 4.2.

By calculating the Eqs. 2.6 and 2.7 with corresponding parameters, the load bearing and CTE strengthening by Al₃Ti is 2.8 MPa and 16.3 MPa for as-cast Al₃Ti/A356 composites. For T6 treated composites, they are 5.4 MPa and 14.1 MPa, respectively. So the total improvement of YS is approximately 20 MPa for both as-cast and T6 state Al₃Ti/A356 composites compared to the A356 alloy. The predicted YS improvement is close to the experimental result for T6 state samples, but overestimated for the as-cast samples. The overestimation of YS improvement for the as-cast samples could be attributed to the overestimation of YS of A356 matrix in the Al₃Ti/356 composites. R. Yang et al. (2015) suggested that the yield strength of A356 alloy will decrease with the decrease of aspect ratio of Si particles. In this research, the aspect ratio of Si particles shows apparently decrease in the composites by the addition of Al₃Ti or/and Sr compared to the A356 alloy. Accordingly, the actual YS of the A356 matrix of the as-cast Al₃Ti/A356 composites should be lower than the YS of A356 alloy shown in Table 4.1.

However, from the fracture surface observation and the mechanical properties of the samples and simulation results, the in-situ Al₃Ti particulates in agglomerations undergo a brittle cracking and generate micro cracks at a smaller strain than the Si particles, which will facilitate the crack propagation and fracture. The ductility is adversely affected therefore. It is suggested that the mechanical properties could be further enhanced by dispersing Al₃Ti particles uniformly in addition to the refinement of the Si phase, which will be studied in the future.

4.5.3 Effect of heat treatment

T6 treatment has almost no influence on the Al₃Ti particular size and morphology from the statistics in Figs. 4.2(a) and (b). This is attributed to the low diffusivity of titanium in aluminum at solid state (3×10^{-19} m² s⁻¹ and 3.2×10^{-17} m² s⁻¹ at 500 °C and 600 °C, respectively) (Abbasi Chianeh et al., 2009). Al₃Ti is expected to be stable and coarsening very slowly in this temperature range (Wu et al., 2000). However, T6 treatment changed the composition and structure of the in-situ Al₃Ti particulates by forming Si-rich zones, as shown in Fig. 4.4(a). From detailed SEM analyses and corresponding EDS analysis, in Figs. 4.3 and 4.4, it is evidence that Si-rich zones

become a common feature in the Al_3Ti particulates of the T6 treated composites while no such Si-rich zones or structures in the Al_3Ti particulates of the as-cast composites. It is evident that the Si-rich zones were formed in the T6 heat treatment of $\text{Al}_3\text{Ti}/\text{A356}$ composites through solid diffusion. It should be noted that there were no Si-rich phase reported in association with Al_3Ti particulates after 2 hours of solid solution treatment at 540 °C by other investigations in $\text{Al}_3\text{Ti}/\text{A356}$ composites (Z. Liu et al., 2018; C. Yang et al., 2018). However, numerous Si-rich zones in the Al_3Ti particulates were produced after 4 hours of solid solution treatment at 540 °C in this work. From the comparison, the appearance of Si-rich zones can be time dependent. In addition, the content of Ti in the Si-rich zone remains as about 26.1 at. %, which shows little change from 25.4 at. % in the as-cast samples. The content of Ti was almost not affected during solid solution treatment, probably, due to its low diffusivity in solid aluminum (Abbasi Chianeh et al., 2009). It is likely that Si diffused into Al_3Ti particulates during solution treatment forming $(\text{Al},\text{Si})_3\text{Ti}$ phase, which then attracted more Si atoms in an extended holding period forming a separate Si-rich phase.

Referencing to published results, three possible types of titanium aluminides can form at the aluminum-rich corner from the ternary Al–Si–Ti system (Perrot, 1990): namely $(\text{Al},\text{Si})_3\text{Ti}$, $\text{Ti}_7\text{Al}_5\text{Si}_{12}$ (τ_1), and $\text{Ti}(\text{Al},\text{Si})_2$ (τ_2). In addition, three types of primary TiAlSi intermetallics were also reported co-exist in Al–Si cast alloys, Al_3Ti type (Si 9~11 wt. %), low Si (Si 7~9 wt. %) and high Si type (Si 35~39 wt. %) (X. Chen & Fortier, 2010). Among these reported phases, $\text{Ti}_7\text{Al}_5\text{Si}_{12}$ (τ_1) has a similar atomic ratio of Al, Si, and Ti (Al:Ti:Si = 20.8 : 29.1 : 50 in at. %) with the Si-rich zone in this study. However, a noticeable discrepancy still exists. Moreover, the formation of high Si type phase in the in-situ Al_3Ti particulates in $\text{Al}_3\text{Ti}/\text{A356}$ composites has yet been studied thoroughly. Therefore, the Si-rich zones could be a new Si-rich phase or a structure inside the Al_3Ti particulates. However, it is still difficult to assure the exact phase or structure of such zones based on EDS analysis. Further analysis by using advanced analytical techniques, such as transmission electron microscopy, is carried out to identify the phases, which will be studied in detail in Chapter 5.

4.6 Summary

This chapter has studied microstructure and mechanical properties of the $\text{Al}_3\text{Ti}/\text{A356}$ composites. The composites with 5 vol. % in-situ Al_3Ti particulates were fabricated via salt-metal reactions. The effects of Sr modification and T6 heat treatment on the microstructure and

mechanical properties of the matrix alloy and the composites were studied. The main conclusions are drawn as follows:

Microstructure analysis has revealed the in-situ Al_3Ti particulates in A356 alloy have an average size of 5~6 μm with a blocky morphology in both as-cast and T6 treated composites. The introduction of Al_3Ti particulates plays a role in restricting the growth of coarse-plate eutectic Si phase in as-cast composites. The addition of Sr in the composites mainly refines the size and the morphology of Si phase.

From EDS analysis, in the as-cast composites, Si element substitutes Al in the in-situ Al_3Ti particulates by 11.1 at. %. The Ti content is 25.4 at. %, which coincides with $(\text{Al},\text{Si})_3\text{Ti}$ as reported by others. After T6 treatment at 540 °C for 4 hrs, in addition to the $(\text{Al},\text{Si})_3\text{Ti}$, Si-rich zones were also observed commonly in the Al_3Ti particulates, in which the Si content increases to about 44.0 at. % while the Ti content remains almost unchanged. In addition, no interaction between Al_3Ti and Sr was observed.

The yield strength of A356 alloy was improved by 5 vol. % in-situ Al_3Ti particulates at both as-cast and T6 treated samples. However, the elongation was decreased due to the agglomeration of particulates. With Sr addition, the elongation and ultimate tensile strength of $\text{Al}_3\text{Ti}/\text{A356}$ composites were both increased because of the refinement of eutectic Si phase, compared to the $\text{Al}_3\text{Ti}/\text{A356}$ composites without Sr addition.

From the fractography observation, it is indicated that Al_3Ti agglomeration play a role in nucleating voids and facilitating the evolution of internal damage, causing the loss of ductility. Moreover, with Sr addition, the dimples are refined in size due to the refined Si particles, which benefits ductility.

CHAPTER 5. EVOLUTION OF INTERMETALLIC PHASES IN AN AL-SI-TI ALLOY DURING SOLUTION TREATMENT

This chapter was reprinted, with journal permission, from Ma, S., Li, N., Zhang, C., & Wang, X. (2020). Evolution of intermetallic phases in an Al–Si–Ti alloy during solution treatment. *Journal of Alloys and Compounds*, 831, 154872. <https://doi.org/10.1016/j.jallcom.2020.154872>

5.1 Introduction

Al-Si casting alloys have been broadly utilized by the automobile industry as cylinder blocks, cylinder heads, valve lifters and pistons, for example, due to their high wear resistance, good corrosion resistance, weldability, fluidity and mechanical properties (Tomida et al., 2003; Q. G. Wang & Davidson, 2001; M. Zhu et al., 2012). Ti is an important alloying element in Al-Si alloys. A minor addition of Ti in the forms of Al-Ti or Al-Ti-B master alloys, can achieve an effective grain refinement for Al casting products (Arnberg et al., 1982; Cibula, 1949; Z. Zhang et al., 2006). As reported, Ti addition over its solubility in α -Al (0.15 wt. %) forms TiAlSi intermetallics (T. Gao et al., 2014; McCartney, 1989; Qiu et al., 2007). These intermetallic particles can also act as reinforcements to strengthen Al-Si alloys attributed to their high modulus and strength for metal matrix composites (Qin et al., 2007). For instance, in-situ Al_3Ti particulates have been introduced into Al-Si alloys by adding Ti powder or through reactions of an Al melt with K_2TiF_6 (Z. Liu et al., 2018; S. Ma & Wang, 2019; C. Yang et al., 2018). The Al_3Ti /Al-Si composites generally show improved mechanical properties compared to the matrix alloys. It was found that Al_3Ti particulates exist actually in the form of $(\text{Al,Si})_3\text{Ti}$ ternary intermetallic, with a portion of Al being substituted by Si in the Al_3Ti lattice.

A series of research works have focused on studying the TiAlSi intermetallics in Al-Si casting alloys. As reported, the intermetallic compounds in Al-Si-Ti system are complicated by possible phases, including AlSi_2Ti , AlSi_3Ti_2 , AlSi_3Ti_6 , $\text{Al}_2\text{Si}_5\text{Ti}_3$, AlSi_7Ti_4 , $\text{Al}_5\text{Si}_{12}\text{Ti}_7$, $(\text{Al,Si})_3\text{Ti}$ (T. Gao et al., 2014; Gu et al., 2004; Riley et al., 2006; Villars et al., 1995; Xiong et al., 2004). heat treatment for heat treatable Al-Si casting alloys is required in general to modify coarse eutectic Si and to achieve enhanced mechanical properties. However, there are still a limited number of investigations on the properties of TiAlSi intermetallics in Al-Si alloys during heat treatment. In Chapter 4, it has revealed Si-rich zones in $(\text{Al,Si})_3\text{Ti}$ particulates in a 5 vol. % Al_3Ti reinforced

A356 composite after a solution treatment of 4 h at 540 °C, as shown in Fig. 4.4. These results showed the phase transformation of the TiAlSi intermetallics during the solution treatment of Al-Si alloys. Nevertheless, detailed investigations have not been carried out. As a result, it is worthwhile to investigate the influence of solution treatment on Al-Si-Ti alloys for further understanding the evolution of TiAlSi intermetallics and the long-debated TiAlSi ternary compounds.

This chapter investigates the evolution of TiAlSi intermetallics in an Al-Si-Ti alloy during solution treatment. Solution treatment of the as-cast alloys is performed for different periods to understand the evolution process. The crystal structures and orientation relationship of the TiAlSi phases are also studied to identify and understand the phase transformation, together with further thermodynamic calculations of the Al-Si-Ti system. Based on experimental results, a mechanism is proposed to illustrate the evolution of TiAlSi intermetallics microscopically. The investigation aims to shed light on the evolution and the structure of TiAlSi intermetallics in Al-Si-Ti alloys during heat treatment of Al-Si-Ti alloys for property improvement.

5.2 Experiment

The Al-Si-Ti alloy was fabricated via K_2TiF_6 salt-Al reactions in an A356 alloy melt. The chemical composition of the A356 matrix alloy is Si 7.44, Fe 0.11, Mg 0.31, Ti 0.005 (in wt. %) and balanced Al. 11.98 g K_2TiF_6 salt is added into a 100 g of A356 melt at 780 °C and mechanically stirred by a graphite rod for 10 min for a complete reaction. The melt was then poured into a preheated (250 °C) permanent steel mold at 730 °C (± 10 °C) and cooled in air down to a room temperature. Subsequently, the as-cast Al-Si-Ti alloy was solution treated at 540 °C for 2 to 72 h and quenched into room temperature water (25 °C). The amount of Al, Si and Ti in the alloy is 90.35, 7.30, 2.35 in wt. % (91.56, 7.10, 1.34 in at. %).

The alloy samples were ground and polished for backscattered electron image (BSE) analysis and energy dispersive X-Ray spectroscopic (EDS) analysis by using a Quanta 3D field emission scanning electron microscope (SEM). The accelerating voltage was chosen as 10 kV. TEM foils were prepared with a scanning electron microscope (SEM) and dual focused ion beam (FIB) (Helios Nanolab DualBeam, FEI). The final cleaning step was performed with a beam current of 50 pA and a voltage of 10 keV to minimize FIB-induced damage. The FEI Titan 80-300TM equipped with a monochromator, an image aberration corrector, and a PHENIX energy

dispersive X-ray spectrometer (EDS), has been used to characterize the phase structure and chemical distribution. The combined error of EDS analysis was limited to $\pm 0.5\%$. Thermodynamic calculations of Al-Si-Ti system were carried out by using Pandat softwareTM with an Al-Si-Ti database. Fast Fourier Transform (FFT) of different areas in the HRTEM images, as well as interplanar crystal spacing measurement were conducted by using DigitalMicrographTM software. Electron diffraction patterns were simulated with CryTBox software for indexing phases, by taking crystal structures and lattice parameters from references (Klinger, 2017).

5.3 Microstructure

5.3.1 SEM analysis

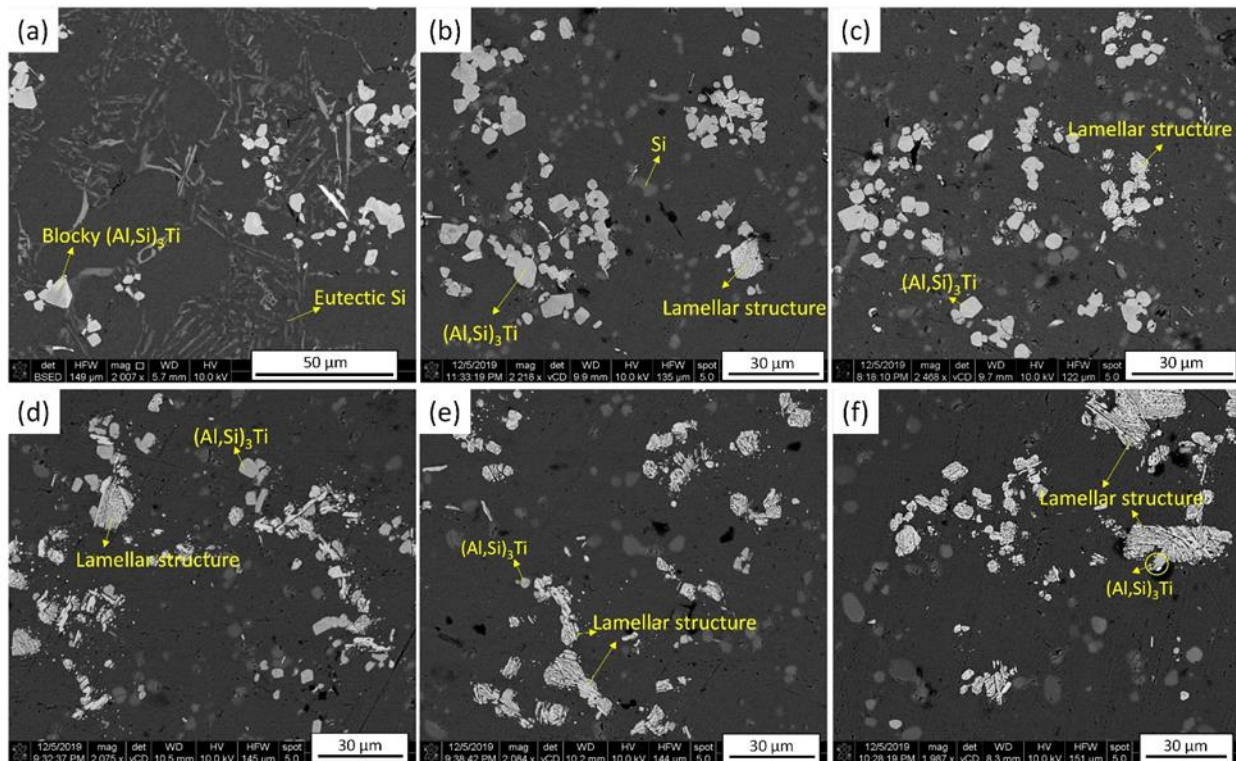


Figure 5.1. Backscattered electron images of the Al-Si-Ti alloy (a) at as-cast state; and after solution treatment at 540 °C for (b) 4 h; (c) 12h; (d) 24 h; (e) 48 h; (f) 72 h.

The typical microstructures of the Al-Si-Ti alloy under different heat treatment conditions are shown in Fig. 5.1. Greyish eutectic Si and bright intermetallic particulates are seen in a dark background of the Al matrix. In Fig. 5.1(a), the eutectic Si is in a coarse needle-like shape in the

as-cast Al-Si-Ti alloy in general. Solution treatment resulted in the fragmentation and spheroidization of coarse eutectic Si needles, as seen in Figs. 5.1(b)~(f). By comparing the general microstructures in these figures, the roundness and size of the Si particulates increased with the solution treatment time.

The intermetallic particulates have a blocky morphology and partially agglomerate either inside the Al grains or at the grain boundaries together with Si particulates in the microstructure. In the as-cast alloy, all the reinforcement appears as plain white particulates, as noted in Fig. 5.1(a). According to related work in Al₃Ti/A356 composites (Z. Liu et al., 2018), these intermetallics were identified as (Al,Si)₃Ti particulates. In contrast, after solution treatment, a lamellar microstructure appears in some of the (Al,Si)₃Ti particulates, as presented in Figs. 5.1(b)~(f). It was found that the lamellar microstructure is appeared randomly on some of the (Al,Si)₃Ti particulates, while the rest (Al,Si)₃Ti particulates have an amorphology as same as in the as-cast alloy, without the appearance of any lamellar structure. The lamellar structure appears either on part of a single (Al,Si)₃Ti particulate with a clear boundary with the untouched portion or a entire (Al,Si)₃Ti particulate after solution treatment. The lamellar structure appears on more (Al,Si)₃Ti particulates with the increase of solution time as shown in Fig. 5.2, based on the random examination of at least 200 reinforcing particulates from each sample. After a 4 h solution treatment, the lamellar structure appears on only about 20 % of the (Al,Si)₃Ti particulates. However, when the solution time exceeds 24 h, the lamellar structure appears on approximately 80 % of the particulates. Therefore, the increase of solution treatment time promotes the formation of the lamellar structure in the Al-Si-Ti alloy. However, no matter how long is the heat treatment time, there remains a big portion of the (Al,Si)₃Ti particulates with their as-cast morphology without the lamellar structure, as shown in Fig. 5.2.

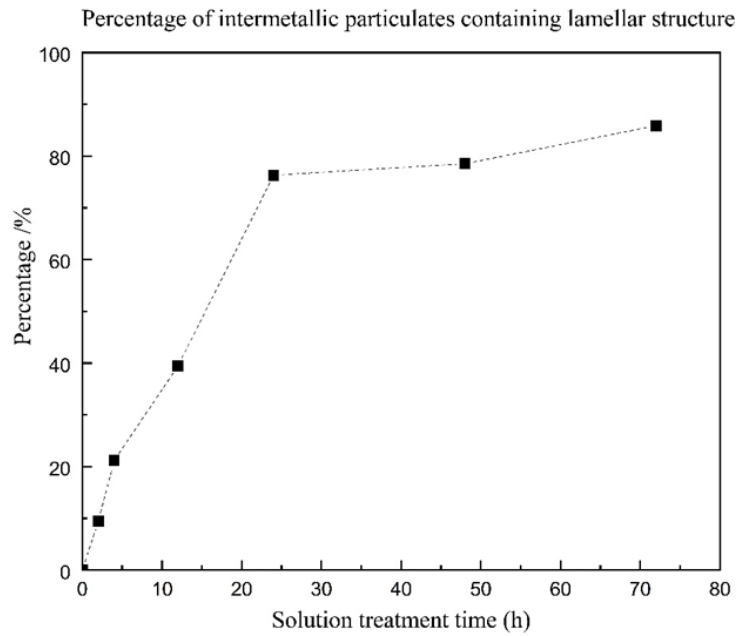


Figure 5.2. Percentage of intermetallic particulates containing lamellar structure in the Al-Si-Ti alloy after different solution treatment time.

5.3.2 EDS analysis

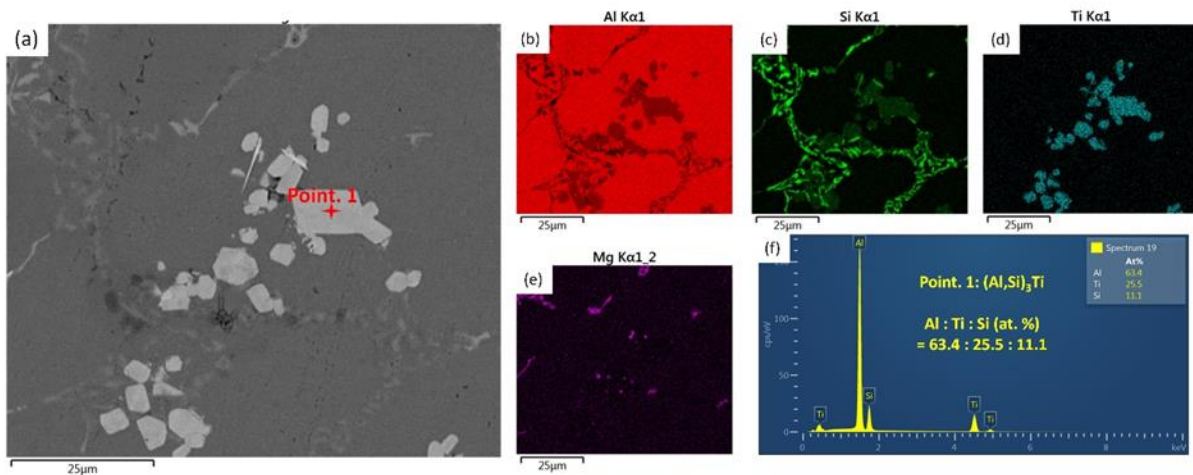


Figure 5.3. (a) Back-scattered electron image of the as-cast Al-Si-Ti alloy with (b)~(e) EDS Elemental mapping of Al, Si, Ti and Mg elements, respectively and (f) an EDS spectrum from Point 1 on an intermetallic particulate in figure (a).

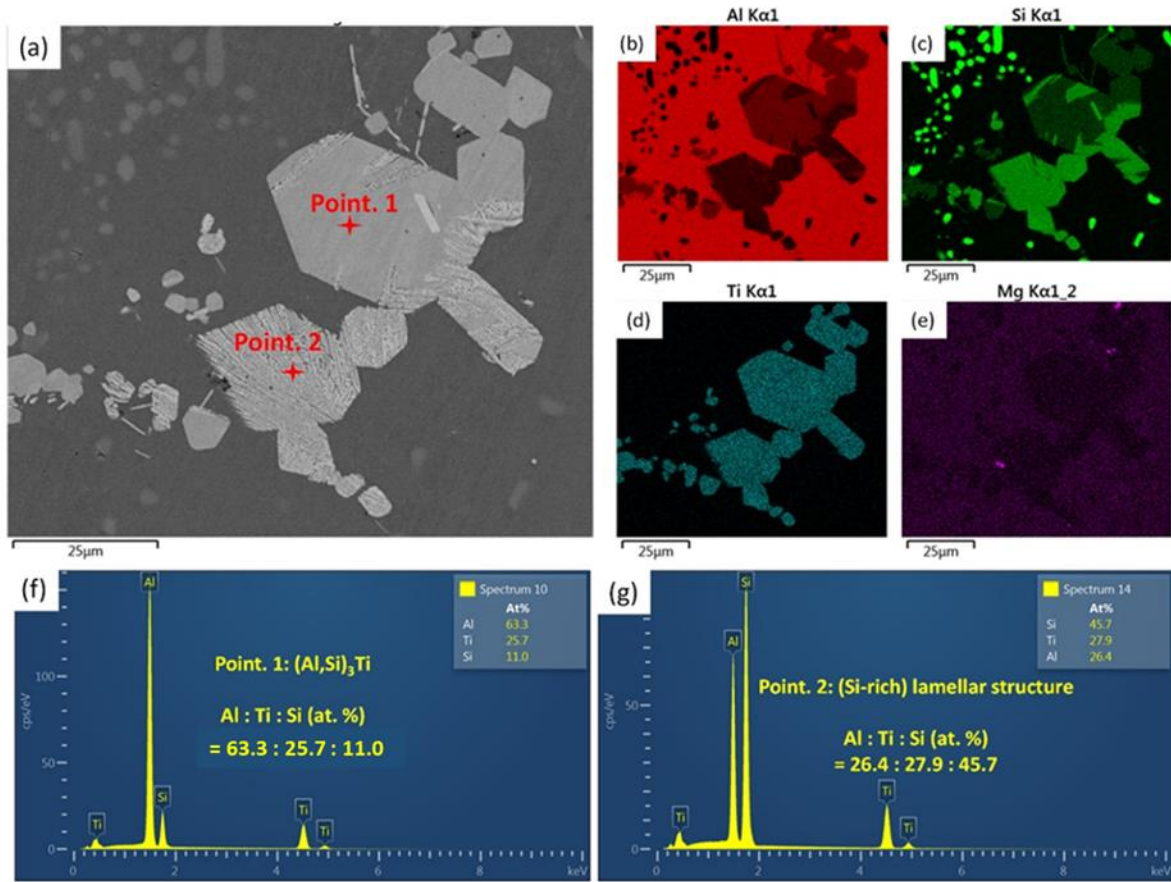


Figure 5.4. (a) Back-scattered electron image of the Al-Si-Ti alloy after 4 h solution treatment, with (b)~(e) EDS Elemental mapping of Al, Si, Ti and Mg elements, respectively, and (f)~(g) the EDS spectra from Point 1 on an intermetallic particulate and Point 2 on the lamellar structure in figure (a), respectively.

The EDS results of the as-cast Al-Si-Ti alloy are presented in Fig. 5.3. The presence of Si in the intermetallic particulates is confirmed by both Si element mapping in Fig. 5.3(c) and an EDS spectrum from Point 1 in one of the intermetallic particulates. The particulates were suggested as an $(\text{Al,Si})_3\text{Ti}$ phase, in which Si substitutes Al in the Al_3Ti lattice in the as-cast $\text{Al}_3\text{Ti}/\text{A356}$ composites. According to first-principle calculations, the substitution is favored by lowering the energy of the system. The amount of Si in $(\text{Al,Si})_3\text{Ti}$ can reach as high as 15 at. %, but normally in the range of 9~11 at. % according to experimental results (Mohanty & Gruzleski, 1996; C. Yang et al., 2018). The results of this study revealed an atomic ratio of Al:Ti:Si in the intermetallic particulates being 63.4 : 25.5 : 11.1, evidencing an $(\text{Al,Si})_3\text{Ti}$ phase in the as-cast alloy.

The EDS results of the Al-Si-Ti alloy after 4 h solution treatment are shown in Fig. 5.4. From Fig. 5.4 (a), the lamellar structure appeared either on parts of a single intermetallic particulate

or throughout of a particulate completely. The elemental mapping of Si and Ti in Figs. 5.4 (c) and (d) revealed a rather uniform distribution of Ti element in all the intermetallic particulates. But Si is enriched in the lamellar structure only, for which the lamellar structure was called a Si-rich phase in Chapter 4. EDS analyses were performed on a series of points, noted as Point 1, on the intermetallic particulates without a lamellar structure and Point 2 on the lamellar structure in Fig. 5.4(a). The Al:Ti:Si atomic ratio at Point 1 is almost identical to the results from Fig. 5.3(f), suggesting an $(\text{Al,Si})_3\text{Ti}$ phase. Meanwhile, the Al:Ti:Si ratio of the lamellar regions is 26.4: 27.9: 45.7, evidencing the enrichment of Si in the lamellar structure from 11.1 at. % for $(\text{Al,Si})_3\text{Ti}$ to 45.7 % mainly at the expense of Al, while the amount of Ti in the lamellar structure is slightly increased comparing with the $(\text{Al,Si})_3\text{Ti}$ phase.

Additional EDS point analyses have been carried out on both $(\text{Al,Si})_3\text{Ti}$ phase and the Si-rich lamellar structure of numerous intermetallic particulates in samples after different solution treatment times. The statistics are shown in Table 5.1, where the composition of the $(\text{Al,Si})_3\text{Ti}$ phase remains almost unchanged, regardless of the solution treatment time. For the lamellar structure, with the increase of solution treatment time, the content of Al decreased while those of Ti and Si increased slightly.

Table 5.1. EDS point analysis on the locations of $(\text{Al,Si})_3\text{Ti}$ and the lamellar structure in the samples after different solution treatment times

Solution treatment time/h	$(\text{Al,Si})_3\text{Ti}$			Lamellar structure		
	Al /at. %	Ti /at. %	Si /at. %	Al /at. %	Ti /at. %	Si /at. %
0	63.3 ± 0.2	25.4 ± 0.2	11.3 ± 0.3	--	--	--
2	63.8 ± 0.3	25.4 ± 0.2	10.8 ± 0.3	26.7 ± 4.6	27.3 ± 1.8	46.0 ± 2.9
4	63.2 ± 0.3	25.7 ± 0.4	11.1 ± 0.1	28.5 ± 1.3	26.5 ± 0.9	45.0 ± 0.5
12	62.9 ± 0.1	25.9 ± 0.1	11.2 ± 0.2	26.7 ± 1.2	27.5 ± 1.0	45.8 ± 0.5
24	63.3 ± 0.4	25.3 ± 0.3	11.4 ± 0.1	24.1 ± 4.1	28.8 ± 1.8	47.1 ± 2.2
48	63.1 ± 0.9	25.0 ± 0.4	11.9 ± 1.3	22.0 ± 4.0	29.7 ± 1.7	48.3 ± 2.2
72	63.3 ± 0.7	25.5 ± 0.7	11.2 ± 0.4	22.7 ± 3.1	29.3 ± 1.5	48.0 ± 1.5

5.3.3 TEM analysis

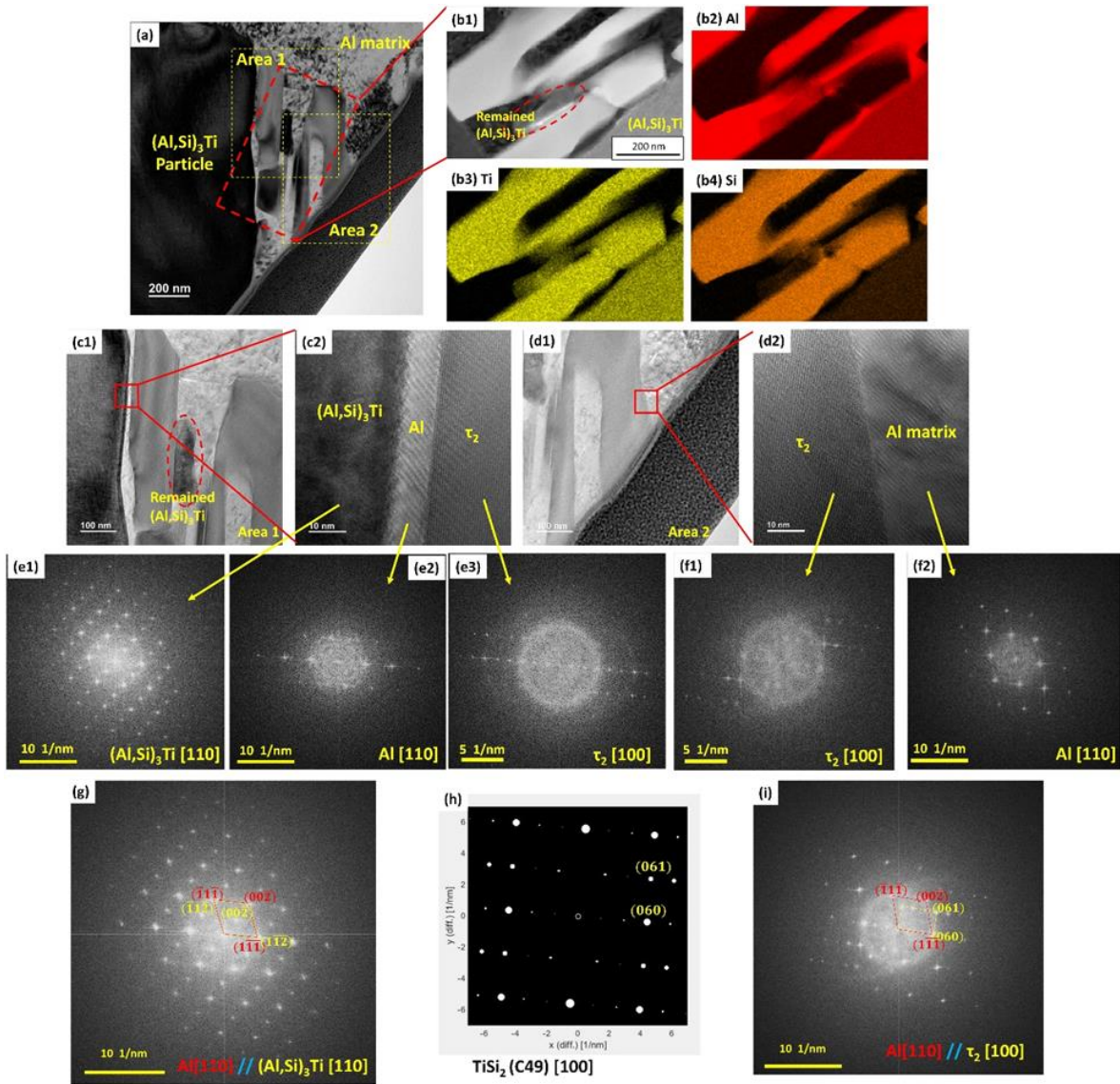


Figure 5.5. (a) A TEM bright field image of the composite after solution treatment for 4 h showing an interface between an $(\text{Al,Si})_3\text{Ti}$ particulate and the lamellar structure; (b1) scanning transmission electron microscopy (STEM) high-angle annular dark-field (HAADF) of the red rectangular area in figure (a) and (b2~b4) corresponding EDS elemental mappings of Al, Ti, and Si. (c1) magnified TEM image of Area 1 in figure (a); (c2) magnified HRTEM image of the red rectangular area in figure (c1); (d1) magnified TEM figure of Area 2 in figure (a); (d2) magnified HRTEM image of the red rectangular area in figure (d1); (e1)~(e3) corresponding FFT patterns of different locations in figure (c2); (f1, f2) corresponding FFT patterns of different locations in figure (d2); (g) the FFT pattern from the $(\text{Al,Si})_3\text{Ti}$ -Al interface; (h) simulated diffraction pattern of TiSi_2 (C49-type) from [100] axis; (i) the FFT pattern from the τ_2 -Al interface.

To understand the lamellar structure, TEM was conducted on a FIB sample of the interface between an $(\text{Al,Si})_3\text{Ti}$ particulate and the lamellar structure from a sample after 4 h solution treatment. The results are shown in Fig. 5.5(a). From the STEM HAADF image in Fig. 5.5(b1), the lamellar structure started to form from a corner of the big $(\text{Al,Si})_3\text{Ti}$ particulate consisting of a series of bright and black stripes in the thickness of 100 nm ~ 200 nm. The EDS elemental mappings of the region, as shown in Figs. 5.5(b2~b4), provide a detailed elemental distribution and a local compositional inhomogeneity. The bright stripes in Fig. 5.5(b1) contain mainly Ti and Si elements without Al. In contrast, the black zones contain Al without the detection of noticeable Ti and Si elements. In addition, an $(\text{Al,Si})_3\text{Ti}$ particulate with a light-greyish contrast is located in the bottom-right corner of Fig. 5.5(b1), where Al, Ti and Si elements were all detected. Comparing the strength of color of the EDS elemental mappings in Figs. 5.5(b2~b4), the amount of Al in the black zones is more than in the $(\text{Al,Si})_3\text{Ti}$, which is more than in the bright stripes. Meanwhile, the amount of Ti in the bright stripes is more than in $(\text{Al,Si})_3\text{Ti}$, which is more than in the black zones. The amount of Si in the bright stripes is more than in the $(\text{Al,Si})_3\text{Ti}$, which is more than in the black zones. Therefore, the elemental distribution suggests that the bright stripes (the lamellar phase) contain mainly Ti and Si, and much less Al than $(\text{Al,Si})_3\text{Ti}$. The black zones contain almost only Al, i.e., being an Al phase.

Moreover, a light-greyish piece is also seen between the bright stripes as noted in Fig. 5.5(b1). From the element mappings in Fig. 5.5(b2~b4), the signals of Al, Si, and Ti of the piece is similar to that of the light-greyish $(\text{Al,Si})_3\text{Ti}$ particulate at the bottom-right corner of Fig. 5.5(b1). Therefore, this small piece is suggested as remaining $(\text{Al,Si})_3\text{Ti}$ phase in the lamellar structure, evidencing the conversion of $(\text{Al,Si})_3\text{Ti}$ particulate to the Si-rich lamellar phase as solution treatment proceeds.

Fig. 5.5(c1) and (d1) are magnified TEM bright field images of Fig. 5.5(a). High resolution TEM (HRTEM) images were taken across the interfaces between the $(\text{Al,Si})_3\text{Ti}$ particulate and the lamellar phase as shown in Fig. 5.5(c2), as well as across the interface of the lamellar phase and Al matrix as in Fig. 5.5(d2). Fig. 5.5(e1) is the FFT patterns from the left hand side of Fig. 5.5(c2), an $(\text{Al,Si})_3\text{Ti}$ particulate. The pattern is indexed to a tetragonal D_{022} Al_3Ti structure (tetragonal I4/mmm) from its $[110]$ zone axis. The interplanar crystal spacings that are interpreted from the FFT pattern are close to theoretical crystal constants of D_{022} Al_3Ti as shown in Table 5.2. It has been reported that $(\text{Al,Si})_3\text{Ti}$ has the same crystal structure (tetragonal I4/mmm) as Al_3Ti (G. Zhu

et al., 2011), in which the substitution of Al by Si results in small changes in its crystal lattices. As a result, $(\text{Al,Si})_3\text{Ti}$ phase is verified.

Figs. 5.5(e2) and (f2) are the FFT patterns of corresponding locations in Figs. 5.5(c2) and (d2), showing an fcc-(Al) structure from its [110] zone axis. The interplanar spacings from the FFT patterns also agree well with the theoretical values of fcc-(Al), as shown in Table 5.2. Therefore, the black zones in Fig. 5.5(b1) are fcc-(Al) phase.

The FFT patterns in Figs. 5.5(e3) and (f1) were produced from the bright stripes in Fig. 5.5(b1), where is enrich of Ti and Si and being depletion of Al. As reported, three TiAlSi ternary compounds may present in Al-Ti-Si alloys, namely $(\text{Al,Si})_3\text{Ti}$, τ_1 and τ_2 (Perrot, 1990). τ_1 and τ_2 are Si-rich phases, which may contain over 40 % Si. The crystal structure of τ_1 is tetragonal ($I4_1/amd$, $a = 0.3576$ nm, $c = 2.715$ nm) (Raman, 1965). The τ_2 is typically expressed as $\text{Ti}(\text{Al}_x\text{Si}_{1-x})_2$ (ZrSi₂-type, orthorhombic; space group $Cmcm$) (Brukl et al., 1961). τ_2 phase is basically TiSi₂, in which the replacement of silicon by aluminum results in small changes in its lattice parameters (Mondolfo, 1976). At a solution treatment temperature of 540 °C, TiSi₂ C49-type is the preferred structure (Mann & Clevenger, 1994) and it also has a ZrSi₂-type crystal structure. Therefore, the τ_2 phase can be considered TiSi₂ (C49) with a portion of Si being replaced by Al. In the current work, the diffraction patterns of τ_1 were simulated based on its reported structure and lattice parameters (Raman, 1965). However, the composition and lattice parameters of τ_2 are not sure. The diffraction patterns of τ_2 were, therefore, simulated with reference to TiSi₂ (C49) phase, taking its crystal structure and lattice parameters from references (Qiu et al., 2007).

Apart from τ_1 and τ_2 , other reported Al-Si-Ti intermetallic phases were also simulated based on references (Brukl et al., 1961; Raman, 1965; Schubert et al., 1963, 1964), including $\text{Al}_2\text{Si}_3\text{Ti}_2$ (space group: $Cmcm$, $a = 0.3618$ nm, $b = 1.352$ nm, $c = 0.3618$ nm), AlSi_3Ti_6 ($P6/mcm$, $a = 0.743$ nm, $c = 0.514$ nm), AlSi_7Ti_4 ($Cmcm$, $a = 0.3635$ nm, $b = 1.419$ nm, $c = 0.3613$ nm), $\text{Al}_2\text{Si}_5\text{Ti}_3$ ($Cmcm$, $a = 0.360$ nm, $b = 1.353$ nm, $c = 0.360$ nm). After a thorough comparison of the simulated diffraction patterns of these phases, it is found that the FFT patterns in Figs. 5.5(e3) and (f1) are close to the diffraction patterns of TiSi₂ (C49) phase from its [100] zone axis, as shown in Fig. 5.5(h). The interplanar crystal spacings from the FFT patterns also closely match the simulation results of TiSi₂ (C49) phase in Table 5.2. However, the differences in intensities between the FFT patterns and simulation patterns of TiSi₂ (C49) in Fig. 5.5(e3) and (f1) should be noted. The patterns do not match TiSi₂ (C49) crystal exactly, but more likely being the $\text{Ti}(\text{Al}_x\text{Si}_{1-x})_2$.

τ_2 phase in which a certain amount of Si is replaced by Al in the TiSi_2 (C49) crystal. Therefore, based on the FFT patterns and also the EDS mapping results, the bright stripes are the τ_2 phase. However, since Al and Si can replace each other over a wide range of composition in τ_2 phase, resulting in a large range of chemical compositions, the exact composition and cell structure of the τ_2 phase that was observed in this study cannot be certified.

The near-rational orientation relationships (OR) of the Al, $(\text{Al,Si})_3\text{Ti}$ and τ_2 phases are elucidated from the FFT patterns from the HRTEM images of the interfaces. An OR is suggested as $(\text{Al,Si})_3\text{Ti}$ [110] // Al [110] and $(\text{Al,Si})_3\text{Ti}$ ($\bar{1}\bar{1}\bar{2}$) // Al ($\bar{1}\bar{1}\bar{1}$) in Fig. 5.5(g). The OR is in agreement with reported OR between Al_3Ti and Al (X. Gao et al., 2015; Guo et al., 2016). The patterns in Fig. 5.5(i) from an Al- τ_2 interface suggests a near-rational OR of Al [110] // τ_2 [100] and Al ($1\bar{1}\bar{1}$) // τ_2 (060). However, a direct contact between $(\text{Al,Si})_3\text{Ti}$ and τ_2 phase was hardly observed in the TEM images. A layer of Al locating between $(\text{Al,Si})_3\text{Ti}$ and τ_2 is seen clearly in Fig. 5.5(g). It is suggested that an $(\text{Al,Si})_3\text{Ti}$ - τ_2 interface is not prevailed as the Al- $(\text{Al,Si})_3\text{Ti}$ and $(\text{Al,Si})_3\text{Ti}$ - τ_2 interfaces are more common in the current work.

Table 5.2. The crystallographic data of the related phases with a comparison of the measured interplanar crystal spacings from FFT patterns in Fig. 5.5

Phase	Structure	Space group	Lattice parameters /nm	Interplanar crystal spacing d_{hkl} /nm		Refs.
				From FFT	Simulation	
fcc(Al)	Cubic	Fm3m	a=0.405	$d(\bar{2}\bar{2}0) = 0.1445$ $d(\bar{1}\bar{1}\bar{1}) = 0.2357$ $d(002) = 0.2036$	$d(\bar{2}\bar{2}0) = 0.1433$ $d(\bar{1}\bar{1}\bar{1}) = 0.2341$ $d(002) = 0.2027$	Massalski (1990)
Al_3Ti (D0 ₂₂)	Tetragonal	I4/mmm	a=b=3.854; c=8.584	$d(\bar{1}\bar{1}2) = 0.2301$ $d(\bar{2}\bar{2}0) = 0.1369$ $d(00\bar{4}) = 0.2133$	$d(\bar{1}\bar{1}2) = 0.2300$ $d(\bar{2}\bar{2}0) = 0.1362$ $d(00\bar{4}) = 0.2146$	Norby et al. (1986)
TiSi_2 (C49)	Orthorhombic	Cmcm	a=0.361; b=1.377; c=0.365;	$d(060) = 0.2249$ $d(061) = 0.1948$	$d(060) = 0.2295$ $d(061) = 0.1943$	Qiu et al. (2007)

5.4 Thermodynamic calculations of the Al–Si–Ti system

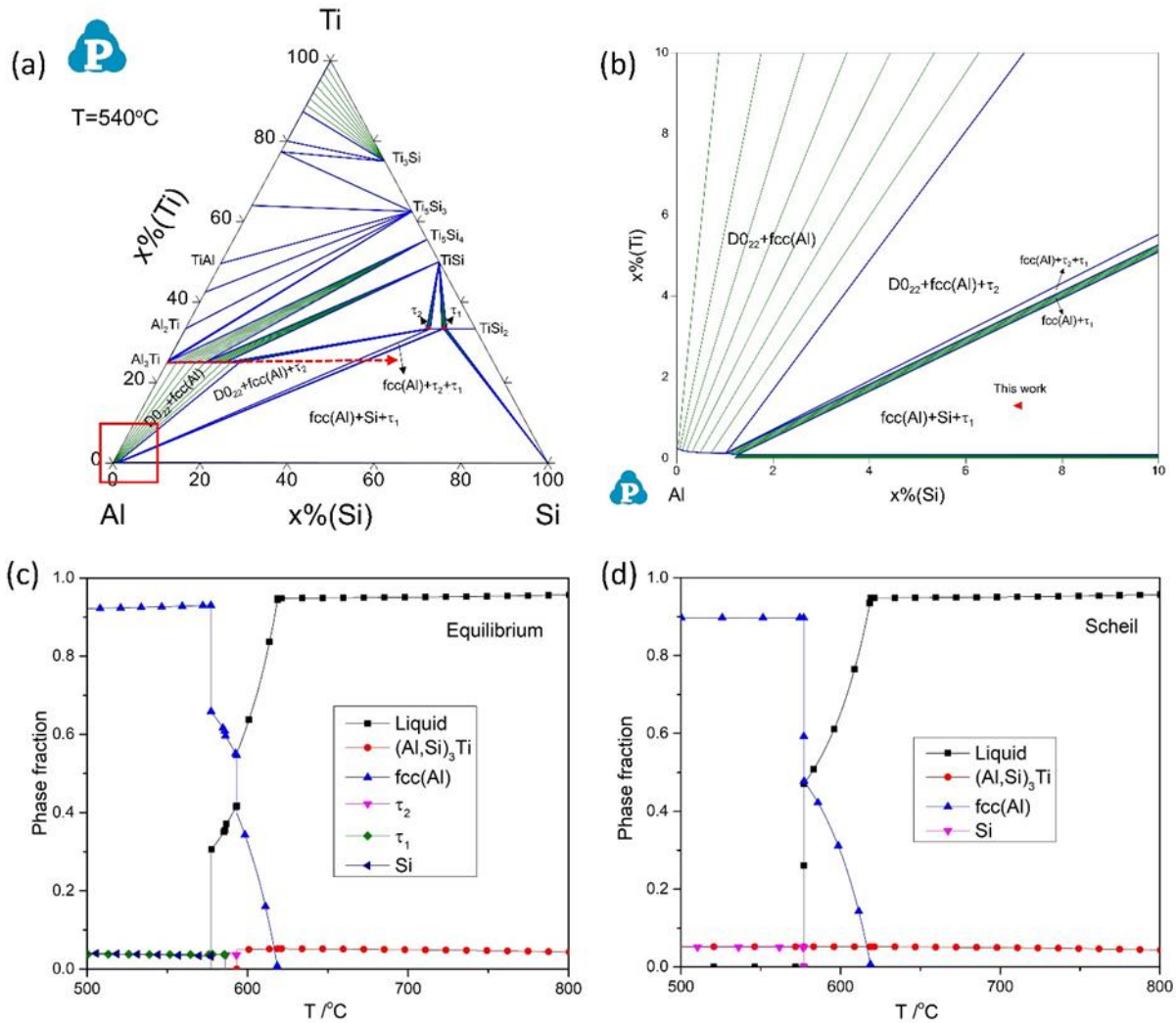


Figure 5.6. (a) A calculated isothermal section of Al-Si-Ti ternary system at 540°C ; (b) Magnified red rectangular area in the Al-rich corner in figure (a); (c) and (d) The evolution of phase fractions in the Al-7.10 at. % Si-1.34 at. % Ti alloy simulated under equilibrium condition and Scheil condition, respectively.

To help understand the formation of the Si-rich lamellar structure, thermodynamic calculations of Al-Si-Ti system were carried out with the Al-Si-Ti database of Pandat Software (Yang Li et al., 2016). Fig. 5.6(a) presents an isothermal section of the Al-Si-Ti ternary phase diagram at 540°C . The τ_2 and τ_1 phase at this temperature has a composition of $\text{Al}_{11.2-10.4}\text{Si}_{55.5-56.3}\text{Ti}_{33.3}$ and $\text{Al}_{7.7-6.7}\text{Si}_{59.0-60.0}\text{Ti}_{33.3}$, respectively. The calculated compositions lie within the range

reported by Yang Li et al. (2016). Fig. 5.6(b) shows a magnified zone at the Al-rich corner of Fig. 5.6(a). It is seen that the composition of the studied Al-Si-Ti alloy locates in the Si + fcc(Al) + τ_1 three-phase equilibrium region. Besides, to understand the phase evolution with the Al-Si-Ti database, solidification simulations were performed from 800 °C to 500 °C on the Al-7.10 at. % Si-1.34 at. % Ti alloy, which is identical to the studied alloy. Both equilibrium and Scheil conditions were simulated as shown in Fig. 5.6(c) and Fig. 5.6(d), respectively. Under equilibrium condition in Fig. 5.6(c), τ_2 phase appears via the reaction of $L + (Al,Si)_3Ti \rightarrow \alpha-Al + \tau_2$ when temperature decreases to 593 °C. Subsequently, τ_2 transforms to τ_1 via the reaction of $L + \tau_2 \rightarrow \tau_1 + \alpha-Al$ at 586 °C. Both reactions are in well consistent with other research (Dezellus et al., 2014; S. Liu et al., 2008). The alloy completely solidifies at 577 °C. Only Si, fcc(Al) and τ_1 coexist between 500 °C and 577 °C under equilibrium condition, which agrees with the Si + fcc(Al) + τ_1 three-phase equilibrium at 540 °C in Fig. 5.6(b) for the studied Al-Si-Ti alloy. However, it is suggested that Scheil solidification prevails during a permanent mold casting rather than equilibrium condition due to the fast solidification rate, the reaction $L + (Al,Si)_3Ti \rightarrow \alpha-Al + \tau_2$ is suppressed therefore (Yang Li et al., 2020; Luo et al., 2014). For the studied Al-Si-Ti alloy simulated under Scheil condition in Fig. 5.6(d), it is seen that the amount of $(Al,Si)_3Ti$ remains almost unchanged throughout the simulated temperature range. Meanwhile, neither τ_2 nor τ_1 phase appears. Si, fcc(Al) and $(Al,Si)_3Ti$ coexist after complete solidification.

In the current study, Al_3Ti (D0₂₂) particulates are formed near the K_2TiF_6 -Al interface after Ti is reduced by Al from the K_2TiF_6 salt, which is given in Reaction 5.1 below (X. Wang et al., 2004; C. Yang et al., 2018). After the completion of the reaction in about 10 min, Si in the melt starts to substitute Al in the Al_3Ti (D0₂₂) lattice, forming a more stable ternary aluminide $(Al_{1-x}Si_x)_3Ti$ through liquid–solid diffusion as in Reaction 5.2 during both reaction and holding (Zhao et al., 2004; G. Zhu et al., 2017). Nevertheless, the presence of τ_2 phase or other Si-rich ternary phases were seldom reported.



According to Reaction 5.1, Ti is enriched in the Al-Si-Ti melt locally at the K_2TiF_6 -Al interface during the chemical reaction, while the amount Si near the interface in the Al-Si-Ti melt

is limited. Therefore, the formation of Al_3Ti containing limited amount of Si if not at all prevails. The formation of $(\text{Al},\text{Si})_3\text{Ti}$ is realized through diffusion of Si in the melt. As a result, a high concentration of Si in ternary Al-Ti-Si phases is unlikely to form during the chemical reaction and a short holding period in the A356 melt. During the permanent steel mold casting, Scheil solidification is indicated. The formation of Si-rich ternary Al-Ti-Si phases such as τ_2 and τ_1 are suppressed. $(\text{Al},\text{Si})_3\text{Ti}$ phase remains during the solidification process. Some of the $(\text{Al},\text{Si})_3\text{Ti}$ particulates act as nuclei for the formation of Al grains, while other locations in the melt away from the $(\text{Al},\text{Si})_3\text{Ti}$ follow a typical Al-Si eutectic reaction path in solidification. Therefore, $\text{Si} + \text{fcc}(\text{Al}) + \text{D0}_{22}(\text{Al},\text{Si})_3\text{Ti}$ phases are formed as observed in the as-cast sample in the current work, complying with the simulation result under Scheil condition in Fig. 5.6(d).

As same as in general casting alloys, the as-cast Al-Si-Ti alloy has a microstructure of $(\text{Si} + \text{fcc}(\text{Al}) + \text{D0}_{22}(\text{Al},\text{Si})_3\text{Ti})$, which is metastable based on the isothermal diagram of the alloy at 540 °C in Fig. 5.6(b). During a heat treatment at 540 °C, the diffusion of Ti is limited in Al, while the diffusion of Si into $(\text{Al},\text{Si})_3\text{Ti}$ substituting Al is dominated (Abbasi Chianeh et al., 2009; Christian, 1975). Therefore, the amount of Ti in $(\text{Al},\text{Si})_3\text{Ti}$ particulates remains almost a constant, a solid phase transition of the as-cast $\text{D0}_{22}(\text{Al},\text{Si})_3\text{Ti}$ particulates is predicted with the increase of Si content as noted by the red-dashed arrow in Fig. 5.6(a). $\text{D0}_{22}(\text{Al},\text{Si})_3\text{Ti}$ transforms into $\text{D0}_{22}(\text{Al},\text{Si})_3\text{Ti} + \text{fcc}(\text{Al}) + \tau_2$ first. Then $\text{D0}_{22}(\text{Al},\text{Si})_3\text{Ti}$ disappears totally and τ_1 forms subsequently, coexisting with $\text{fcc}(\text{Al}) + \tau_2$. Finally, τ_2 disappears and Si phase forms, reaching $\text{Si} + \text{fcc}(\text{Al}) + \tau_1$ three-phase equilibrium. The evolution of $(\text{Al},\text{Si})_3\text{Ti}$ to τ_2 phase from the thermodynamic calculation is supported by the observation of a τ_2 phase in the current study during solution treatment for 4 h and the content of τ_2 keeps increasing with the increase of solution treatment time up to 72 h. Because of the existence of $(\text{Al},\text{Si})_3\text{Ti}$ as observed in Fig. 5.1(f), it is indicated that $\text{D0}_{22}(\text{Al},\text{Si})_3\text{Ti}$ phase still partly transforms into τ_2 , locating at the $\text{D0}_{22}(\text{Al},\text{Si})_3\text{Ti} + \text{fcc}(\text{Al}) + \tau_2$ region of Fig. 5.6(a) after 72 h solution treatment. A similar solid phase transition was reported in the investigation of phase equilibria in the Al-rich corner of Al-Si-Ti system (Luo et al., 2014). In their work, τ_2 did not appear under an as-cast condition in an Al-9.2 Si-14.3 Ti (at. %) sample although three-phase equilibrium $((\text{Al},\text{Si})_3\text{Ti} + \text{fcc}(\text{Al}) + \tau_2)$ is expected with the composition. After a long annealing period (3168 h) between 450~550 °C, a portion of $(\text{Al},\text{Si})_3\text{Ti}$ phase transformed into Si-rich ternary τ_2 phase as observed in the current work.

Theoretically, for the studied alloy after up to 72 h solution treatment, τ_1 phase can hardly form since there is no region showing the coexistence of τ_1 and $D0_{22}$ $(Al,Si)_3Ti$ based on the calculation from Fig. 5.6(a). However, $Si + fcc(Al) + \tau_1$ three-phase equilibrium will be finally reached if a long enough heat treatment time is given. So it is inferred that τ_2 is still a metastable phase in the studied alloy and will transform to τ_1 with prolonged solution treatment time. The $\tau_2 \rightarrow \tau_1$ solid phase transition was supported by related works (Yang Li et al., 2016; Luo et al., 2014) in an Al-28.0 Si-3.9 Ti (at. %) alloy between 500~550 °C after a long annealing period (3168 h).

5.5 Al-Si-Ti phase evolution

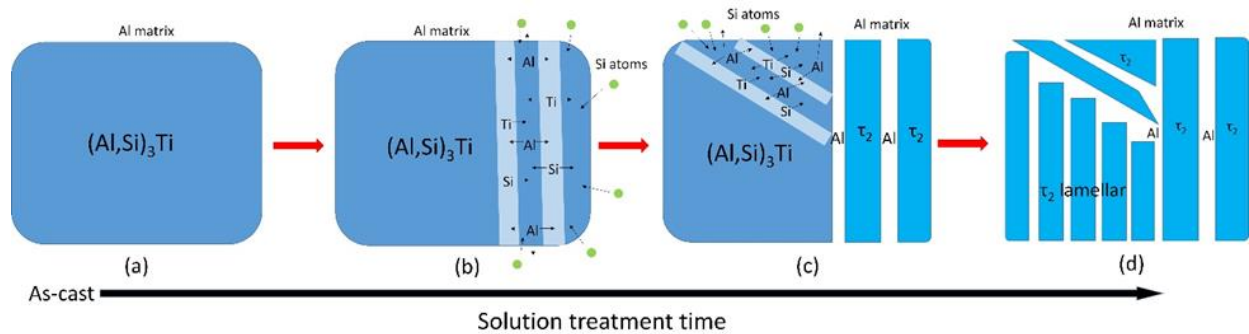
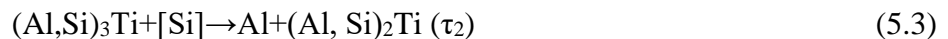


Figure 5.7. Schematic drawing of the transition from a solid $(Al,Si)_3Ti$ particulate to a lamellar structure with the increase of solid solution treatment time; (a) blocky $(Al,Si)_3Ti$ in as-cast alloy; (b) Si enrichment in a part of the particulate and the diffusion of elements along the arrows; (c) formation of lamellar structure limited to only parts of the particulates together with further Si enrichment and elemental diffusion in another area; (d) a completion of the transition of the entire $(Al,Si)_3Ti$ particulate into a lamellar structure.

A formation mechanism of the lamellar structure is elucidated as following based on previous analyses. Only blocky $(Al,Si)_3Ti$ particulates form in the as-cast Al-Si-Ti alloy because of the nature of the K_2TiF_6 -Al melt reaction, which produces excess of Ti at the melt/salt interface. In the follow on solution treatment, $(Al,Si)_3Ti$ transforms into the Si-rich τ_2 phase as suggested by the thermodynamic calculations in Section 5.4. Comparing the composition of $(Al,Si)_3Ti$ ($Si \leq 0.15$, $Ti \approx 0.25$) with τ_2 ($Al_{17.8-9.2}Si_{48.9-57.5}Ti_{33.3}$), the enrichment of Si and Ti is essential for the $(Al,Si)_3Ti \rightarrow \tau_2$ transition. The transition is therefore realized via the diffusion of Si and Ti, resulting in the formation of a lamellar structure or phase in the blocky $(Al,Si)_3Ti$ particulates. The diffusion of Si and Ti in α -Al is calculated at the solution treatment temperature (540 °C) as shown in Table 5.3.

To help in understanding the phase transition with the increase of solid solution treatment time, a schematic drawing is presented in Fig. 5.7. As shown in the figure, after a short solution treatment period ($t=2$ h and 4 h for example), the estimated diffusion distance of Si is as much as $52.3 \sim 74.0 \mu\text{m}$, which is comparable to the grain size in Fig. 5.1. As a result, Si atoms from eutectic Si particulates can readily diffuse into the $(\text{Al},\text{Si})_3\text{Ti}$ particulates through the Al matrix. However, a short solution treatment time is not enough to reach a homogeneity for Si to diffuse into the $(\text{Al},\text{Si})_3\text{Ti}$ particulates. Therefore, Si only enriches in a limited number of $(\text{Al},\text{Si})_3\text{Ti}$ particulates, or in parts of certain $(\text{Al},\text{Si})_3\text{Ti}$ particulates. In the Si enrichment areas, $(\text{Al},\text{Si})_3\text{Ti}$ transform to τ_2 phase as the Si content exceeds its solubility in $(\text{Al},\text{Si})_3\text{Ti}$, while for other areas, the $(\text{Al},\text{Si})_3\text{Ti}$ remain unchanged as shown in Fig. 5.7(b). Additionally, the diffusion of Ti is also required for the phase transition as mentioned above. From Table 5.3, Ti has a much smaller diffusion coefficient than Si does. The calculated diffusion distance for Ti is merely $0.12 \sim 0.18 \mu\text{m}$ after 2 h~4 h of solution treatment. As a consequence, Ti can only diffuse within a single $(\text{Al}, \text{Si})_3\text{Ti}$ particulate. According to the current work, the lamellar structure starts to form after 2~4 h solution treatment time with a lamellar thickness of $100 \sim 200 \text{ nm}$, which is close to the calculated diffusion distance. As a result, it is suggested that Ti atoms diffuse inside the $(\text{Al}, \text{Si})_3\text{Ti}$ particulates within a limited distance (approximately the τ_2 lamellar thickness), forming the τ_2 lamellar in the Si enrichment areas in the particulates. Meanwhile, as Ti and Si are diffused out of the original $(\text{Al}, \text{Si})_3\text{Ti}$ phase to form the nearby τ_2 lamellar, Al is left among the τ_2 lamellae, which is accordance with the TEM results in Fig. 5.6, i.e., fcc-(Al) phase locates among the τ_2 lamellae. Thereby, the formation of a lamellar structure in the $(\text{Al}, \text{Si})_3\text{Ti}$ particulates can be explained reasonably. The increased Si content in τ_2 phase is therefore attributed to both the diffusion of Si from the Al matrix and within the $(\text{Al}, \text{Si})_3\text{Ti}$ particulate, meanwhile the increase of Ti is attributed to the diffusion of Ti within the $(\text{Al}, \text{Si})_3\text{Ti}$ particulate, as shown in Figs. 5.7(b) and (c). The phase transition can be summarized as Reaction 5.3.



With the increase of solution treatment time, the diffusion of Si and Ti in the $(\text{Al},\text{Si})_3\text{Ti}$ particulate continues, meanwhile, more Si atoms in the matrix diffuse into the particulate. As a result, the formation of τ_2 lamellae proceeds continuously until the entire $(\text{Al},\text{Si})_3\text{Ti}$ particulate is

converted into τ_2 lamellae, leaving Al in place, as illustrated in Fig. 5.7(d). Therefore, the amount of τ_2 phase in the microstructure is increased accordingly, in agreement with the microstructures in Fig. 5.1 and statistics in Fig. 5.2. From the observation of the lamellar structure in Fig. 5.1 after a different solution treatment period. The lamellar thickness does not show obvious difference. On one hand, the diffusion rate of Ti is very slow, its maximum diffusion distance is still very limited (0.75 μm) after even 72 h of solution treatment. On the other hand, once the τ_2 lamellae forms, Ti in τ_2 can hardly diffuse back into the nearby Al phase. Consequently, the coarsening of the τ_2 lamellae does not occur. It should be noted that τ_2 can transform to τ_1 to reach equilibrium state with long enough heat treatment time for the studied alloy, which requires further investigation.

Table 5.3. Diffusion data for the dilute solution of Ti and Si in α -Al matrix at solution treatment temperature 540 °C (813 K), where R is the gas constant (8.31 J/mol·K) (Christian, 1975).

Element	Pre-	Activation	Diffusion Coefficient	Diffusion distance at 813 K			
	exponential	Energy	at 813 K	$x=(Dt)^{1/2}$ (μm)			
	Factor	Q	$D=D_0\exp[(-Q/RT)]$	t=2 h	t=4 h	t=24 h	t=72 h
	D_0 (m^2/s)	(kJ/mol)	(m^2/s)				
Ti	0.112	260	2.17×10^{-18}	0.12	0.18	0.31	0.75
Si	1.38×10^{-5}	117.6	3.80×10^{-13}	52.3	74.0	181.3	314.0

The formation of τ_2 phase in the Al-Si-Ti alloy after solution treatment can be also influential in the micromechanical properties. $(\text{Al,Si})_3\text{Ti}$ shows increased elastic modulus (280 GPa vs 220 GPa) and nanohardness (10.7 GPa vs 9.2 GPa) than pure Al_3Ti does (Pang et al., 2013). Another research showed that by increasing Si content, microhardness of TiAlSi increases synchronously. The microhardness of TiAlSi phase increased by about 4 times (from 59.06 HV to 305.1 HV) in an $\text{Al}_x\text{Si}_{1-x}\text{Ti}$ alloys under an as-cast condition as the content of Si was varied from 3 % to 60 % (T. Gao et al., 2011). The Si-rich TiAlSi phase in that work has an obviously increased hardness compared to the low-Si $(\text{Al,Si})_3\text{Ti}$ phase.

Recent work has reported introducing in-situ Al_3Ti particulates in heat treatable Al-Si casting alloys (such as A356) to fabricate aluminum matrix composites with increased mechanical properties (Z. Liu et al., 2018; S. Ma & Wang, 2019). From the mechanical property point of view, the phase transformation from $(\text{Al,Si})_3\text{Ti}$ to τ_2 during solution treatment can modify the

morphology of reinforcements from large blocky shape to a refined lamellar structure. The hardness of the TiAlSi intermetallic particulates will be increased with the increase of Si content. However, as Si diffused into the intermetallic particulates to promote phase transformation, Si content in the Al-Si matrix is decreased adversely, affecting the strength of matrix. In addition, a long solution treatment time may also result in the coarsening of eutectic Si particulates. So it is still difficult to evaluate the effects of the evolution of the TiAlSi intermetallic phase on the mechanical properties of Al₃Ti/Al-Si matrix composites. Further investigation is required.

5.6 Summary

In this chapter, an Al-Si-Ti alloy was produced via K₂TiF₆-Al reactions in an A356 alloy. The evolution of TiAlSi intermetallic phases during solution treatment was investigated. A series of as-cast samples were solution treated at 540 °C for different time periods (0~72 h). Microstructural analysis revealed the evolution history of the TiAlSi intermetallics. The following conclusions are drawn from the study.

The TiAlSi intermetallic particulates are blocky (Al,Si)₃Ti in the as-cast Al-Si-Ti alloy. After solution treatment for 2 h, a lamellar structure starts to form on certain parts of (Al,Si)₃Ti particulates. With the increase of the solution treatment time, the amount of the lamellar structure increases. The lamellar structure forms on approximately 80 % of the (Al,Si)₃Ti particulates after 72 h solution treatment. The lamellae are Si enriched, containing about 45 %~48 % at. % Si compared to the (Al,Si)₃Ti particulates that contain ~ 11 at. % Si. The contents of Al, Ti and Si in both (Al,Si)₃Ti phase and the Si enriched lamellar structure are almost unaffected by the solution treatment time.

A detailed EDS analysis from a STEM HAADF image shows that the lamellar structure consists of Si and Ti enriched stripes (lamellae) with a thickness of 100~200 nm and Al among the stripes. HRTEM observations and corresponding FFT patterns suggest the Si and Ti enriched stripes being an (Al,Si)₂Ti (τ_2) phase with a TiSi₂ (C49) structure, in which Al substitutes Si readily. Between the τ_2 lamellae, Al phase is verified. The Al- τ_2 and (Al,Si)₃Ti- τ_2 interfaces are commonly found while direct contact between (Al,Si)₃Ti and τ_2 can hardly be seen from HRTEM observation. The near-rational orientation relationships (OR) are suggested as (Al,Si)₃Ti [110] // Al [110], (Al,Si)₃Ti ($\bar{1}1\bar{2}$) // Al ($\bar{1}1\bar{1}$) between (Al,Si)₃Ti and Al; and Al [110] // τ_2 [100], Al ($1\bar{1}\bar{1}$) // τ_2 [060] between Al and τ_2 based on the FFT patterns from the interfaces.

Thermodynamic calculations of the Al–Si–Ti system also support the transition from a DO_{22} $(Al,Si)_3Ti$ to a τ_2 phase. τ_1 phase is indicated to be absent in the microstructure after up to 72 h solution treatment. Nevertheless, $\tau_2 \rightarrow \tau_1$ phase transformation is suggested to reach a $Si + fcc(Al) + \tau_1$ three-phase equilibrium for the studied alloy with long enough treatment time.

A formation mechanism of the lamellar structure (eutectoid phase) is proposed with the consideration of the diffusion of Ti and Si during solution treatment. The formation of the Si-rich lamellar τ_2 phase is attributed to the diffusion of Ti and Si within the original $(Al,Si)_3Ti$ reinforcing particulates as well as the diffusion of Si in the Al matrix during solution treatment. The diffusion distance of Ti is quite limited and close to the lamellar thickness. In addition, Al phase forms between the τ_2 lamellae as Si and Ti diffuse into the τ_2 phase. The phase transition during solution treatment is summarized as $(Al,Si)_3Ti + [Si] \rightarrow Al + (Al, Si)_2Ti (\tau_2)$. As the increase of solution treatment time, the diffusion of Si and Ti goes on, resulting in the continuous formation of τ_2 phase until the entire $(Al,Si)_3Ti$ particulate is consumed.

CHAPTER 6. THREE-DIMENSIONAL (3D) MICROMECHANICAL SIMULATION OF THE EFFECT OF PARTICLE SIZE, FRACTION AND DISTRIBUTION ON THE MECHANICAL BEHAVIOR OF AN IN-SITU $Al_3Ti/A356$ COMPOSITE

This chapter was reprinted, with journal permission, from Ma, S., Zhuang, X., & Wang, X. (2019). 3D micromechanical simulation of the mechanical behavior of an in-situ $Al_3Ti/A356$ composite. *Composites Part B: Engineering*, 176, 107115. <https://doi.org/10.1016/j.compositesb.2019.107115>

6.1 Introduction

Recently, numerical methodologies have been applied for micromechanical simulations to study mechanical behavior of multiphase materials based on microstructure-based models. For instance, Finite Element (FE) micromechanical simulations on the microstructure-based Representative Volume Element (RVE) models have been widely adopted to study the mechanical behavior of multiphase materials, such as dual-phase steels (DPs) and metal matrix composites (Qing, 2013a; Ramazani, Pinard, et al., 2013; Sun et al., 2009). A RVE is defined as a volume large enough to be statistically representative of microstructural heterogeneities in the multiphase materials, while small enough to be considered as a volume element of continuum mechanics (Kanit et al., 2003). Numerical simulation on microstructure-based RVE is advantageous in studying the influence of reinforcement (size, morphology, volume fraction, distribution etc.) on the macroscale response of composites to an applied loading. In addition, microscale stress–strain fields and damage evolution can be accessed during a loading process (Qing, 2013a). Two-dimensional (2D) and three-dimensional (3D) RVEs can be adopted for the FE simulation. 2D simulation (with plane stress or plane strain elements) is more attractive than 3D for less time requirement for calculation. However, it cannot be fully representative of the 3D structure and stress-strain states. Therefore, the mechanical properties of composites are not precisely predicted. In comparison, simulations with 3D RVE show a higher accuracy according to related works (Ramazani, Mukherjee, Quade, et al., 2013; Saraev & Schmauder, 2003).

Experimental work has proven the benefits of Al_3Ti particles as reinforcement for aluminum alloys in enhancing the strength (R. Gupta et al., 2018; C. Yang et al., 2018). However, information on numerical simulation on the mechanical properties of Al_3Ti/Al composites is still

scarcely available. FE simulation with RVE is a promising method in investigating the effects of the Al₃Ti particle properties, such as particle size, volume fraction and particle clustering, on the macroscale properties of composites. Moreover, it is important to predict the mechanical properties through tailoring the microstructure for targeted applications.

In this chapter, FE micromechanical simulations with 3D RVEs are conducted with the consideration of the brittle cracking of Al₃Ti particles and the ductile damage of A356 matrix. A series of RVEs are automatically generated with various microstructural features, such as particle size, fraction and distributions, in order to investigate their effects on the flow behavior and damage evolution of Al₃Ti/A356 composites under a uniaxial tensile loading. Furthermore, the Young's modulus, yield strength and elongation of the composites with various microstructural features are predicted from simulation and compared to theoretical calculations or reported experimental results on the Al₃Ti/A356 composites.

6.2 Material and Experiment

A 5 vol. % in-situ Al₃Ti particle reinforced A356 composite was fabricated via the chemical reactions of K₂TiF₆ and an Al melt. The chemical composition of the A356 alloy matrix was Si 7.44, Fe 0.11, Mg 0.31, Ti 0.005 in wt. % and balanced Al. The reaction temperature was set as 780 °C. The melt was stirred mechanically by a graphite rod for 10 min for a complete reaction. After removing the salt products on top, the Al₃Ti/A356 melt was poured into a preheated (250 °C) permanent steel mold at 730 °C (± 10 °C) and cooled down to room temperature in air. The permanent steel mold was made for producing dog-bone shape samples for tensile tests. Subsequently, T6 heat treatment was conducted on samples in the following procedure: solution treatment 540 °C for 4 h and quenching into room temperature water (25 °C), followed by artificial aging at 155 °C for 6 h. The dog-bone shaped ingots were ground and polished with a rectangular gage sections of 6 mm \times 6 mm. The gauge length was 25.4 mm. Uniaxial tensile tests were conducted at room temperature on an ATS 900 machine with a strain rate of 10^{-3} s⁻¹. A minimum number of three samples were tested. The microstructures of the T6 treated Al₃Ti/A356 composites were characterized by using a Leica DM-LM/P optical microscope (OM) and a Quanta 3D Field Emission Scanning Electron Microscope (FESEM). For comparison, A356 alloy samples were also prepared with identical casting and T6 treatment procedures as those of the Al₃Ti/A356 composite. The typical microstructures of the T6 state A356 matrix and Al₃Ti/A356 composite are

shown in Figs. 6.1(a) and (b). Microstructure analysis was conducted on the backscattered electron images of the composites. The results show that the average area fraction is 5.1 %, statistically close to the designed volume fraction of Al₃Ti. The average dendritic cell size of the matrix and the composites are $34.2 \pm 1.4 \mu\text{m}$ and $36.7 \pm 0.6 \mu\text{m}$, respectively. The in-situ Al₃Ti particles are generally randomly located and partially agglomerated in the matrix. Fig. 6.1(c) shows four typical microstructures near fracture surface of the composites after tensile test. The brittle cracking of on Al₃Ti particles is clearly to be seen near the fracture surface. However, interfacial debonding rarely occurs between the Al₃Ti particles and the matrix. The Al₃Ti particle size follows a lognormal distribution approximately with an average size of $5.2 \pm 2.7 \mu\text{m}$, as presented in Fig. 6.1(d).

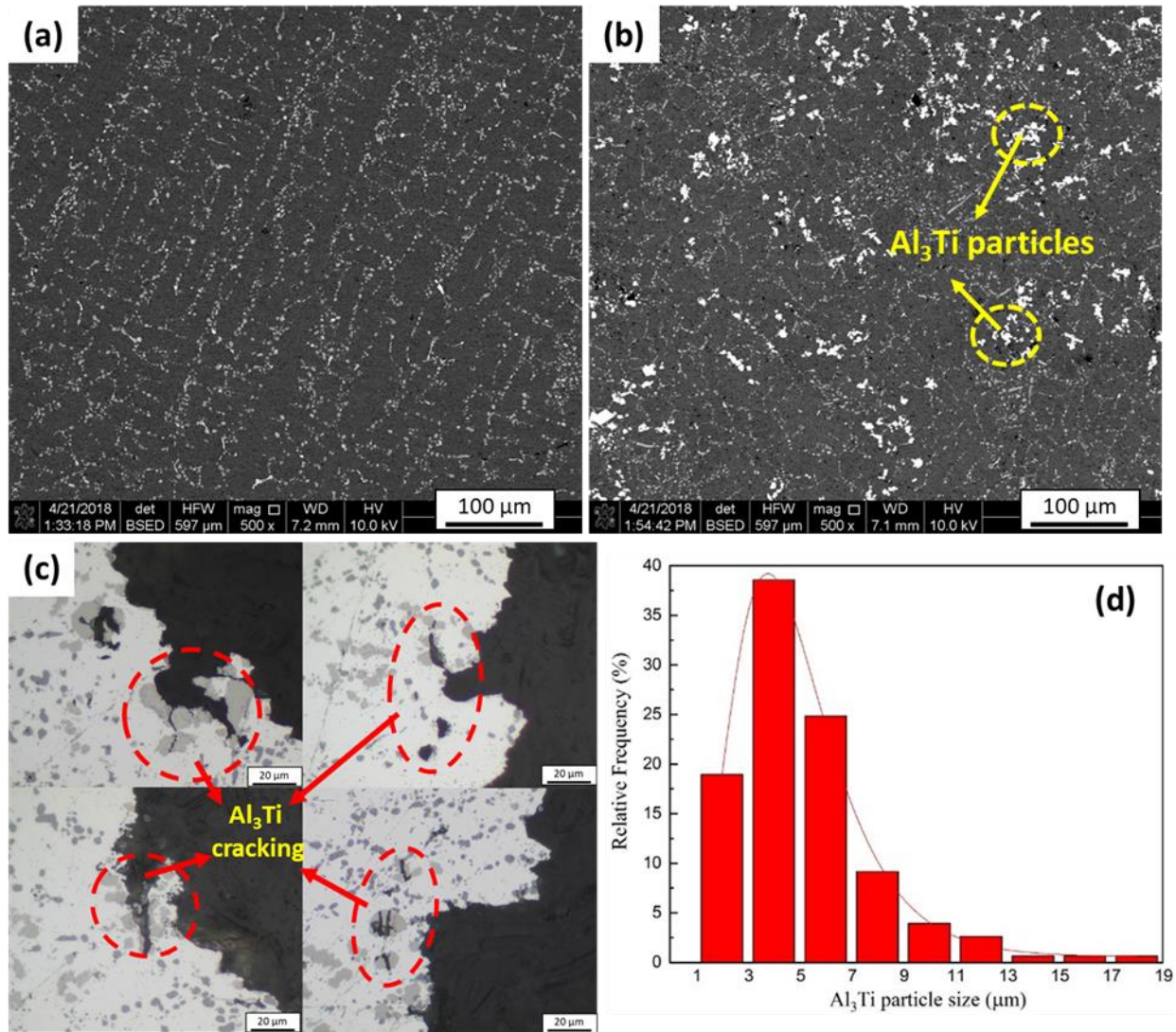


Figure 6.1. Backscattered electron images showing typical microstructure of (a) T6-A356 matrix and (b) T6-Al₃Ti/A356 composite in this work; (c) Optical images showing four typical areas near the fracture surface of the Al₃Ti/A356 composite after tensile test; (d) Particle size distribution of Al₃Ti in the Al₃Ti/A356 composite.

6.3 Modeling

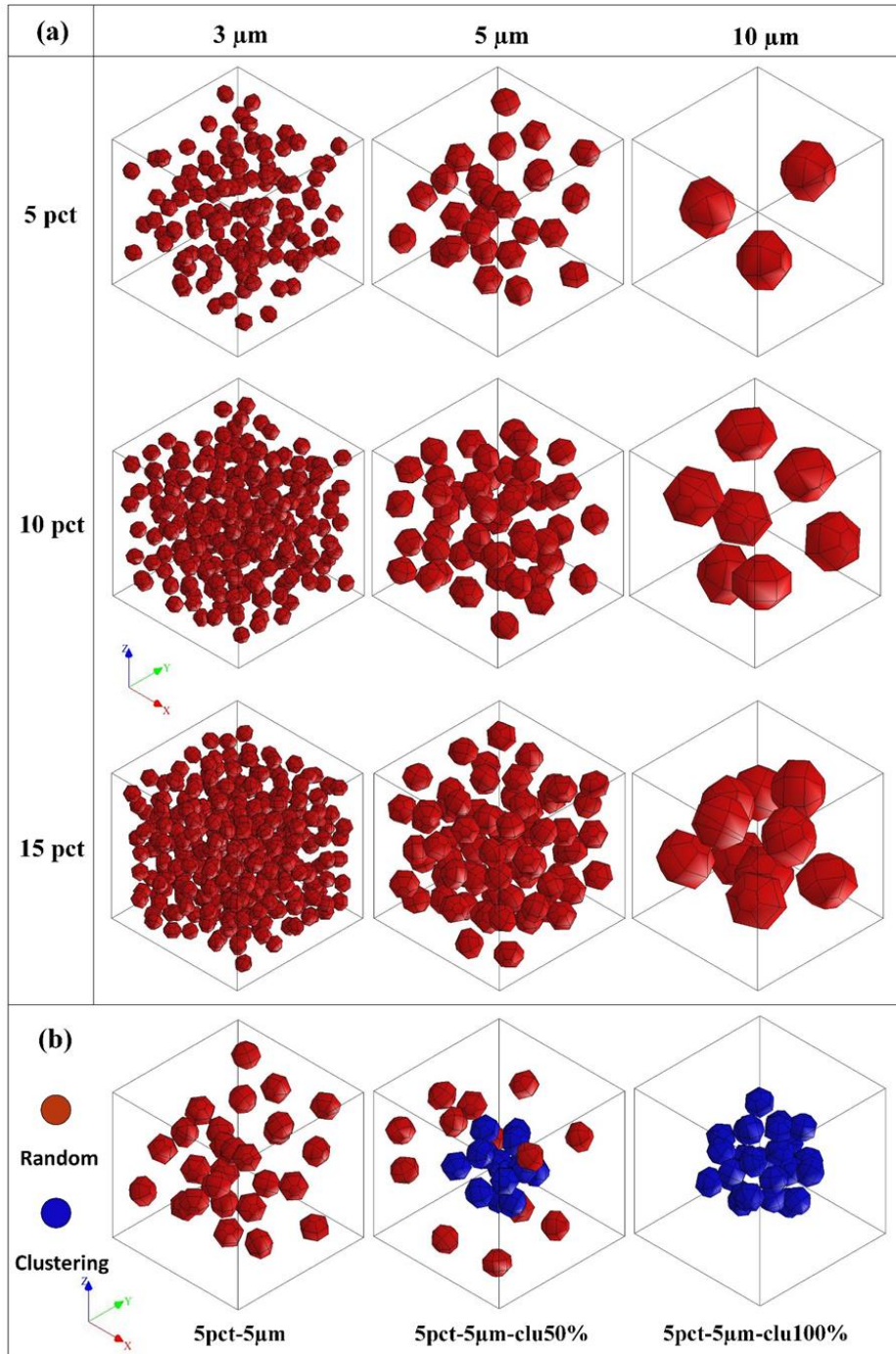


Figure 6.2. (a) Examples of 3D automatically generated RVEs containing randomly distributed Al_3Ti particles with various sizes and volume fractions. (b) 5pct-5 μm RVEs with random distribution, 50 % particle clustering, and 100 % particle clustering. (The edge length of all the RVEs in this figure is 30 μm)

Three dimensional RVEs were automatically generated using the Digimat-FE software, with dispersed Al_3Ti particles imbedded in an A356 matrix. According to the observation of in-

situ Al₃Ti particles in the current work and previous work (C. Yang et al., 2018), the morphology of most Al₃Ti particles are close to an equiaxial-polyhedron. Thereby Al₃Ti particles were generated as icosahedron shape in the RVEs for simplicity. The geometrical parameters of Al₃Ti particles are controllable, such as their size, volume fractions and distributions. The T6 treated A356 matrix was simplified as a homogenized constitution since the Si particles dispersed in α -Al are generally smaller in size compared to the Al₃Ti particles. In the present study, a series of RVEs were generated with the particle sizes of 3 μm , 5 μm and 10 μm and volume fractions of 5 %, 10 % and 15%. Both the position and the orientation of the particles were randomly selected, as shown in Fig. 6.2(a). For simplicity, these RVEs are abbreviated according to the particle size and volume fraction. For instance, “5pct-5 μm ” refers to the RVE with 5 vol. % and 5 μm -sized particles. Furthermore, to study the effects of particle clustering, one particle cluster was set in the center of a RVE model with 5 vol. % and 5 μm -sized particles (the “5pct-5 μm ” RVE) as shown in Fig. 6.2(b). In one RVE, all the particles are gathered in the cluster (noted as “5pct-5 μm -clu100%”). In the other RVE, 50 % particles are in the cluster while the rest particles are still randomly dispersed (noted as “5pct-5 μm -clu50%”). It is evident that the clustering particles have a much smaller average Nearest Neighbor Distance (NND) than those randomly distributed particles. A parameter β was used to symbolize the average NND normalized by particle size. For the clustering particles of the 5pct-5 μm -clu50% and the 5pct-5 μm -clu100% RVEs, $\beta=1.07$, while $\beta=1.606$ for the randomly distributed particles in the “5pct-5 μm ” RVE in Fig. 6.2 (b).

6.4 Micromechanical Simulation

6.4.1 Constitutive behavior

For the A356 matrix, the density, elastic modulus and Poisson’s ratio are set as 2.7 g/cm³, 69 GPa, and 0.33, respectively (Ghosh & Moorthy, 1998). An isotropic working-hardening behavior is assumed, which is described by a power law Eq. 6.1 (Dao et al., 2001).

$$\sigma = \sigma_y \left(1 + \frac{E}{\sigma_y} \varepsilon_p\right)^n \quad (6.1)$$

Where σ_y is the yield strength of the A356 matrix, taken as 216.3 MPa from tensile experiment, E is the Young’s modulus of A356, σ and ε_p are true stress and plastic strain, respectively. The

exponent n is 0.117, obtained by fitting the uniaxial tensile stress-strain curve of the matrix alloy. The elongation of the A356 matrix from tensile test is 6.7 %.

The brittle Al_3Ti phase is assumed to undergo elastic deformation solely. The density, elastic modulus and Poisson's ratio are taken as 3.3 g/cm^3 , 216 GPa, and 0.25, respectively (Fu, 1990; Zeng et al., 2018).

For the simulation of matrix/reinforcement interfacial behavior, no interfacial debonding is considered because of the strong Al/ Al_3Ti interfacial bonding based on the observation in Fig. 6.1(c) and other related work (Mohanty & Gruzleski, 1995; X. Wang et al., 2004).

6.4.2 Damage mechanisms

Therefore, only the ductile failure of matrix and the brittle failure of Al_3Ti reinforcements are involved in the simulation. A damage parameter D_η is employed to describe the ductile failure of A356 matrix, defined as Eq. 6.2, according to the work of Rice and Tracey (Rice & Tracey, 1969).

$$D_\eta = \int_0^{\bar{\epsilon}^{pl}} e^{\frac{3}{2}\eta} d\bar{\epsilon}^{pl} \quad (6.2)$$

$$\bar{\epsilon}^{pl} = \int_0^t \dot{\bar{\epsilon}}^{pl} dt, \quad \dot{\bar{\epsilon}}^{pl} = \sqrt{\frac{2}{3} \dot{\boldsymbol{\epsilon}}^{pl} : \dot{\boldsymbol{\epsilon}}^{pl}} \quad (6.3)$$

where $\eta = \sigma_m / \sigma_y$ is the stress triaxiality. σ_m is the hydrostatic stress, σ_y is the von Mises stress, $\bar{\epsilon}^{pl}$ is the equivalent plastic strain (PEEQ), and $\dot{\boldsymbol{\epsilon}}^{pl}$ is the plastic strain rate tensor. In the simulation, D_η is cumulated at each element to obtain D_η as Eq. 6.2 at a certain time during the loading. Ductile failure occurs when D_η exceeds a critical value $D_{\eta c}$. $D_{\eta c}$ was determined from a uniaxial tension FE simulation on the A356 matrix, based on the method by Kut (2010). A quarter FE model (symmetrical to x and y directions) with identical section size and gauge length as the T6-A356 tensile test sample were uniaxial tensioned. The input material properties are also from the experimental tensile curve of the T6-A356 sample. When the model was extended to a displacement corresponding to its experimental elongation, it assumes that the model was fractured. At that moment, the D_η value at the center of the section was taken as $D_{\eta c}$ for the A356 matrix, as notified in Fig. 6.3. Based on the simulation results, the $D_{\eta c}$ for the T6-A356 matrix in this work is 0.1592.

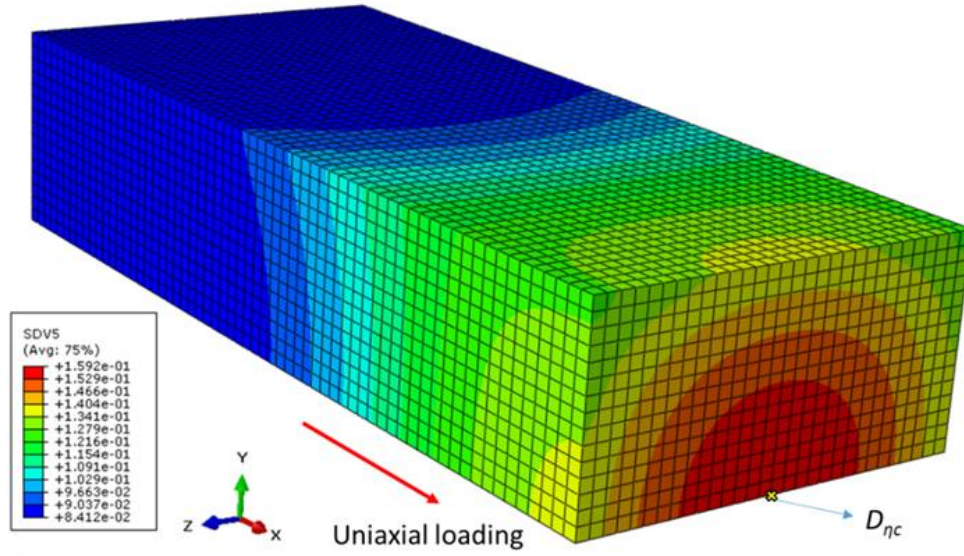


Figure 6.3. The critical value $D_{\eta c}$ of the T6-A356 matrix determined by uniaxial tensile simulation. (SDV5 in the legend refers to D_{η})

The constitutive post failure behavior plays a significant role on the numerical output stress-strain relationships after damage initiation in RVE. Tursun et al. (2006) employed an element removal method to simulate the damage of composites. The stiffness of a constitutive element is directly removed when it meets the damage criterion without applying the damage evolution law. This method can clearly show the crack paths inside RVEs. However, the predicted stress-strain curves show an evidently underestimation of the flow stress than the experiment response, when the element removal occurs. Therefore, it is not accurate to directly remove the damaged element to predict the stress field of RVE after damage initiation. As a result, damage evolution law is employed to describe the constitutive post failure behavior in this study.

For the ductile failure of matrix, the post failure behavior can be simulated as a weakening of finite elements by decreasing its stiffness (Young's modulus). A linear damage evolution law is adopted for this with a damage parameter d , defined as Eq. 6.4 (Qing, 2013b).

$$d = \min\left(1, k_d \frac{\varepsilon_{eq} - \varepsilon_0}{\varepsilon_0}\right) \quad (6.4)$$

where ε_0 and ε_{eq} refer to the initial equivalent failure strain and the current equivalent strain, respectively. k_d is a parameter controlling the degradation speed of material's stiffness. If d of a

certain element reaches 1, the element will be removed as its stiffness reduces to zero. The ductile failure and post failure behavior above were realized using an Abaqus/Explicit subroutine VUSDFLD.

For the brittle failure of Al₃Ti, the “brittle cracking” model in Abaqus/Explicit is employed to describe the brittle failure of SiC particles, as applied by J. Zhang et al. (2016). In this model, the crack initiation is detected using a simple Rankine criterion based on Mode I fracture considerations. The criterion states that crack occurs when the maximum principal tensile stress exceeds the tensile strength of Al₃Ti particles (σ_f^p).

Both Mode I (tension softening/stiffening) and Mode II (shear softening/retention) are taken into account for the ensuing post failure behavior. For Mode I, the reduction of stiffness is described by a linear evolution law with an ultimate fracture strain e_f^{cr} . For Mode II, the reduction of shear modulus G is calculated by a function D of the fracture strain e^{ck} as a part of total strain (Eq. 6.5).

$$D(e^{ck}) = \alpha(e^{ck})G \quad (6.5)$$

where the shear retention parameter α is defined as:

$$\alpha(e^{ck}) = \frac{\rho(e^{ck})}{\rho(e^{ck})-1} \quad (6.6)$$

$$\rho(e^{ck}) = \left(1 - \frac{e^{ck}}{e_{max}^{ck}}\right)^p \quad (6.7)$$

where p and e_{max}^{ck} are parameters used to control the shear retention. For parameters in the “brittle cracking” model, $\sigma_f^p \approx 800$ MPa according to the fracture strength of an Al₃Ti + 0.3 % Al alloy (Z. Lu et al., 2016); p is set as 1, assuming a linear damage evolution for the post cracking behavior of Mode II for simplicity. Due to a lack of experimental data on Al₃Ti particles, the parameters k_d , e_f^{cr} and e_{max}^{ck} are obtained by fitting the tensile stress-strain curve of 5 vol. % Al₃Ti/A356 composites from the uniaxial tensile result. It is suggested that the ratio of e_f^{cr} and e_{max}^{ck} is 1:10 for SiC particles according to J. Zhang et al. (2016). For simplicity, the ration is also employed for

the Al₃Ti particles here. Different parameter combinations have been tried for obtaining the optimum results, which will be discussed in the Section 6.5.1.

6.4.3 Loading and Boundary conditions

All the generated RVEs in Fig. 6.2 were subsequently meshed in the Abaqus/CAE software with the general linear 3D solid elements (C3D4). Initially, the effects of RVE size, mesh density and model variation were investigated in order to determine a proper parameter combination as a prerequisite for further simulation, which will be discussed in Section 6.5.1.

To simulate the uniaxial tensile process of Al₃Ti/A356 composites, the face of RVE on the y-z plane was fixed with no displacement in the x-direction ($U_x=0$) and the opposite surface was subjected to a linearly increasing displacement along x-direction. Meanwhile, all the rotation degree of the nodes on the two surfaces were fixed to guarantee the stability of the model after fracture happens, as suggested by J. Zhang et al. (2016). No constrains were exerted on the other four faces parallel to the tensile direction. The schematic image of loading and boundary conditions is shown in Fig. 6.4.

Finally, the simulation of the RVE models were conducted in Abaqus/Explicit. The nominal stress and strain of the RVE were calculated by the following equations:

$$\sigma_{nom} = \frac{\sum_1^N f_{RF}}{L^2} \quad (6.8)$$

$$\varepsilon_{nom} = \frac{\Delta x}{L} \quad (6.9)$$

where f_{RF} is the reaction force at the nodes on the loading face, N is the total number of the nodes on the loading surface, L is the initial edge length of RVE, and Δx is the displacement along the loading direction. The maximum ε_{nom} is 0.08.

Additionally, the stress partition behavior in the constitutive phases (A356 matrix, Al₃Ti) were studied. Since the loading is along the x direction, the S11 component of the stress tensor were obtained from each constitutive phases by averaging the S11 values of all the elements in the segment V of corresponding phase with the first homogenization strategy by Eq. 6.10 (Zhou et al., 2015).

$$\overline{s_{11}} = \frac{1}{V} \int_V s_{11} dV \quad (6.10)$$

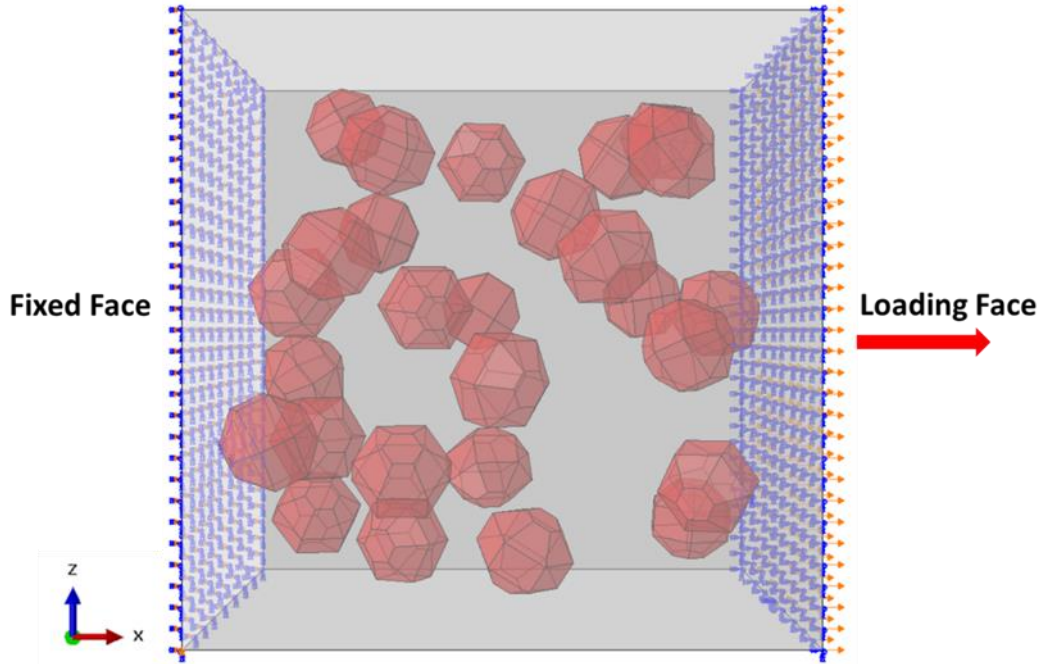


Figure 6.4. Schematic image of loading and boundary conditions on the 3D RVEs.

6.5 Simulation Results

6.5.1 Model validation

To validate the numerical simulation with RVE models, it is common to compare the predicted nominal stress-strain curves with the experimental results. Here, the 5pct-5 μ m RVE as Fig. 6.2(a) was employed for comparison with the fabricated 5 vol. % Al₃Ti/A356 composite in this study, since they possess similar average Al₃Ti particle size and volume fraction. Firstly, the parameters k_d , e_f^{cr} and e_{max}^{ck} as mentioned in Section 6.4.2 above were numerically extrapolated from fitting the experiment stress-strain curve. Fig. 6.5 shows the simulation stress-strain curves with different combinations of parameters. It is shown that k_d leads to an obvious stress discrepancy when the strain exceeds 0.03, while e_f^{cr} and e_{max}^{ck} influence the strain when the stress begins to drop. The combination of $k_d=1$, $e_f^{cr}=0.08$ and $e_{max}^{ck}=0.008$ gives the closest match between a calculated curve and experimental curve for the Al₃Ti/A356 composites. As a result, this combination of parameter will be used in the following simulations.

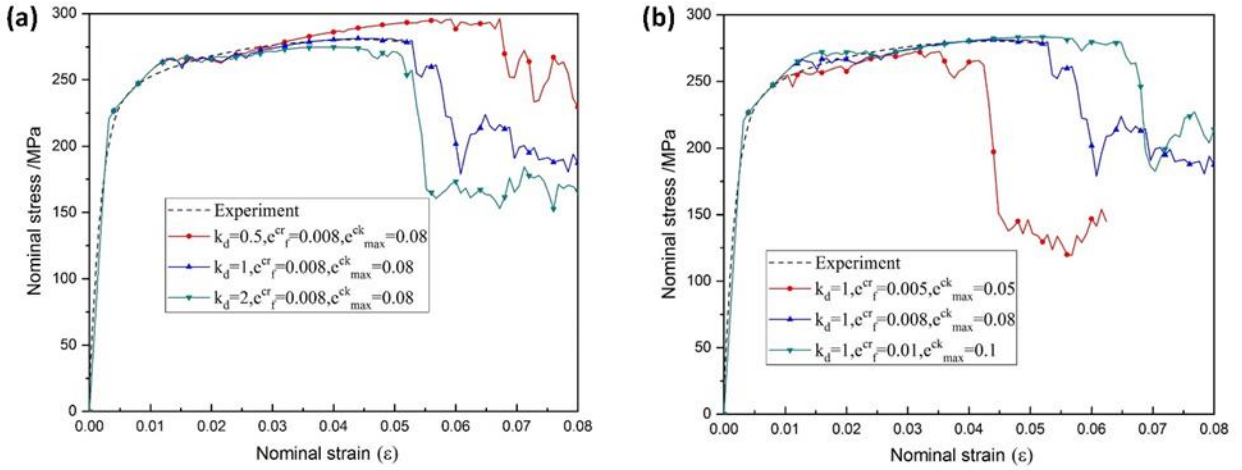


Figure 6.5. Effect of (a) the parameter k_d and (b) e_f^{cr} and e_{max}^{ck} on the obtained nominal stress-strain curves from RVE simulation.

Secondly, the effects of RVE size, mesh dependence and model variation are studied. The effects of RVE size were conducted on a 5pct-5 μ m RVE with RVE edge lengths of 20 ~ 50 μ m for example. The simulated stress-strain curves are shown in Fig. 6.6(a). The curves present no obvious difference with each other below a certain strain where the nominal stress suddenly drops down. Here, the strain is defined as a fracture strain (ϵ_f), also as the “elongation” of for a certain RVE, comparative to the elongation in experimental tensile test. It can be seen that the stress drops gradually and fluctuates when the strain exceeds ϵ_f , which is different from uniaxial tensile test that the stress drops quickly to zero. A similar phenomenon is observed by other investigators (J. Zhang et al., 2016). One reason is the application of linear damage evolution law in each element. The stress of the failure elements cannot drop to zero directly. Another reason is that the stress-state of a real tensile sample after the necking is complex and cannot be simply simulated with the boundary conditions on a RVE as Fig. 6.4 (Hu et al., 2008). Therefore, the rapid damage evolution in the real tensile test after necking cannot be well described with the current model. As a result, the determination of ϵ_f on the simulated stress-strain curves in RVE is based on a phenomenological method. In the simulation, the maximum loading ($\epsilon_{nom}=0.08$) is equally divided into 100 frames (i.e. 100 output data points on a simulated stress-strain curve). The ϵ_f is determined by calculating the relative decrease of stress to between two neighbor points: $\Delta\sigma =$

$(\sigma_{i+1} - \sigma_i)/\sigma_i$, i is the number of a certain data point. If $\Delta\sigma < -5\%$, it indicates that the sudden drop of stress occurs at this point. The nominal strain of Point i is ϵ_f , as presented in Fig. 6.6(d).

Apart from the 5pct-5 μm RVE, the RVE size effect is also conducted for two other kinds of RVEs, 5pct-10 μm and 10 pct-10 μm RVEs. The results indicate that when RVE length exceeds 30 μm , the simulated curves also show little difference. As to the other RVE models in Fig. 6.2(a), they contain the more particles than 5pct-10 μm and 10pct-10 μm RVEs. The minimum RVE size for simulation is decreased with the increase of particle number in a RVE, as suggested by X. X. Zhang et al. (2014). Thus, 30 μm RVE length is also applicable for all the models in Fig. 6.2(a). From all above, the edge length of RVE is chosen as 30 μm in this study by considering the balance of computational accuracy and cost, as well as ensuring enough particles in each RVE model.

Fig. 6.6(b) shows simulated stress-strain curves with three different mesh densities (initial seed size=1.25 μm , 1 μm and 0.75 μm). There are no obvious differences between these curves. Then, three randomly generated 5pct-5 μm RVEs are simulated to study the model variability. As shown in Fig. 6.6(c), the output curves are almost in coincidence with each other. Only slight discrepancy in the elongation is in presence.

In the following simulation, the initial mesh seed size is selected as 1 μm . The total number of elements in each model is in the range of $1 \times 10^5 \sim 2 \times 10^5$. For each kind of RVE in Fig. 6.2, three models were simulated to reduce the error caused by the model variability. With these parameters, the simulated stress-strain curve of a 5pct-5 μm RVE is in a good agreement with the experimental result of $\text{Al}_3\text{Ti}/\text{A356}$ composites in Fig. 6.6(d). Similar to the stress-strain curve from uniaxial tensile test, the simulated stress-strain curve also shows a typical process of elastic deformation, work hardening and failure, as divided in Fig. 6.6(d). The Young's modulus, yield stress (YS, taken at 0.2 % residual plastic strain), and elongation (ϵ_f) of the composites were measured from each simulated stress-strain curve, for predicting the mechanical properties of $\text{Al}_3\text{Ti}/\text{A356}$ composites with different microstructures.

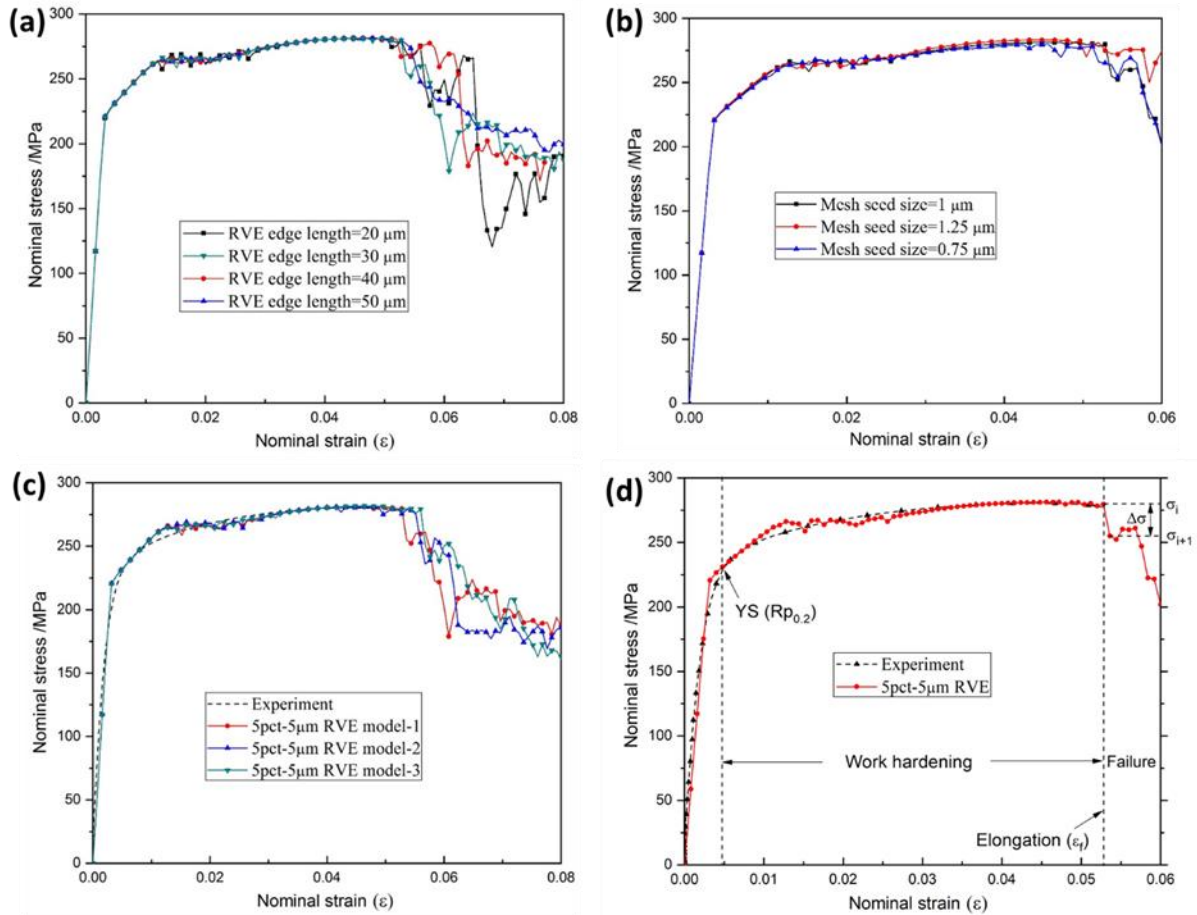


Figure 6.6. Effect of (a) the selected RVE edge length; (b) mesh density; and (c) model variation on the simulation nominal stress strain curves; (d) comparison between the nominal stress-strain curves from 5pct-5 μm RVE and from experimental uniaxial tensile test.

6.5.2 Effect of particle size

The simulated stress-strain curves of RVEs with different particle sizes are compared in Figs. 6.7(a1)~(a3), with the volume fractions of particles 5, 10 and 15 % respectively. It is clear that with the same volume fraction of reinforcing particles the YS of the composite increases slightly as particle size decreases. However, the increase of particle size reduces the elongation significantly.

Figs. 6.7(b1)~(b3) show the average S11 stress component of Al_3Ti and A356 matrix phases corresponding to the RVEs in Figs. 6.7(a1)~(a3), respectively. In general, smaller-sized Al_3Ti particles can evidently undertake higher S11 stress at the beginning of deformation. Meanwhile, the stress states of the matrix show no obvious difference in the figures. As a result,

the difference of YS among the RVEs is mainly attributed to the average S11 undertaken by Al_3Ti . As the nominal strain raises, the average S11 on Al_3Ti reaches a peak and then drops linearly. The linear stress drop on Al_3Ti indicates that brittle cracking occurs and follows a linear damage evolution law as described in Section 6.4.2 above. It is observed that the average S11 of smaller Al_3Ti particles reaches a higher peak at a lower strain and seems to drop faster than that of larger Al_3Ti . With further loading, the stress on the Al_3Ti particles remain unchanged, while the strengthening of matrix continues to increase until a certain strain referring to the elongation (ϵ_f) of corresponding RVE model. In addition, the average S11 of the matrix drops at a larger strain in the RVEs with smaller particle size, resulting in higher elongation.

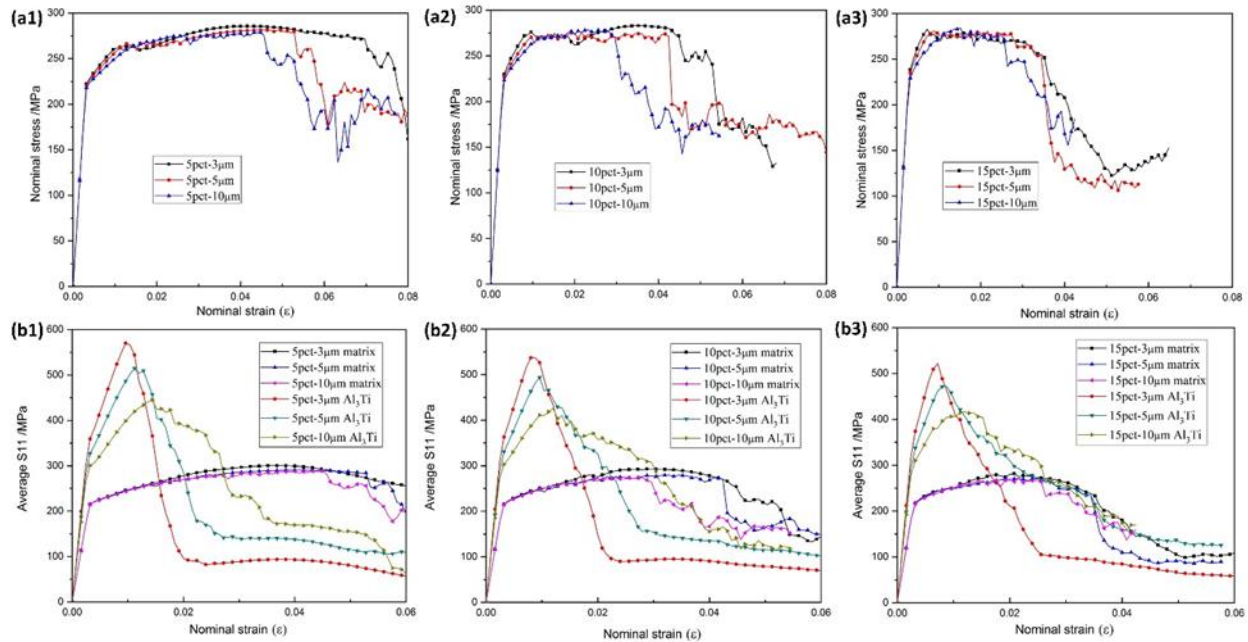


Figure 6.7. (a1)~(a3) simulation stress-strain curves of 5pct-3, 5, and 10 μm RVEs, respectively. (b1)~(b3) the average S11 stress component of Al_3Ti and A356 matrix phases corresponding to the RVEs in Figs. 6.7(a1)~(a3), respectively.

The simulated stress-strain curves of RVEs with different particle sizes are compared in Figs. 6.7(a1)~(a3), with the volume fractions of particles 5, 10 and 15 % respectively. It is clear that with the same volume fraction of reinforcing particles the YS of the composite increases slightly as particle size decreases. However, the increase of particle size reduces the elongation significantly.

Figs. 6.7(b1)~(b3) show the average S11 stress component of Al₃Ti and A356 matrix phases corresponding to the RVEs in Figs. 6.7(a1)~(a3), respectively. In general, smaller-sized Al₃Ti particles can evidently undertake higher S11 stress at the beginning of deformation. Meanwhile, the stress states of the matrix show no obvious difference in the figures. As a result, the difference of YS among the RVEs is mainly attributed to the average S11 undertaken by Al₃Ti. As the nominal strain raises, the average S11 on Al₃Ti reaches a peak and then drops linearly. The linear stress drop on Al₃Ti indicates that brittle cracking occurs and follows a linear damage evolution law as described in Section 6.4.2 above. It is observed that the average S11 of smaller Al₃Ti particles reaches a higher peak at a lower strain and seems to drop faster than that of larger Al₃Ti. With further loading, the stress on the Al₃Ti particles remain unchanged, while the strengthening of matrix continues to increase until a certain strain referring to the elongation (ϵ_f) of corresponding RVE model. In addition, the average S11 of the matrix drops at a larger strain in the RVEs with smaller particle size, resulting in higher elongation.

Fig. 6.8(a) shows the S11 stress component distributions on the Al₃Ti particles. It is shown clearly that most 3 μ m-sized particles take the highest S11 at a nominal strain of 0.8 % close to the yield point. However, 5 μ m and 10 μ m-sized particles take a generally lower S11 at this strain. The results are in agreement with Figs. 6.7(b1)~(b3). Then as a nominal strain increases from 0.8% to 1.2 %, S11 taken by each particle keeps increasing until its maximum principle stress exceeding the critical value (σ_f^p), indicating the occurrence of brittle damage. Thereafter the S11 drops on the damaged particles, as shown by a blue color in Fig. 6.8(a). From comparison, S11 increases the most on each 3 μ m particle, so that a couple of them are already brittle damaged, while for the 5 μ m and 10 μ m-sized particles, the S11 increase are moderate and much fewer particles are damaged. As a result, it indicates that the average S11 on smaller particle can reach the peak faster and higher. And the stress also drops earlier due to occurrence of brittle damage, which is agree with the results in Fig. 6.7(b1). Therefore, it is evidence that smaller particles are prone to “being strengthened” faster and undertaking higher average S11 than the larger ones statistically from Figs. 6.7(b1)~(b3) and Fig. 6.8(a).

The damage parameter D_η distribution in matrix at different nominal strains for the 5pct RVEs is presented in Fig. 6.8(b). In each model, D_η accumulates quickly in a region around reinforcing particles. As loading increases, damage initiates in these regions. Subsequently, the damage zones expand and coalesce with each other, as shown in the third column of Fig. 6.8(b).

The figure shows that the damage evolution in matrix with smaller particles is slower and uniform, while damage in the matrix develops around larger particles under the same nominal strain. As a consequence, RVEs with larger particles are prone to damage, which is in agreement with the earlier drop of S_{11} in the matrix of Fig. 6.7(b1) and the lower elongation as presented in Fig. 6.7(a1).

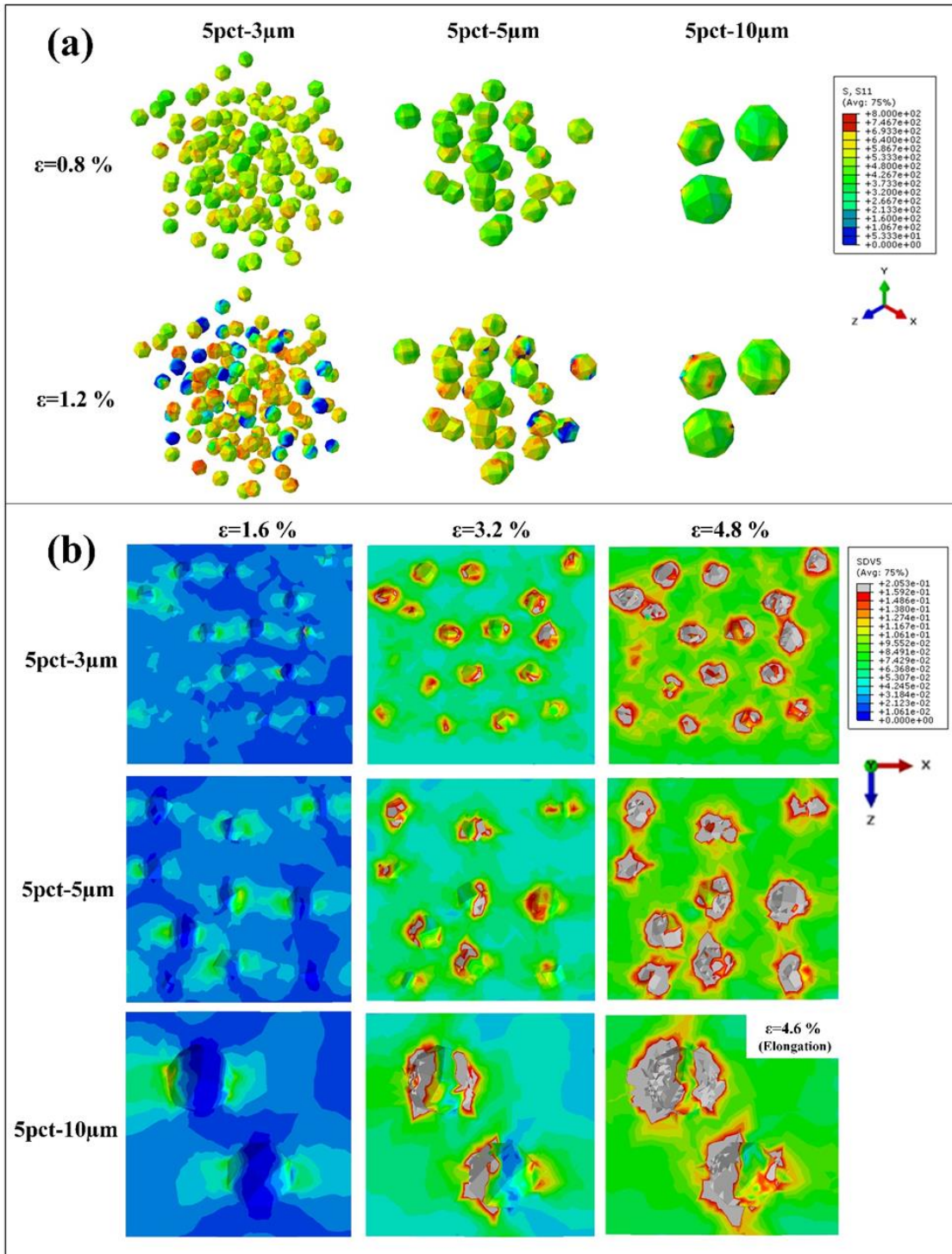


Figure 6.8. (a) S11 stress component distributions on the Al_3Ti particles at different nominal strains of 5pct-3, 5, and $10\mu\text{m}$ RVEs; (b) The matrix damage parameter D_η distribution at different nominal strains of 5pct-3, 5, and $10\mu\text{m}$ RVEs (A section on X-Z plane is shown for each model. D_η of the gray colored elements here has exceeded the critical value $D_{\eta c}$, indicating that damage has already occurred on those elements. It is also applicable for Figs. 6.10(b) and 6.12(b)).

6.5.3 Effect of particle fraction

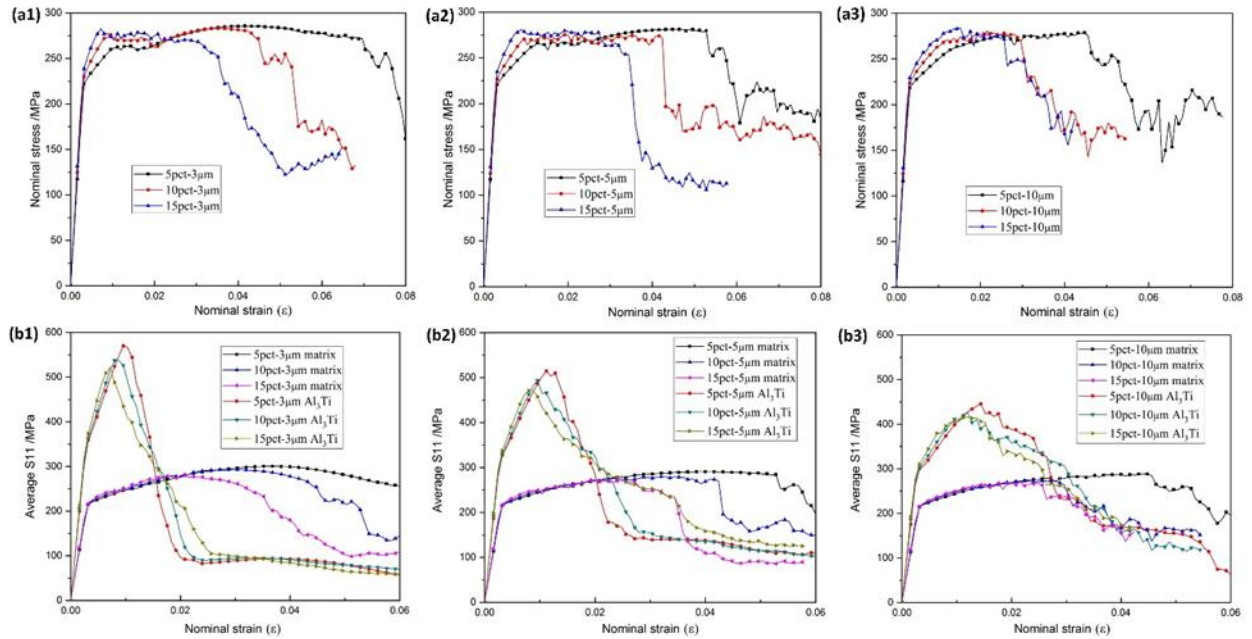


Figure 6.9. (a1)~(a3) The simulation stress-strain curves of of 5, 10, and 15pct-5 μm RVEs, respectively. (b1)~(b3) The average S11 stress component of Al₃Ti and A356 matrix phases corresponding to the RVEs in Figs. 6.9(a1)~(a3), respectively.

Figs. 6.9(a1)~(a3) compare the simulated stress-strain curves of RVEs with different particle volume fractions with the particle size of 3, 5 and 10 μm , respectively. The YS is improved while the elongation is deteriorated apparently from each figure with the increase of the volume fraction of particles. The average S11 stress component of Al₃Ti and A356 matrix are shown in Figs. 6.9(b1)~(b3), corresponding to the RVEs in Figs. 6.9(a1)~(a3), respectively. As the strain near the yield point ($\epsilon=0.8\%$), Al₃Ti in each RVE take similar average S11 regardless of particle fraction. In addition, in the RVEs with a lower fraction of particles, the peak value of average S11 on Al₃Ti increases and drops at a certain larger strain. Furthermore, the drop of stress in the matrix is delayed.

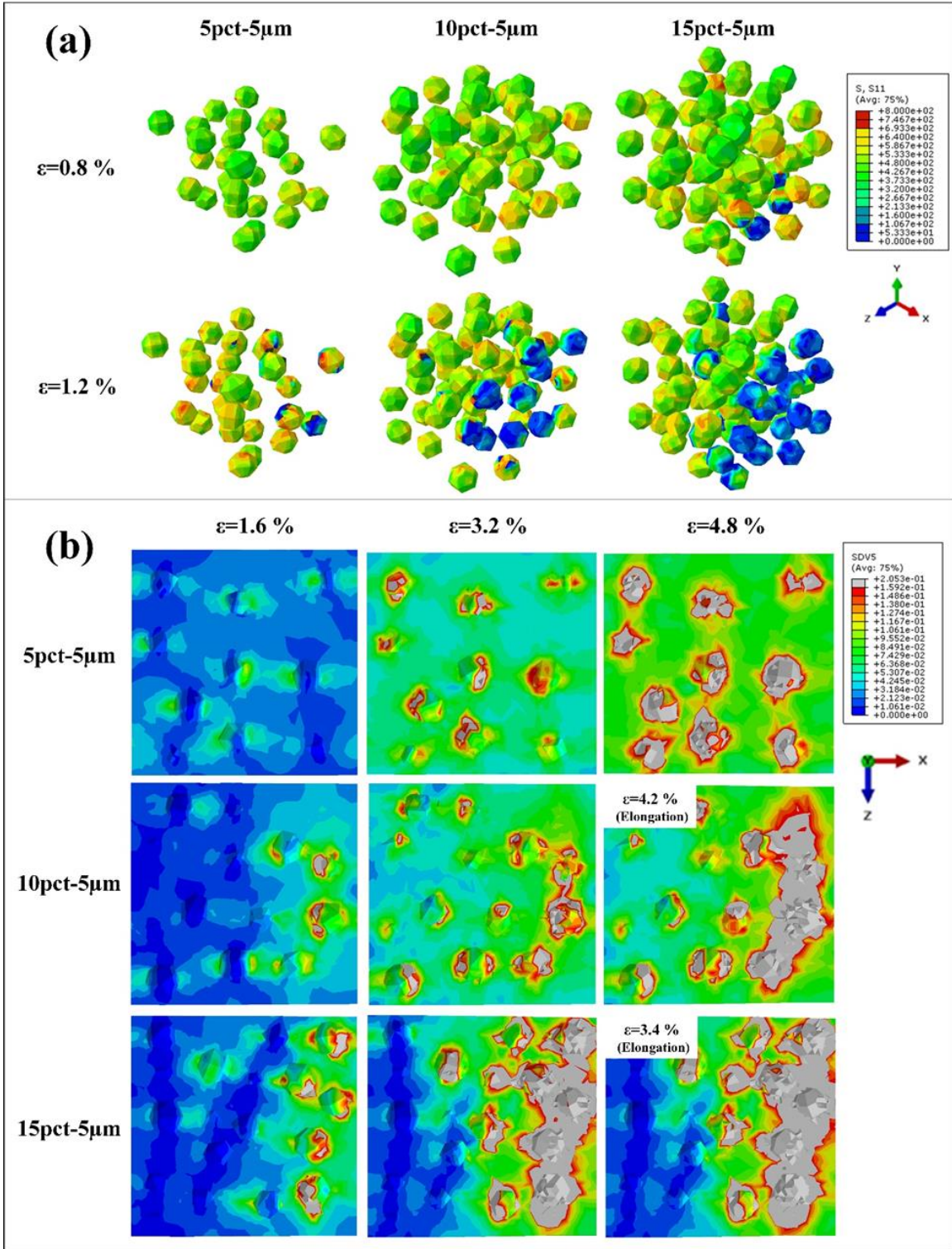


Figure 6.10. (a) S11 stress component distributions on the Al_3Ti particles at different nominal strains of 5, 10, and 15pct-5µm RVEs; (b) The matrix damage parameter D_η distribution at different nominal strains of these three RVEs.

The S11 stress component and matrix damage parameter D_η distributions at different nominal strains of 5, 10, and 15pct-5 μ m RVEs are compared in Figs. 6.10(a) and (b). From Fig. 6.10(a), at a nominal strain of 0.8 % (close to the yield point), some particles undertake higher S11 due to stress concentration, since the space between the particles is reduced at a larger particle fraction. Especially, brittle damage even occurs on some particles at this strain in 15pct-5 μ m RVE due to severe stress concentration. As the strain increases to 1.2 %, it is clear that a large portion of particles are damaged in RVEs with a higher particle fraction. The results suggest that particles are more likely to be damaged if the total particle fraction increases. From damage evolution in matrix in Fig. 6.10(b), the increase of particle fraction facilitates the damage of matrix, because of severe stress concentration and more interfacial zones where matrix damage initiates.

6.5.4 Effect of particle distribution

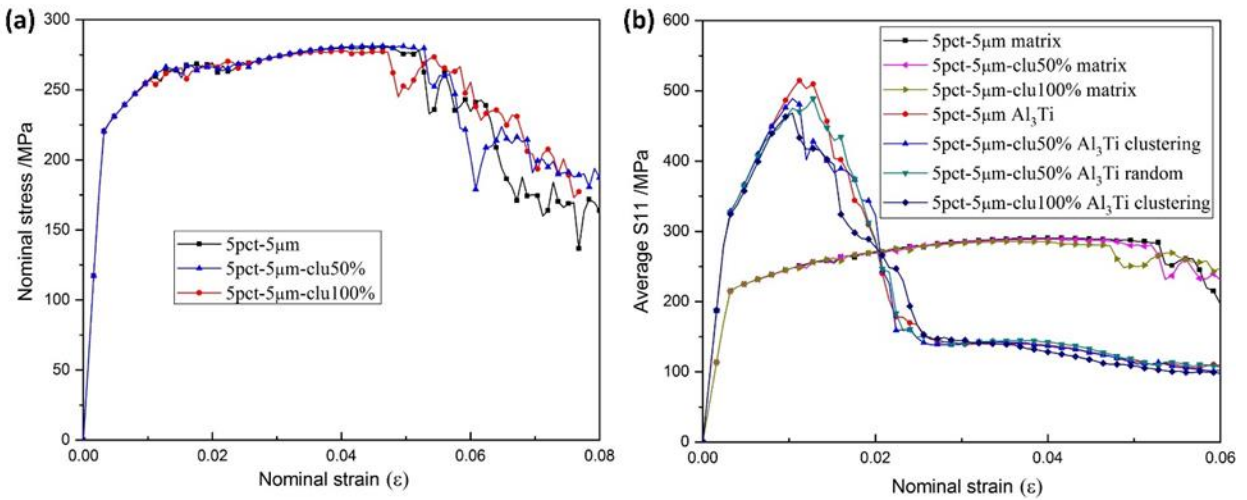


Figure 6.11. (a) Simulation stress-strain curves of 5pct-5 μ m, 5pct-5 μ m-clu50% and 5pct-5 μ m-clu100% RVEs, respectively. (b) The average S11 stress component of Al₃Ti and A356 matrix phases corresponding to the RVEs in Figure 6.11(a), respectively.

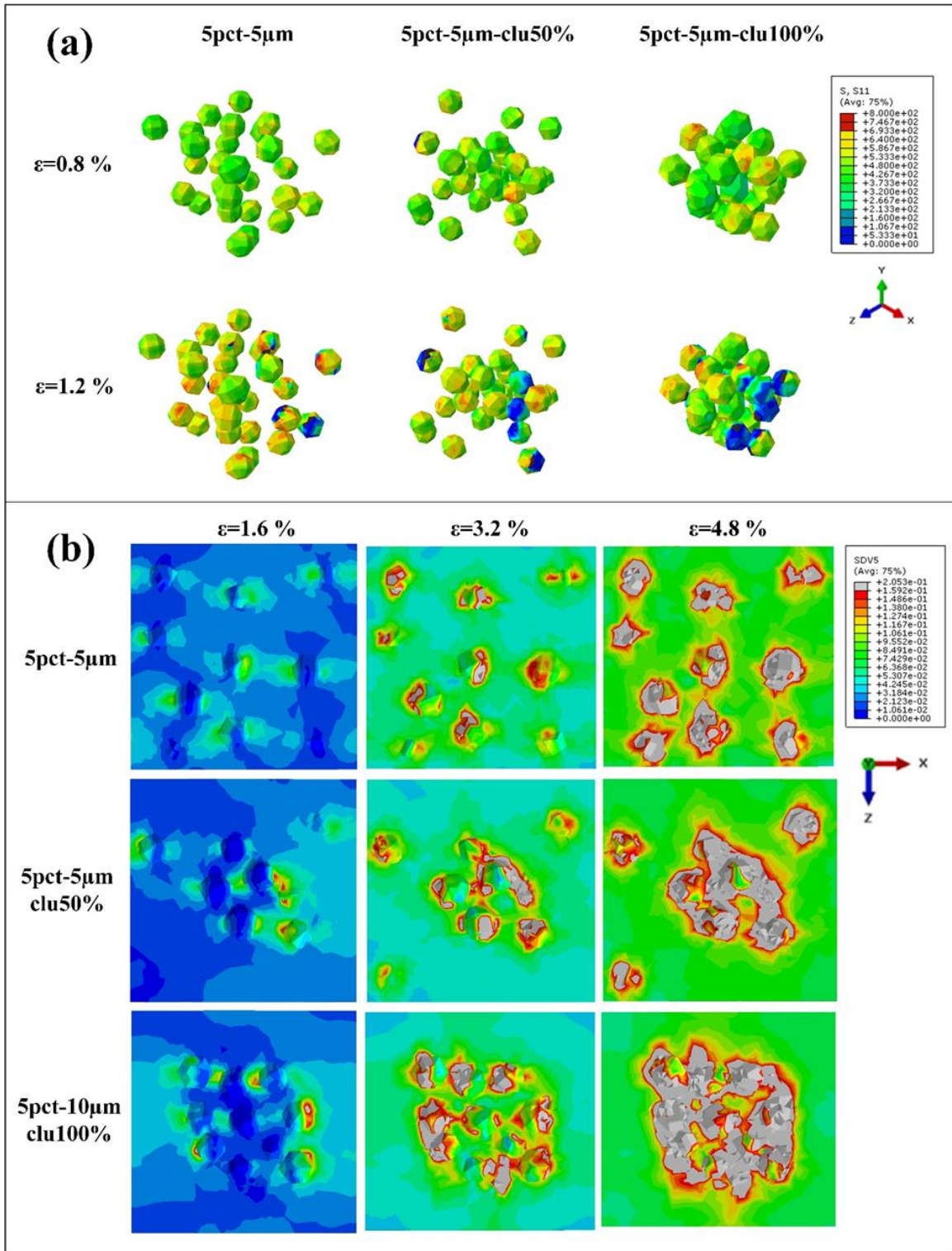


Figure 6.12. (a) S11 stress component distributions on the Al₃Ti particles at different nominal strains of 5pct-5 μ m, 5pct-5 μ m-clu50% and 5pct-5 μ m-clu100% RVEs; (b) The matrix damage parameter D_7 distribution at different nominal strains of these three RVEs.

Fig. 6.11(a) compares the simulated stress-strain curves of 5pct-5 μ m RVEs with a random particle distribution, 50 % particle clustering and 100 % particle clustering at the center of the model as shown in Fig. 6.2(b). It is clear that the simulated curves show no obvious differences until a large strain close to the elongation of each RVE. The RVE with more clustering particles has lower elongation. From the constitutive stress-strain curves in Fig. 6.11(b), the peak value of average S11 on randomly distributed Al₃Ti is the highest and drops at a much larger strain than the clustering particles. In addition, S11 of the matrix drops at a smaller strain in the RVEs with clustering particles. Fig. 6.12(a) shows the distributions of S11 stress component on the Al₃Ti particles at different nominal strains of the three models, respectively. It is also shown that the clustering of particles results in stress concentration and are prone to damage due to a small NND. Therefore, clusters of particles cannot bear a high stress as random dispersed particles. From the matrix damage parameter D_η distribution of the three models in Fig. 6.12(b), the particle clustering facilitates the damage in matrix, especially in the vicinity of the particle clustering zone, and the effect becomes stronger as the particle clustering becomes more severe (from 50 % to 100 %).

6.6 Discussions

The mechanical properties the Al₃Ti/A356 composite are predicted from the simulated stress-strain curves in Fig. 6.13 based on the RVEs. Theoretically, the Young's modulus of particle reinforced composites can be predicted using the Tsai-Halpin equation (Eqs. 2.4 and 2.5), Where E_p and E_m are the Young's modulus of Al₃Ti (216 GPa) and A356 matrix (69 GPa), respectively. s is the aspect ratio of particle, assumed as 1 because all the particles are icosahedron-shaped. V_p is the volume fraction of particles. The predicted Young's modulus of the RVEs with different microstructures are compared with the theoretical values calculated by Eqs. 2.4 and 2.5. It is shown that the predicted Young's modulus values from simulation are generally in good agreement with the results of the Tsai-Halpin equation, as shown in Fig. 6.13(a).

The yield strength of the Al₃Ti/A356 composites can be predicted with the modified shear-lag model in theory as Eq. 6.11 (Y Li et al., 2009; Nardone & Prewo, 1986; Sekine & Chent, 1995).

$$\sigma_c = \sigma_m \left[V_p \left(1 + \frac{s}{2} \right) + (1 - V_p) \right] \quad (6.11)$$

Where σ_c and σ_m are the yield strength of the composite and matrix, respectively. σ_m is 216.3 MPa for the A356 matrix. s is aspect ratio of Al₃Ti particle, taken as 1. V_p is also the volume fraction of Al₃Ti. It is seen that Eq. 6.11 does not involve the effects of particle sizes.

Another broadly applied approach for predicting YS is a micromechanics approach, which attributes several strengthening mechanisms to the particle reinforced composites: load-bearing strengthening $\Delta\sigma_{\text{Load}}$, grain refinement strengthening $\Delta\sigma_{\text{gf}}$, coefficient of thermal expansion (CTE) mismatch strengthening $\Delta\sigma_{\text{CTE}}$, as well as Orowan strengthening $\Delta\sigma_{\text{Orowan}}$. The grain refinement strengthening is normally expressed by the Hall-Petch relationship. For the current work, the decrease in grain size by Al₃Ti addition is negligible because the average dendritic cell sizes of A356 matrix and Al₃Ti/A356 composites are very close to each other. On the other hand Al alloys also have a low Hall-Petch coefficient ($k=68 \text{ MPa}\cdot\mu\text{m}^{-0.5}$) (M. Wang et al., 2014). Therefore, the grain size has a limited influence on the change of the yield strength. As to Orowan strengthening, the particle size should be smaller than 1 μm to activate this mechanism. However, the Al₃Ti particles in the composites are mostly larger than 1 μm . Thus, the effect of Orowan strengthening is also minor and is not considered in the current study. Therefore, from all above, the YS of the Al₃Ti/A356 composites can be calculated as Eq. 6.12:

$$\sigma_c = \sigma_m + \Delta\sigma_{\text{Load}} + \Delta\sigma_{\text{CTE}} \quad (6.12)$$

The load bearing strengthening ($\Delta\sigma_{\text{Load}}$) refers to the load transfer to the reinforcement through the interface between Al₃Ti reinforcement and the matrix. As a result, the applied load to reach the yielding point is improved in the composites. The strengthening effect of $\Delta\sigma_{\text{Load}}$ can be calculated by Eq. 2.6, where σ_m is also YS of A356 matrix and V_p is the volume fraction of Al₃Ti.

The CTE mismatch strengthening is caused by the formation of geometrically necessary dislocations (GND) accommodating the mismatch in coefficient of thermal expansion between Al₃Ti and matrix during cooling. Its contribution is predicted by Eqs. 2.7 and 2.8, where E_m and ν are Young's modulus and Poisson's ratio of alloy matrix, respectively; A is a constant that equals to 12; $\Delta\alpha$ is the CTE difference between the A356 matrix and Al₃Ti; ΔT is the difference between quenching temperature and room temperature; d_p is the average Al₃Ti particle size; The values of these parameters in the current study are given as: $b = 0.286 \text{ nm}$; $\Delta\alpha = 11 \times 10^{-6} \text{ K}^{-1}$ (Z. Liu et al., 2018); $\Delta T = 510 \text{ K}$; d_p equals to the corresponding average Al₃Ti size. From the expressions of

Eqs. 2.6, 2.7 and 2.8, it is seen that the load-bearing strengthening is not dependent on particle size, while the CTE mismatch strengthening is increased with refinement of particle size in the micromechanics approach.

The predicted YS from RVEs are compared with the calculated results from modified shear-lag model (Eq. 6.11) and micromechanical approach (Eq. 6.12), as presented in Fig. 6.13 (b). It is seen that the predicted YS values of the composites from simulation in this study are particle size dependent and obvious higher than those obtain from modified shear-lag model, which neglects the particle size effect. Comparatively, the predicted YS values are generally close to the calculated results from the micromechanics approach, which is particle size dependent.

Based on Sections 6.5.2 and 6.5.4 above, the average S11 stress component in the matrix is nearly not affected by particle size or distribution at yield point, as illustrated in Fig. 6.7(b1) and Fig. 6.11(b1). That is in agreement with the research of others (Q. Liu et al., 2018). In this work, the simulation results indicate that small-sized particles can undertake more S11 from Figs. 6.7(b1)~(b3) and Fig. 6.8(a). Therefore, the particle size effects on the YS of the composites are attributed to the difference of load bearing ability among Al₃Ti particles of different sizes.

From related simulation work on MMCs (Q. Liu et al., 2018; Shao et al., 2011; Sung et al., 2009), it is believed that the vicinity of interface between particles and matrix suffers stress and strain concentration. Near the particle-matrix interfacial zones, the ductile matrix could be easily deformed since the elastic modulus of aluminum matrix is small and it has good plasticity for large deformation. However, Al₃Ti particles have high modulus and the Al₃Ti elements of near the interface have to experience elastic deformation to maintain the bonding with matrix and thereby result in high local stress. For a certain volume fraction of equiaxed reinforcement particles, the total interfacial area is inversely proportional to the particle size. Therefore, smaller particles can create more interfacial area, which indicates more Al₃Ti elements at the vicinity of interface could be strengthened. Therefore, smaller particles can bear more loads in the composites at the yield point.

However, it should be noted that in this study, a classical plasticity model is employed for the matrix of RVEs. For a better prediction of YS, the effect of CTE mismatch induced GNDs in the micromechanical approach should also be considered, as suggested from related simulation works (Ramazani, Mukherjee, Schwedt, et al., 2013; Shao et al., 2011; Sung et al., 2009; J. F. Zhang et al., 2018). For instance, J. F. Zhang et al. (2018) assumed CTE mismatch induced GNDs

as part of the background dislocation density distributed over the entire composite matrix volume. The CTE strengthening contribution ($\Delta\sigma_{CTE}$) is directly added to the flow behavior of matrix. However, the assumption is not accurate for low particle volume fraction ($< 25\%$), since the CTE mismatch affected zone is smaller in size than the entire matrix zone. Others illustrated that CTE mismatch induced GNDs are mainly distributed at a dislocation punched zone around the particle (Shao et al., 2011; Sung et al., 2009). An intermediate layer is employed to simulate the punched zone between matrix and reinforcements in these researches. The simulated stress-strain curves are in well agreement with experimental data. Despite the limitation of the 3D-RVE models in this study, the particle size effects on the YS of composites are still obviously shown from the fact that smaller particles bear more loads in the composites at the yield point due to an increase of interfacial areas. And the predicted YS values of the composites from the RVEs show a slight discrepancy with theoretically calculation by the micromechanical approach and more accuracy compared to the modified shear lag model.

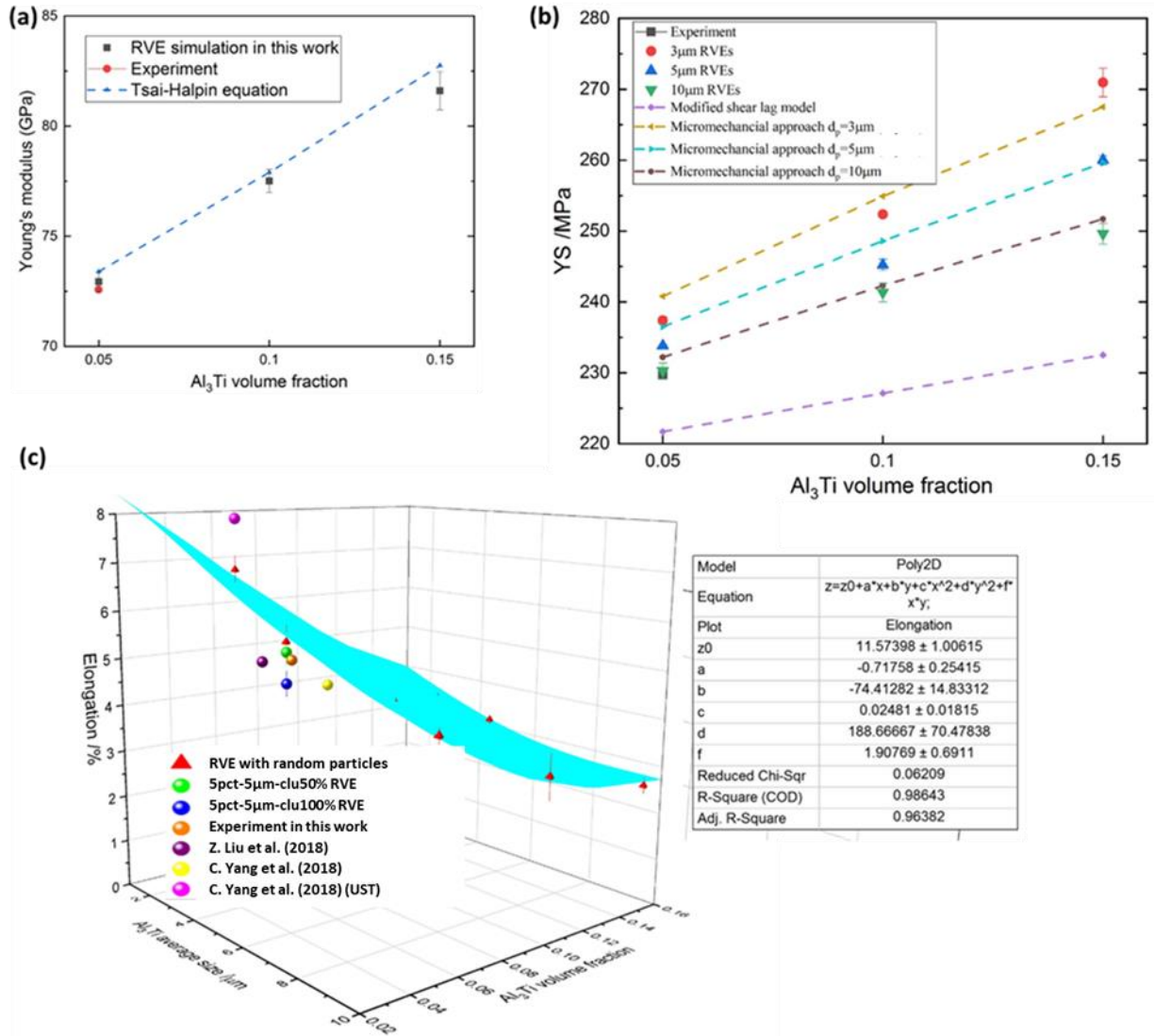


Figure 6.13. (a) Predicted Young's Modulus of Al₃Ti/A356 composites from simulation and comparison with the results calculated by Tsai-Halpin equation; (b) Predicted yield strength (YS) from simulation and comparison with the results calculated by modified shear lag model and micromechanical approach; (c) Predicted elongation of Al₃Ti/A356 composites from simulation and comparison with experimental results of related works. (The surface in the image refers to a polynomial 2D fitting surface from the simulation results of RVEs with random particle distribution in this work, UST = ultrasonic treatment)

Furthermore, the predicted elongation of the Al₃Ti/A356 composites with various structures from simulation are shown given Fig. 6.13(c). It is clear that the elongation of the composites decreases evidently with the increase of particle size and volume fraction. Here, a polynomial 2D surface fitting is applied on the points referring to the results from RVEs with

random particle distribution to predict the relationship between elongation and the characteristics of particles (particle size and fractions). The fitting surface is shown in Fig. 6.13(c). It is also seen that for the RVEs with clustering particles, the elongation locates beneath the fitting plane, which proves particle agglomeration is detrimental to the elongation of the composites.

In addition, experimental results of others (Z. Liu et al., 2018; C. Yang et al., 2018) on in-situ fabricated $\text{Al}_3\text{Ti}/\text{A356}$ composites, limited though, are also shown in Fig. 6.13(c) for comparison. It is seen that the results are located close to the fitting surface in general, suggesting that the predicted relationship from simulation are generally in accord with the reported experimental results with an acceptable discrepancy. The discrepancy could be attributed to the differences in Al_3Ti particle distribution and variations in the properties of the A356 matrix.

Other research on $\text{Al}_3\text{Ti}/\text{Al}$ matrix composites also suggest that the refinement of Al_3Ti particles and improved uniformity in distribution, achieved by friction stir processing (FSP), high speed shearing or ultrasonic treatment (R. Gupta et al., 2018; Hsu et al., 2006; R. Yang et al., 2015; Zeng et al., 2018; Q. Zhang et al., 2011), are helpful for improving the strength and elongation of the composites. Meanwhile it should be noted that the matrix grain size of the composites is also significantly refined in the processing, which furtherly improves the mechanical properties of the composites.

6.7 Summary

In this chapter, the mechanical properties of in-situ Al_3Ti particle reinforced A356 composites was studied by a 3D micromechanical finite element simulation method in this work. A series of RVEs were automatically generated to model the composites with various microstructural features, such as Al_3Ti particles of different sizes, volume fractions and distributions. The ductile damage of A356 matrix and brittle damage of Al_3Ti particles were considered, while the particle-matrix interface behavior was assumed as perfect bonding due to a strong interfacial bonding between Al_3Ti and Al matrix. The post failure behavior of both constitutive phases were described by a linear damage evolution law. The simulated uniaxial tensile stress-strain curve is in good agreement with the experimental work. Furthermore, the mechanical properties of the $\text{Al}_3\text{Ti}/\text{A356}$ composites with different microstructures, such as Young's modulus, yield strength and elongation, were predicted based on simulation. The following conclusions can be drawn:

With the decrease of particle size, the yield stress and elongation of the composites are improved. Microscopically, smaller particle size can bear more S_{11} at yield point and resulting in a higher yield strength. In addition, the damage evolution in A356 matrix in the RVEs with smaller Al_3Ti particles is slower and more uniform compared to those containing larger Al_3Ti particles. The elongation is improved therefore.

The increase of particle fraction in the composites can improve the yield strength while reducing the elongation evidently. Microscopic simulation suggests that a larger fraction of particles results in a reduced distance between neighbor particles and causes severe stress concentration. Therefore, the damage of particles and matrix are both promoted so that the elongation is decreased.

Particle clustering shows no evident effect on yield strength and flow stress at small strain. However, the elongation is reduced with the increase of the fractions of clustering particles. Microscopically, particle clustering facilitates the damage of particles and matrix locally.

The Young's modulus that is predicted by the RVEs in this work show a good agreement with the calculation of Tsai-Halpin equation. The predicted yield strengths are close to the micromechanics approach considering the load bearing and CTE mismatch strengthening effects. The influence of particle size on yield strength can be revealed by simulation. The relationship between elongation and the Al_3Ti particle properties are predicted from simulation results by a polynomial fitting. Despite the study is limited to $Al_3Ti/A356$ composites, the predict relationship is generally in agreement with reported experimental results.

CHAPTER 7. EFFECT OF HOT ROLLING AND HEAT TREATMENT ON MICROSTRUCTURE AND MECHANICAL PROPERTIES OF AN IN-SITU TiB₂/AL-CU-MG-SC COMPOSITE

7.1 Introduction

Aluminum alloy 2618 (Al2618) is selected as the matrix material for the investigation. Al2618 is a heat-treatable Al–Cu–Mg alloy with certain amounts of Fe and Ni alloying elements. It exhibits outstanding strength at both ambient and elevated temperatures, and is therefore widely utilized as structural components in the automotive and aerospace industries, such as cylinder heads, pistons for engines, airframe structures (Bergsma et al., 1996; Elgallad et al., 2014; N. M. Kumar et al., 2016; Nový et al., 2009; Özbek, 2007; J. H. Wang & Yi, 2006). The alloying elements, such as Fe and Ni can control grain size, provide dispersion hardening and enhance microstructural stability. Heat treatment can further increase the strength via precipitation hardening. Furthermore, adding trace alloying elements such as scandium (Sc) or Sc with Zr shows strengthening effect for an aluminum alloy by forming nano-sized coherent Al₃Sc or Al₃(Sc,Zr) in the aluminum matrix. The strengthening effect at both ambient and elevated temperatures were reported in Al (Fuller et al., 2003), Al-Fe-Ni (Bian et al., 2020) and Al2618 matrix (K. Yu et al., 2004). Previous findings indicated that Sc can improve the yield strength of TiB₂/2618 composites (S. Ma et al., 2020). Nevertheless, for monolithic aluminum alloys, their low stiffness, strength and wear resistance cannot fulfill some modern engineering applications. As a result, the fabrication of PRAMCs is considered an effective solution, for which in-situ TiB₂ is a promising reinforcing particle. The introduction of ceramic particulates such as TiB₂, is commonly applied to enhance the stiffness and strength of various Al alloy matrices, such as Al-Cu (S. C. Tjong & Lau, 1999), Al-Si (M. Wang et al., 2014), Al-Cu-Mg (Tang et al., 2019), Al-Mg-Si (S. M. Ma et al., 2014) and etc.

Additionally, PRAMCs have the advantageous that their ingots can be mechanically processed as same as monolithic alloys, such as extrusion, forging and rolling. The effects of secondary mechanical processing, such as rolling, on the mechanical properties of PRAMCs were investigated by related research work. For instance, R. V. Kumar et al. (2018) studied the effect of hot rolling microstructure and mechanical behavior of ZrB₂/Al6061 composites. Evident grain refinement and strength enhancement are shown compared to the matrix. The ductility of hot rolled composites is also increased compared to their as-cast counterparts. G. Li et al. (2021) investigated

the microstructures of A356 matrix composites with nanosized in-situ Al_2O_3 particles. The results show the fragment of Si phase and the disappearance of Al_2O_3 particle agglomeration with a 75 % rolling reduction. Lee & Subramanian (1992) studied a cold rolled $(\text{Al}_2\text{O}_3)_p/\text{Al}$ composites and also suggested the disappearance of banded Al_2O_3 clusters after rolling. Amirkhanlou & Niroumand (2011) fabricated a high-strength Al6061/10 vol.% SiC_p composite by compocasting and cold rolling. The rolled composites exhibited a reduced porosity and a highly-uniform particle distribution. A recent work by Tang et al. (2019) reported an in-situ nano $\text{TiB}_2/\text{Al-Cu-Mg}$ composites by cold rolling and post-aging treatment, which possesses high strength and ductility. They found that TiB_2 particles play an effective role in dislocation pinning and accumulation during the cold-rolling process. Generally, it is indicated that rolling deformation is helpful in reducing the porosity and achieve a more uniform particle distribution in cast composites by breaking up particle agglomerates. Matrix grain refinement and particle-matrix interfacial bonding enhancement can be also achieved, resulting in the improvement of mechanical properties (Tao et al., 2018; D. Wang et al., 2020). However, there are still limited research studying the effect of mechanical processing and heat treatment on the microstructure and properties of Al2618 alloy matrix composites.

In this chapter, aiming to achieve improved mechanical performance of Al2618 alloy matrix, in-situ TiB_2 particulates are introduced via salt-metal reaction into Al2618 alloy matrix with a minor amount of Sc addition. A series of $\text{TiB}_2/\text{Al2618}$ composites are fabricated and subjected to hot rolling, with different particle volume fraction, rolling deformation and heat treatment. The role of each factor on the microstructure and mechanical properties are discussed in detail. The strengthening mechanisms and fracture behaviors are also included.

7.2 Experiment

The in-situ TiB_2 particulate reinforced Al2618 alloy was produced via chemical reactions of a mixture of KBF_4 and K_2TiF_6 salts with the alloy melt in an induction furnace at 730 °C for 30 min. The particle weight percentage (wt. %) was set as 0 % (with no salt addition), 4 % or 8 % (noted as Al2618, C4, and C8), respectively. The melt was stirred by an electromagnetic field and the slag was removed before casting into 1lb piglets. The alloy and composite ingots were remelted at 780 °C in an electrical resistance furnace and poured at 730 °C into a preheated steel mold (400 °C) with a cavity dimension of 260 mm × 33 mm × 6.7 mm. A laboratory rolling mill was

used for hot rolling process. The cast coupons were annealed at 480 °C for 1 h and subsequently rolled into 4.2 ± 0.1 mm and 2.0 ± 0.1 mm, equivalent to 35 % and 70 % thickness reduction (noted as R35 and R70) through multiple passes. The thickness reduction of each pass is approximately 0.5 mm. The sheets were annealed at 480 °C for 10 min between passes. The chemical compositions of the Al2618 alloy and TiB₂/Al2618 composites are given in Table 7.1. Some of the hot rolled sheets were subjected to a heat treatment as follows: solid solution at 530 °C for 5 h, water quenching, and then artificial aging at 195 °C for 20 h.

The as-rolled and heat-treated sheets were cut into dog-bone shaped tensile samples according to the ASTM-B557M standard. The gauge length is 25.4 mm and the width is 6 mm. Uniaxial tensile tests were conducted on an ATS900 machine at room temperature at a strain rate of 10^{-3} s^{-1} along the rolling direction of the samples. X-ray diffraction was conducted on polished samples with a Bruker-D8 Focus Machine. The microstructures of composites were characterized by using a Leica DM-LM/P optical microscope (OM). The samples were polished and etched for about 30 s by using the Keller's reagent (2.5 ml HNO₃, 1.5 ml HCl, 1.0 ml HF and 95 ml H₂O) and washed by purified water. A Quanta 3D field emission scanning electron microscope (FESEM) equipped with an energy dispersive X-Ray spectrometer (EDS) was used for SEM and EDS analysis under 10 kV accelerating voltage. Microstructural image analysis was carried out with Image J software to measure the TiB₂ particle size.

Table 7.1. Chemical composition of the studied materials (in wt. %)

Materials	Cu	Mg	Ni	Si	Fe	Sc	Ti	B	Al
Al2618	2.4	1.6	1.2	0.16	0.09	0.11	--	--	bal.
TiB₂/Al2618(4 wt. %)	2.4	1.6	1.2	0.17	0.11	0.11	2.7	1.2	bal.
TiB₂/Al2618(8 wt. %)	2.4	1.7	1.2	0.34	0.13	0.11	5.4	2.4	bal.

7.3 Microstructure

7.3.1 Microstructure of in-situ TiB₂/Al2618 composites

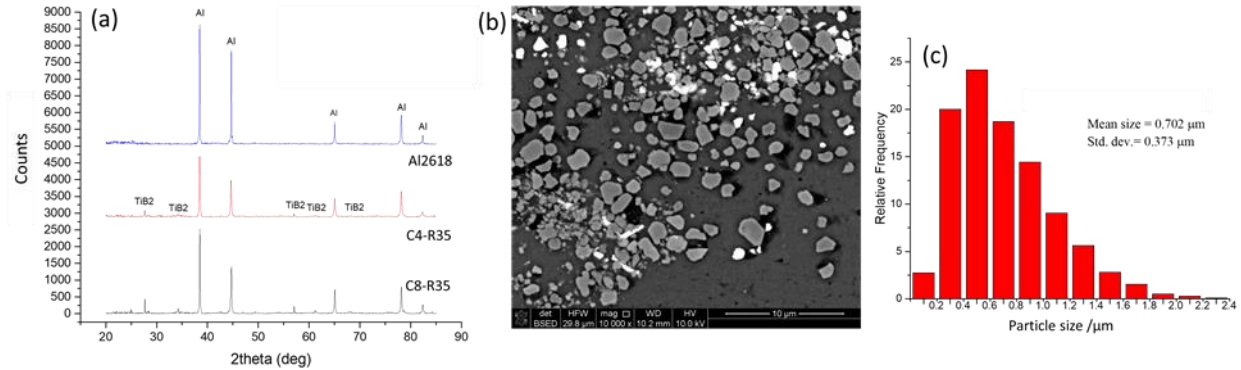


Figure 7.1. (a) XRD spectra of Al2618 alloy and in-situ TiB₂/Al2618 composites (R35 samples, heat-treated); (b) Backscattered electron image (BSE) shows typical morphology of TiB₂ particulates; (c) The size distribution of the in-situ TiB₂ particulates (C8-R35 sample).

The XRD spectra of Al2618 alloy and the in-situ TiB₂/Al2618 composite are presented in Fig. 7.1(a), the peaks of Al (JCPDS:89–4037) and TiB₂ (JCPDS:35–0741) can be indexed in both C4 and C8 composites. Other phases, such as intermetallics and precipitation phases can be hardly identified from the pattern due to the measurement limit of the machine.

Typical morphology of the TiB₂ particulates are shown in Fig. 7.1(b). The particles are mostly blocky and equiaxial shaped. Particle cracking is scarcely observed after rolling. From the size distribution histogram in Fig. 7.1(c), plenty of TiB₂ particles are submicron in size, although the maximum size can exceed 2 μm. The size of TiB₂ particles follows a typical lognormal distribution with an average size of approximately 0.7 μm.

Figure 7.2 shows the typical microstructures of the as-rolled Al2618 alloy and TiB₂/Al2618 composites. It is seen that the Al2618-R35 alloy has a typical dendritic grain structure. However, in the C4-R35 or C8-R35 composites, the grains are mostly equiaxed. The dendritic grain structure is also rarely observed in all the R70 samples. Compared to the R35 samples, the microstructures of the R70 samples show the presence of both irregular, elongated grains and equiaxed grains. The elongated grains are resulted from the deformation the hot rolling, while the equiaxed grains may be a result of dynamic recrystallization (DRX). In addition, the grains are evidently refined with

the increase amount of TiB_2 particles, since TiB_2 particles facilitated a heterogeneous nucleation and reducing the grain size. Additionally, TiB_2 also promoted dynamic recrystallization by the particulate simulate nucleation (PSN), resulting in small-sized recrystallized equiaxed grains.

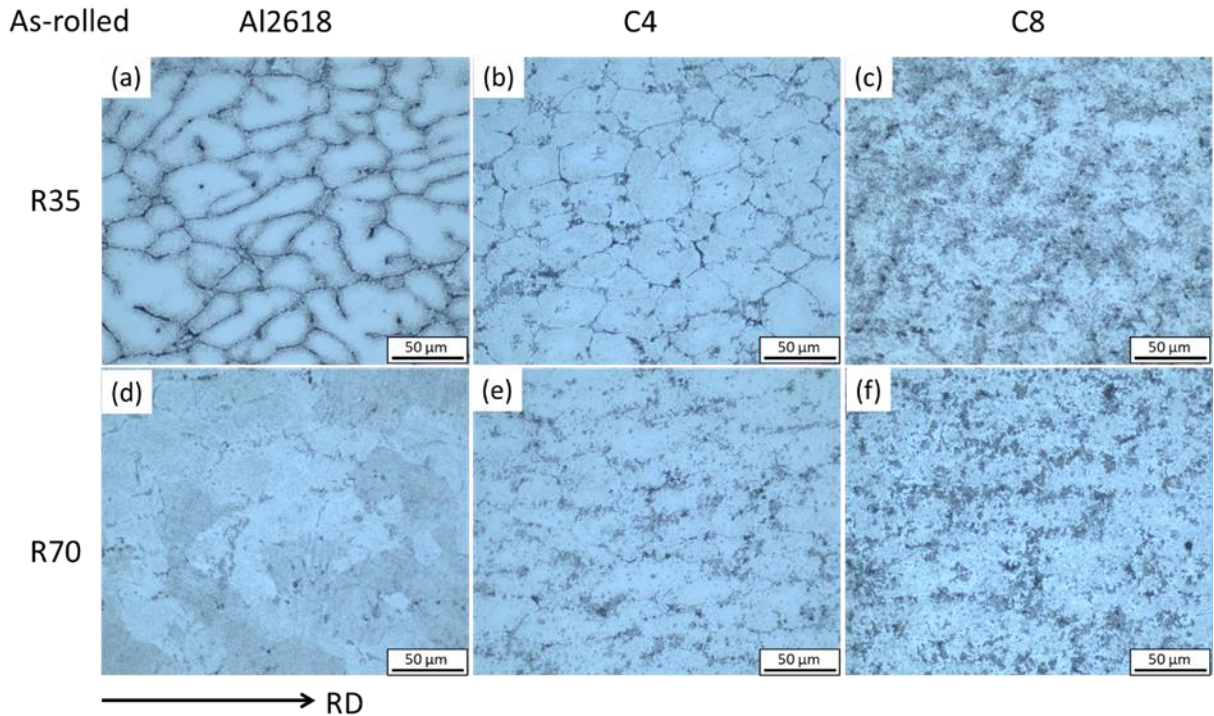


Figure 7.2. OM images of the as-rolled Al2618 alloy and $\text{TiB}_2/\text{Al2618}$ composites taken from RD-TD plane (a) Al2618-R35, (b) C4-R35, (c) C8-R35; (d) Al2618-R70; (e) C4-R70; and (f) C8-R70.

Typical BSE images of the as-rolled Al2618 alloy and $\text{TiB}_2/\text{Al2618}$ composites are presented as Fig. 7.3, showing the distribution of intergranular intermetallics (bright white contrast zones) and TiB_2 (grayish particles). For the Al2618-R35 sample in Fig. 7.3(a), coarse intermetallics are typically seen at the grain boundaries. While in the R35 composites, they become finer in size due to the intergranular TiB_2 particulates restricting growth of intermetallics, as shown in Figs. 7.3(b) and (c). Moreover, with the increase of rolling deformation, the coarse intermetallics are fragmented and refined as in the R70 samples in Figs. 7.3(d)~(f), compared to the R35 samples. TiB_2 particles are partly agglomerated. They are either mixed with the intermetallics fragments at grain boundaries or distributed within the Al grains

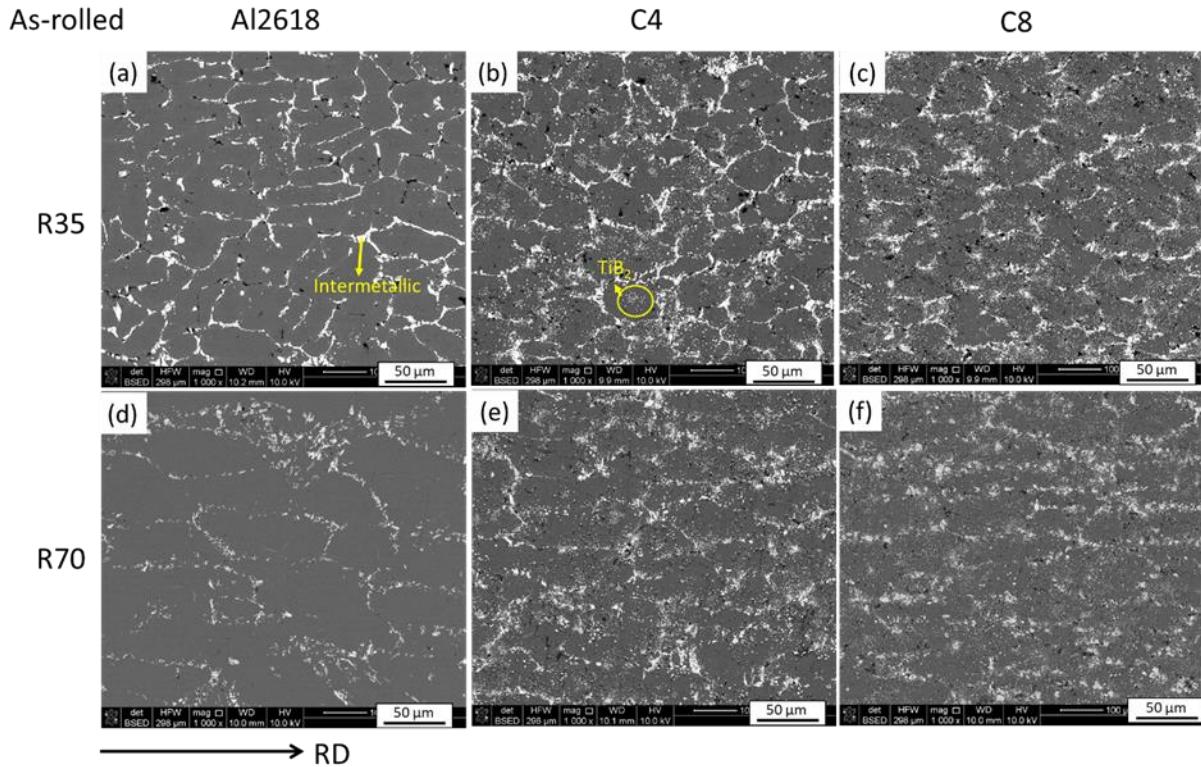


Figure 7.3. BSE images of the as-rolled Al2618 alloy and $\text{TiB}_2/\text{Al2618}$ composites taken from RD-TD plane (a) Al2618-R35, (b) C4-R35, (c) C8-R35; (d) Al2618-R70; (e) C4-R70; and (f) C8-R70.

Fig. 7.4 presents the microstructures of the heat-treated Al2618 alloy and $\text{TiB}_2/\text{Al2618}$ composites. It is observed that the intermetallics are spheroidized after heat treatment. For the Al2618-R35 sample, dendritic grain structure remains after heat treatment. In the C4-R35 and C8-R35 composites, equiaxed recrystallized grains can be rarely seen, recrystallization may occur but to a quite limited degree. In comparison, with a larger amount of deformation, equiaxed grains are dominating the microstructure in the R70 alloy and composites, indicating a fully recrystallization after heat treatment. Moreover, with the introduction of TiB_2 , the recrystallized grain size is obviously refined, compared to the unreinforced alloy.

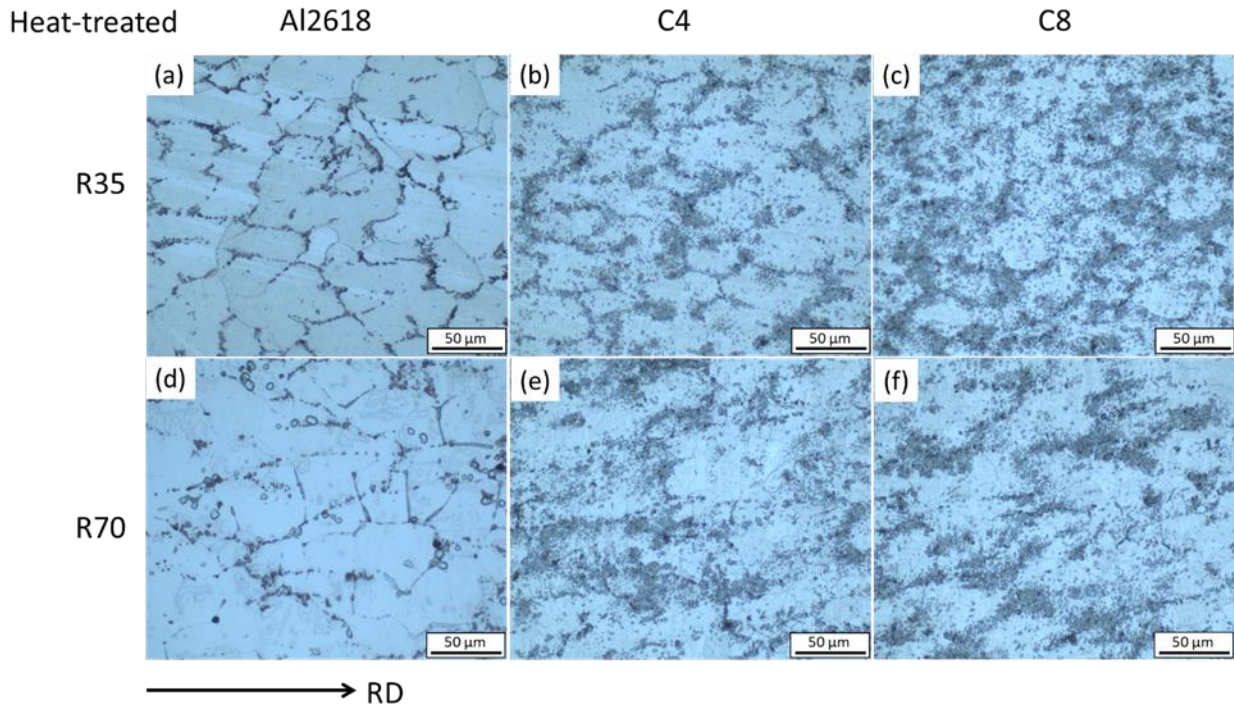


Figure 7.4. OM images of the heat-treated Al2618 alloy and $\text{TiB}_2/\text{Al2618}$ composites (a) Al2618-R35, (b) C4-R35, (c) C8-R35; (d) Al2618-R70; (e) C4-R70; and (f) C8-R70.

7.3.2 EDS analysis

Element distribution in a typical microstructure of the as-rolled C8-R70 $\text{TiB}_2/\text{Al2618}$ composite is analyzed by EDS. From Fig. 7.5(a), the intermetallic phases are fractured after rolling and mixed with TiB_2 particulates. EDS point analysis at several locations in Fig. 7.5(a) are conducted and the results are shown in Fig. 7.5(b). Points 1~3 show the typical composition of intermetallic phases. It is indicated that the intermetallic phases are rich in Cu and Ni from the composition of Point 1 and the element mapping of Cu and Ni in Fig. 7.5(c), indicating Al-Cu-Ni intermetallic phases. Element Fe can be found in some intermetallic phases associated with Cu and Ni from Point 3, suggesting Al-Cu-Fe-Ni type intermetallics. The association of element Mg and Si is found to some extent, suggesting a Mg_2Si phase. Furthermore, local enrichment of Sc is found in some of the Al-Cu-Ni intermetallics from the composition of Point 2. The local enrichment of Sc can be detected in Sc mapping of Fig. 7.5(c), though not so clear due to the low Sc amount in the composite. The point analysis of the matrix (Point 4) shows that Mg and Cu are mainly dissolved in Al matrix as alloying elements.

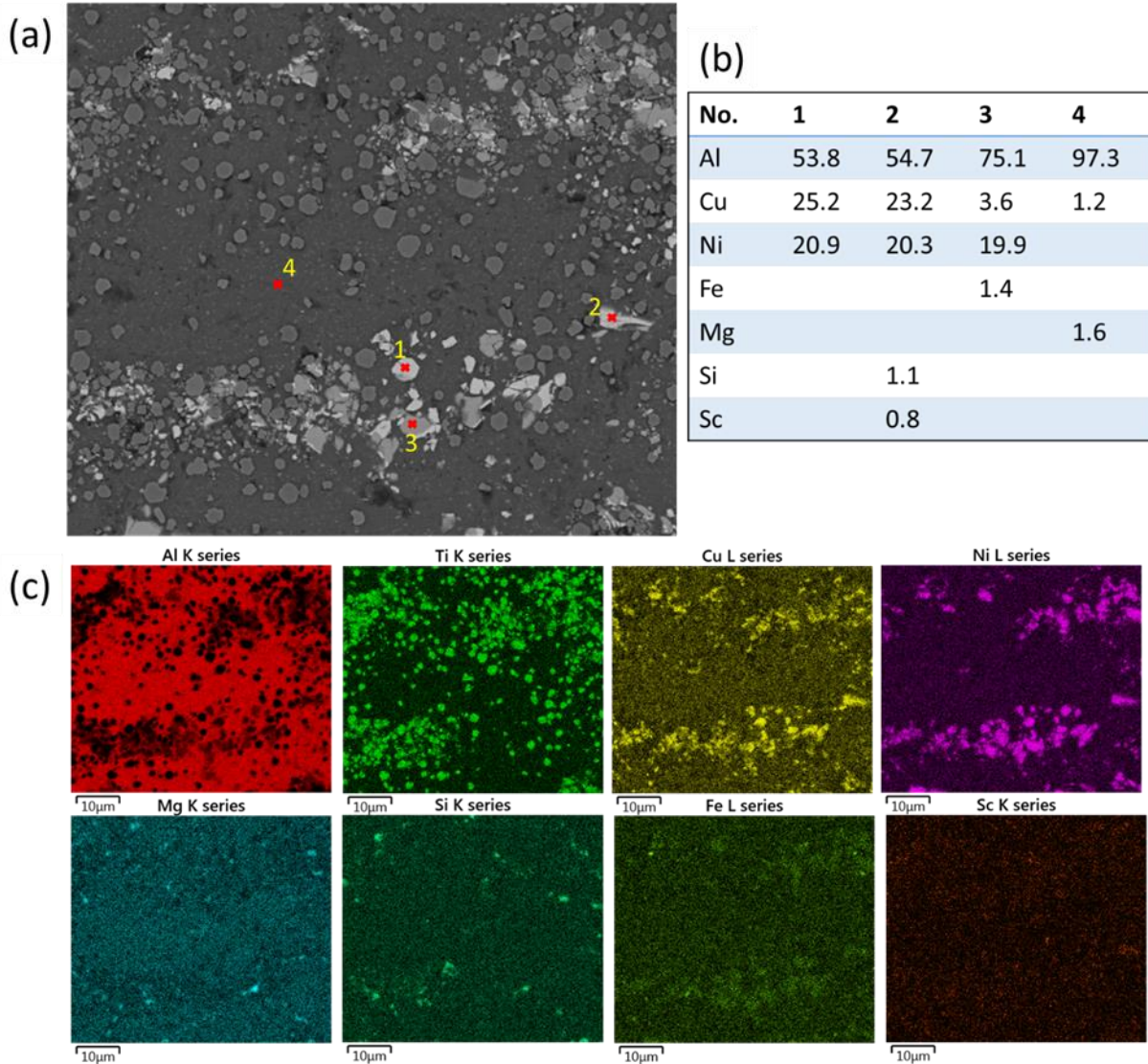


Figure 7.5. EDS analysis of as-rolled $\text{TiB}_2/\text{Al2618}$ composite (C8-R70 sample) (a) Electron image; (b) Elemental composition from the point analysis in figure (a) (in at. %); (c) Elemental mapping.

Fig. 7.6 gives the EDS analysis results of a typical microstructure of the heat-treated C8-R70 $\text{TiB}_2/\text{Al2618}$ composite. From the microstructure in Fig. 7.6(a), it is clear that the bright intermetallic phases are spheroidized and refined after rolling and heat treatment to the size close to that of TiB_2 particulates. The element mappings in Fig. 7.5(c) also indicate the enrichment of Cu and Ni in the intermetallics, with small amount of Fe. The association of Mg and Si is also revealed by the Mg and Si elemental mappings in Fig. 7.6(c). Cu and Mg are also mainly detected

in the Al matrix, as the case of the as-rolled state. In addition, local enrichment of Sc is also evident in a portion of Al-Cu-Ni type intermetallic particulates from the composition of Points 2 and 3 in Fig. 7.6(b). It is also indicated that the Sc enriched intermetallic particles are also enriched with a certain amount of Si from the Point 2 in Fig. 7.5(b) and Points 2 and 3 in Fig. 7.6(b).

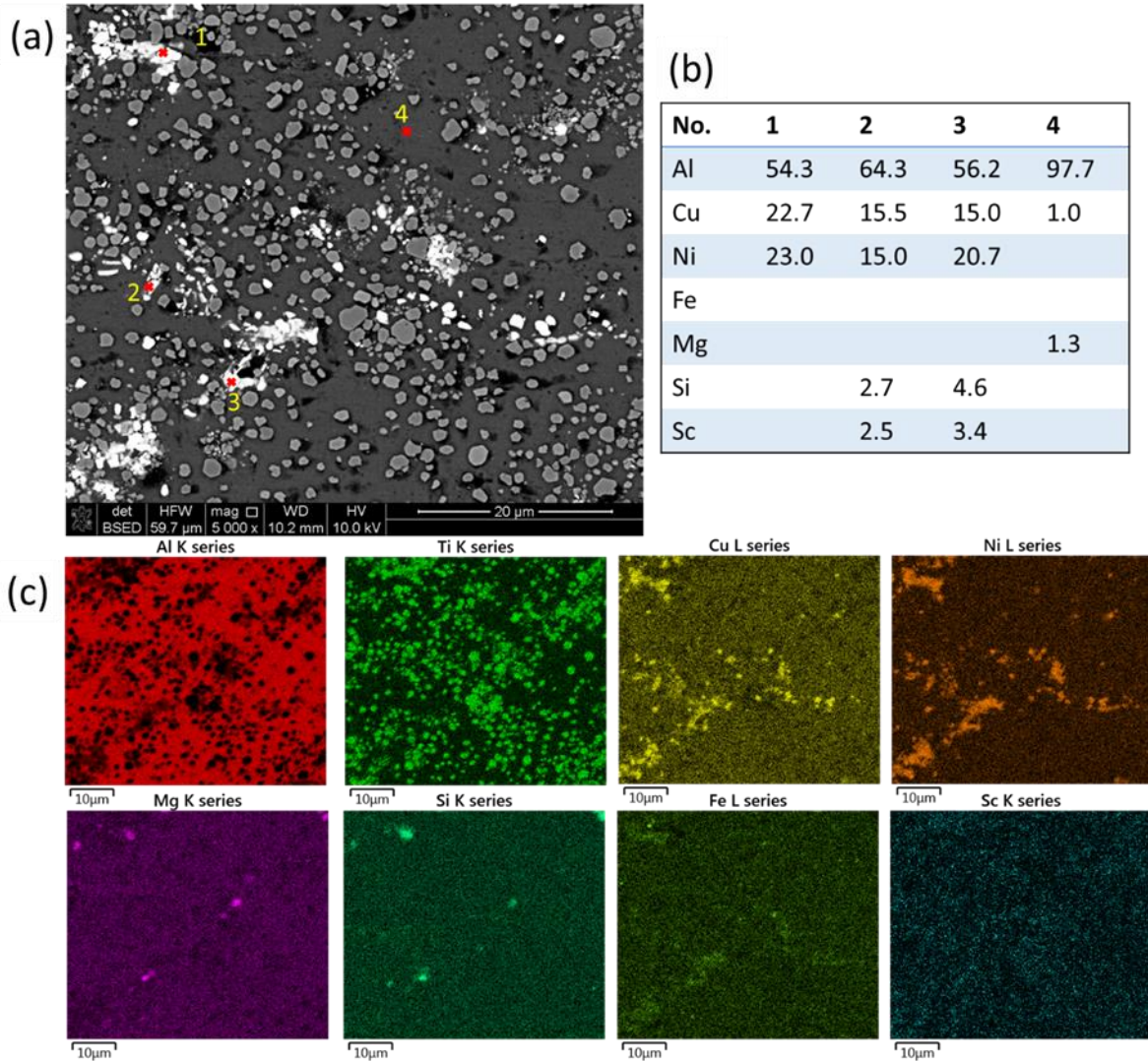


Figure 7.6. EDS analysis of heat-treated TiB_2/Al_{2618} composite (C8-R60 sample) (a) Electron image; (b) Elemental composition from the point analysis in figure (a) (in at. %); (c) Elemental mapping.

7.4 Mechanical Properties

7.4.1 Tensile properties

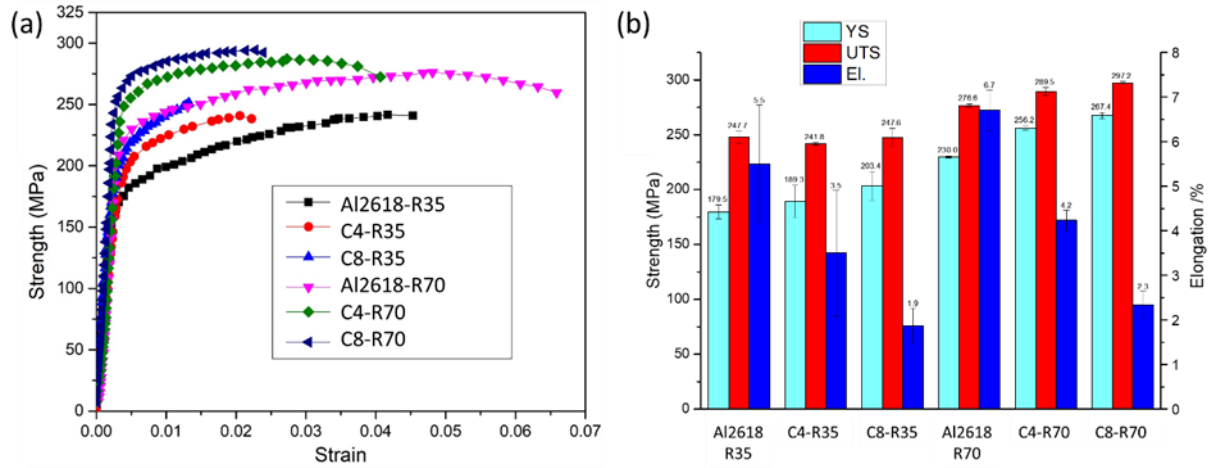


Figure 7.7. Uniaxial tensile properties of the as-rolled Al2618 and TiB₂/Al2618 composites; (a) Tensile stress-strain curves; (b) Statistical histogram.

Uniaxial tensile properties of the as-rolled Al2618 and TiB₂/Al2618 composites are shown in Fig. 7.7. For the same rolling reduction, YS is improved with the increase of TiB₂ content. However, the El. is decreased accordingly, from the stress-strain curves in Fig. 7.7(a). The YS, UTS and El. of the R70 alloy and composites are simultaneously increased, compared with their R35 counterparts. It is indicated that the increase of rolling deformation improves the YS by work hardening. The improvement of elongation can be attributed to the reduction of porosity and refinement of intermetallic phases. As a result, it shows that the Al2618 and TiB₂/Al2618 composites achieve evidently better mechanical properties after a 70 % thickness reduction by hot rolling. The statistics of Fig. 7.7(b) reveals that the as-rolled C8-R70 composite can reach a high YS of over 250 MPa and UTS of nearly 300 MPa, which is 16.3 % and 7.4 % higher than the Al2618-R70 alloy, and 43.4 % and 20.0 % higher than the Al2618-R35 alloy, due to the introduction of TiB₂ and the increase of hot rolling deformation.

Fig. 7.8 presents the uniaxial tensile properties of the heat-treated Al2618 and TiB₂/Al2618 composites. For the R35 samples, the YS still increases with the increased amount of TiB₂ but with the expense of elongation as Fig. 7.8(a). Compared to the as-rolled R35 samples, evident

improvement of YS and UTS is shown in the heat-treated R35 samples owing to precipitation hardening, but the elongation is reduced meanwhile. For the heat-treated R70 samples, the YS is not evidently increased (C8-R70) or even slightly decreased (C4-R70) with the increase of TiB_2 , compared to that of the Al2618 alloy. It is indicated that the YS in the heat-treated R70 composite samples undergoes softening during heat treatment, contradicting to the strengthening effect by TiB_2 . In addition, after heat treatment, the YS of the R70 samples is also increased very little (Al2618-R70), or reduced (C4-R70 and C8-R70) compared to the heat-treated R35 samples as compared in Fig. 7.8(b). Therefore, it is also suggested softening can occur in the R70 samples after heat treatment, contradicting to work hardening by rolling deformation. Meanwhile, the elongation of all the R70 samples after heat treatment are greatly increased compared to the as-rolled samples and the heat-treated R35 samples, from the statistics in Figs. 7.7(b) and 7.8(b). The improved elongation also suggests a softening effect after heat treatment. The softening will be demonstrated in detail later.

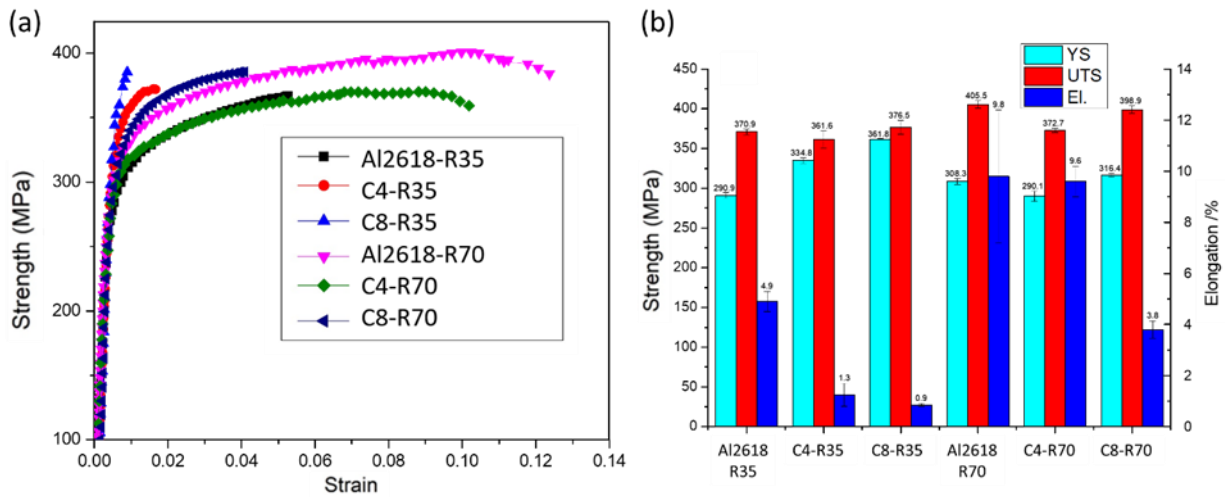


Figure 7.8. Uniaxial tensile properties of the heat-treated Al2618 and $TiB_2/Al2618$ composites; (a) Tensile stress-strain curves; (b) Statistical histogram.

7.4.2 Fracture surface

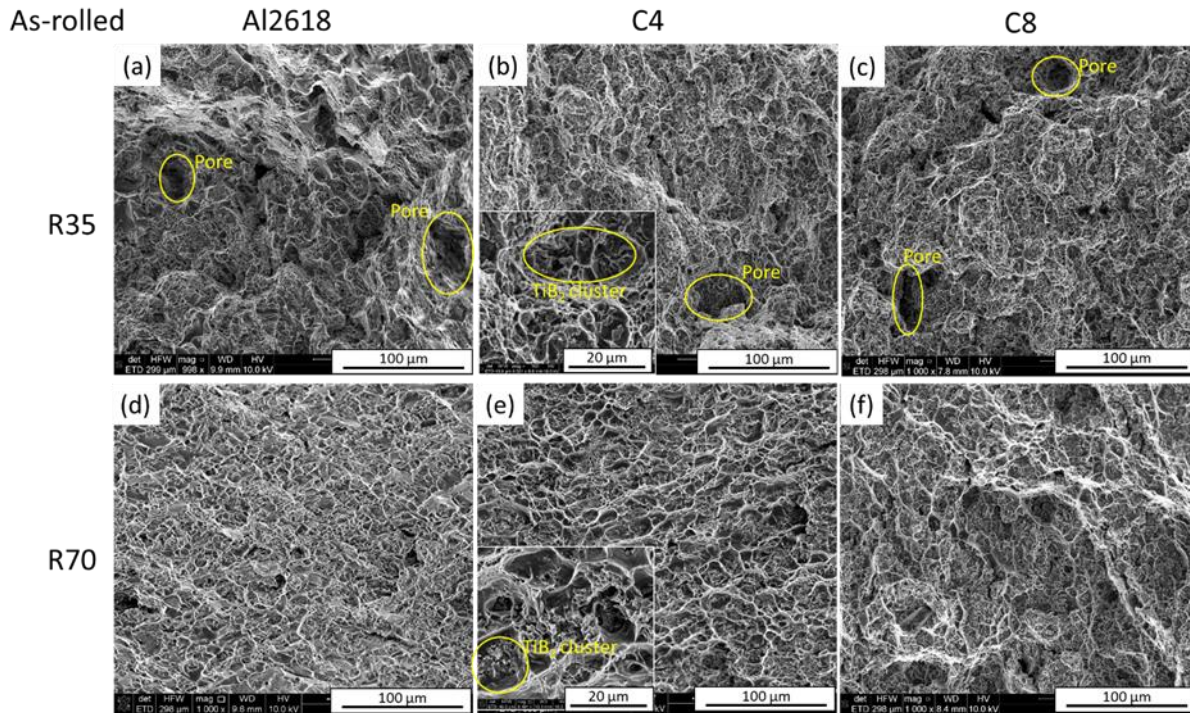


Figure 7.9. Typical fracture surfaces of the as-rolled Al2618 alloy and $\text{TiB}_2/\text{Al2618}$ composites; (a) Al2618-R35, (b) C4-R35, (c) C8-R35; (d) Al2618-R70; (e) C4-R70; and (f) C8-R70.

Fig. 7.9 presents the typical fracture surfaces of as rolled Al2618 alloy and $\text{TiB}_2/\text{Al2618}$ composites. In general, dimples appear in all the samples indicating typical ductile fracture feature. In the R35 samples, several large-sized voids are observed, referring to the porosity inside the materials, as circled in Figs. 7.9(a)~(c). Comparatively, in the R70 samples, such large pores are rarely found, suggesting that the increase of rolling deformation effectively reduces the porosity in the Al2618 alloy and $\text{TiB}_2/\text{Al2618}$ composites. As a result, a higher elongation is achieved. Additionally, in the composite samples, TiB_2 clusters appear on the fracture surface, resulting in localized large size dimples around the particles, as shown in Figs. 7.9(b), (c), (e) and (f). The TiB_2 clusters act as damage nucleation zones facilitating the damage evolution. Consequently, the ductility is adversely affected and the elongation of $\text{TiB}_2/\text{Al2618}$ composites is lower than Al2618 alloy.

The fractography of heat-treated Al2618 alloy and $\text{TiB}_2/\text{Al2618}$ composites are shown in Fig. 7.10. Similar to the as-rolled state, the pores in the R35 samples in Figs. 7.10(a)~(c) are eliminated in the R70 samples with further rolling deformation. The TiB_2 particle clusters are also

observed in the composites. Moreover, the fracture surfaces of the heat-treated R70 samples are dominated by fine-sized and uniform dimples as Figs. 7.10(d)~(f), compared to all other samples in Figs. 7.9 and 7.10. The small and uniform dimples suggest a good ductility, which agrees with the tensile test results in Fig. 7.8(b). That is attributed to the refinement of intermetallic phases after a larger hot rolling deformation (R70) and heat treatment.

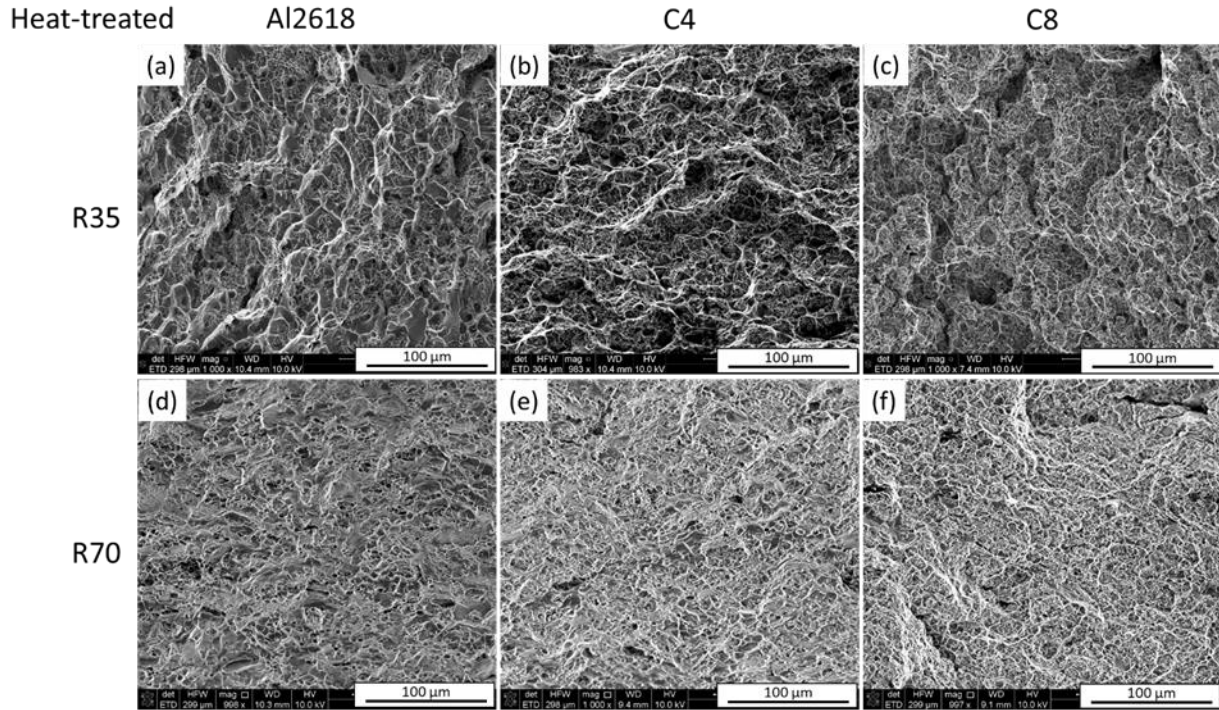


Figure 7.10. Typical fracture surfaces of the heat-treated Al2618 alloy and $\text{TiB}_2/\text{Al2618}$ composites; (a) Al2618-R35, (b) C4-R35, (c) C8-R35; (d) Al2618-R70; (e) C4-R70; and (f) C8-R70.

7.5 Discussions

From the results above, hot rolling and heat treatment have shown obvious influence on the microstructure of Al2618 and $\text{TiB}_2/\text{Al2618}$ composites, such as grain structure, morphology of intermetallic phases, particulate distribution as well as precipitation, resulting in the differences in the mechanical properties among the samples. Additionally, TiB_2 particulates cannot only contribute to the strength increase as reinforcements, but also potentially affect the thermomechanical deformation and precipitation progress microscopically, according to related works (Z. Chen et al., 2017; Dan et al., 2017; G. Li et al., 2021; Tan et al., 2001). As a consequence,

the effect of hot rolling, heat treatment as well as TiB_2 particulates can be interactive on the microstructure and the mechanical properties, which will be discussed as follows.

7.5.1 Effect of hot rolling

Hot rolling deformation generates a high shear and compressive stress, causing the elongation of grain structure along the rolling direction and the reduction of casting porosity. Meanwhile, the fragment of large-sized brittle intermetallic phases and reinforcement particulates can be typically achieved, due to the discrepancy between the Al matrix in deformation. For small sized reinforcements, fragment is rarely observed. Instead, the shear metal flow tends to cause of the redistribution of particulates aligned in the rolling direction. The agglomerations of smaller particles can be released therefore, as reported in related works (R. V. Kumar et al., 2018; Tao et al., 2018; D. Wang et al., 2020). In this work, compared to the R35 samples, the R70 samples show more elongated grains under a severer rolling reformation. Additionally, the intermetallic particles are fragmented and TiB_2 particulates are redistributed along the roll direction. The porosity is also reduced from the fracture surfaces, compared as Fig. 7.9 and Fig. 7.10. Consequently, the strength and elongation of R70 Al2618 alloy and $\text{TiB}_2/\text{Al2618}$ composites are improved simultaneously, compared to their R35 counterparts. The enhanced mechanical properties are attributed to work hardening effect, reduced porosity, the refined intermetallic particles and more uniform distribution of TiB_2 particulates by a larger rolling deformation.

Moreover, it is also reported that restoration occurs together with work hardening during hot rolling, in the forms of dynamic recovery (DRV) and/or dynamic recrystallization (DRX). It is generally believed that DRV takes place in aluminum alloy while DRX is suppressed due to its high stacking fault energy (SFE), and also reported in the unreinforced Al alloys from similar work (Z. Chen et al., 2017; Humphreys, 2004). Typically, the recrystallized grains occur at grain boundaries or triple junction with refined size and an equiaxial morphology. In this work, it is shown that recrystallized grains are rarely seen in all the R35 samples from Figs. 7.2(a)~(c). It is suggested that DRX rarely happens since the R35 deformation cannot produce enough stored energy to initiate recrystallization. With the increase of deformation (R70), elongated grains along the rolling direction and small-sized equiaxial grains appear in the R70 samples, as shown in Figs. 7.2(d)~(f), evidencing the deformed grains and recrystallized grains. So, it is concluded that partially DRX occurs in the R70 Al2618 alloy and $\text{TiB}_2/\text{Al2618}$ composites, but still to a limited

extent. Generally, restoration in the form of recovery has little effect in decreasing the strength while recrystallization decreases the strength significantly. Due to the limitation of DRX, the softening by restoration is also limited. As a result, when the rolling deformation increases to R70, the working hardening still dominates compared to the softening by restoration. Consequently, the YS and UTS of R70 samples are superior to those of R35 samples, as shown in Fig. 7.6(b). It is also observed that a dendritic to equiaxial grain conversion occurs in Al2618 alloy when the rolling reduction increased from R35 to R70, indicating the occurrence of DRX during hot rolling.

7.5.2 Effect of heat treatment

The heat treatment in the current work consists of solid solutionization at 530 °C for 5 h, and artificial aging at 195 °C for 20 h, which are typically applied to Al2618 alloy (Casati et al., 2017; Shen et al., 2016; K. Yu et al., 2004). Solid solutionization results in the diffusion of alloying elements, and refines the size and morphology of intermetallic phases. Additionally, further restoration after hot rolling deformation is expected during solution treatment in the forms of static recovery or recrystallization, because the temperature is higher than the recrystallization temperature of 2xxx-series Al alloys. As current work for instance, 530 °C is above the recrystallization temperature range of Al2618 (600~700 K), from the work of K. Yu et al. (2004). However, in the R35 samples, the grain structure of the heat-treated samples does not show an obvious difference from their as rolled counterparts. It is indicated that recrystallization rarely happens in these samples after heat treatment. That is also attributed to the limited deformation that does not store enough energy to drive the recrystallization. In comparison, more recrystallized grains are observed in R70 samples with larger rolling deformation after heat treatment, as being compared in Figs. 7.2(d)~(f) to Figs. 7.4(d)~(f).

The artificial aging results in the precipitation hardening of Al2618 and TiB₂/Al2618 composites, following precipitation process in Al-Cu-Mg alloys. In addition, trace Sc element is also potentially to provide additional precipitation hardening by forming fine Al₃Sc in the matrix. From Figs. 7.5 and 7.6, local Sc enrichment can be found in some intermetallic particles both in the as-rolled and heat-treated samples. That is attributed to the formation of a W(Al-Cu-Sc) phase (Y. H. Gao et al., 2019). However, Sc in matrix can also be detected in the matrix though the content is a trace element. S. Ma et al. (2020) reported an additional YS enhancement by Sc addition in TiB₂ composites, compared to the matrix without Sc addition.

As to the mechanical properties, heat treatment causes the softening of materials by recrystallization and hardening by the precipitation of secondary phases. In all the R35 samples, the restoration, especially recrystallization is quite limited and softening is therefore not evident. As a consequence, precipitation hardening is prevailing. The YS is greatly increased, according to the comparison of the as-rolled and heat-treated samples in Fig. 7.7(b) and Fig. 7.8(b). However, in the R70 samples, the softening effect by recrystallization becomes more evident compared to precipitation hardening. Therefore, the increase of YS after heat treatment is quite limited compared to the as-roll state. But, meanwhile, the softening by recrystallization contributes to the significant increases in elongation in the heat-treated R70 samples from the histograms in Fig. 7.7(b) and Fig. 7.8(b).

7.5.3 Effect of TiB₂ particulates

Firstly, TiB₂ particulates refine the grains and modify the morphology of the grains of Al2618 alloy, as shown in the as-rolled R35 samples in Figs. 7.2(a)~(c). With the increase of the volume fraction of TiB₂ particulates, the dendritic grains turn to equiaxial. The grain size is also reduced obviously. TiB₂ particulates act as nuclei and enhance heterogeneous nucleation of the grains. In addition, the introduction of TiB₂ particulates enhances the recrystallization by particle stimulated nucleation (PSN) effect. The PSN is typically activated by particles larger than 1 μm diameter (Humphreys, 2004). It is also reported that clusters of particle may act as one very large particle, leading to strain and strain rate inhomogeneity, promoting recrystallization. The particles can enhance dislocation generation and reservation by pinning dislocations during the high temperature deformation process and provide driving force for dynamic recrystallization (Z. Chen et al., 2017; Humphreys et al., 1990). It is believed in the current work that the large TiB₂ particles (>1 μm) and TiB₂ particle clusters facilitate recrystallization by PSN effect and result in the formation of recrystallized grains especially in the R70 samples. Besides, TiB₂ particles also act as obstacles that slow down or restrict the growth of the deformed grains and recrystallized grains. With the increase of TiB₂ volume fraction, the grain size is reduced in the as-rolled R70 samples as Figs. 7.2(d)~(f), evidencing the restriction effect. In Figs. 7.4(d)~(f), it is also clearly seen that the size of recrystallized grains is reduced by TiB₂ addition after heat treatment.

With the increase of TiB₂ volume fraction, the YS is generally increased for the as-rolled samples TiB₂ particulates result in the strengthening of matrix via the following mechanisms: load-

bearing strengthening $\Delta\sigma_{\text{Load}}$, grain size refinement $\Delta\sigma_{\text{gf}}$, coefficient of thermal expansion (CTE) mismatch strengthening $\Delta\sigma_{\text{CTE}}$, as well as Orowan strengthening $\Delta\sigma_{\text{Oro}}$. Theoretically, the contribution of each strengthening mechanisms can be expressed as follows.

The load-bearing strengthening is the direct contribution of TiB_2 reinforcing particulates. Attributed to a strong interfacial bonding, an applied load is transferred from the soft matrix to the hard reinforcing particulates effectively. It is assumed that TiB_2 particles are equiaxial and its aspect ratio is 1, its contribution to the yield stress can be expressed as Eq. 2.6.

Grain refinement strengthening is generally evaluated by the well-known Hall-Patch strengthening (Eq. 2.9). The constant k is taken as $68 \text{ MPa}\cdot\mu\text{m}^{0.5}$ for Al (Z. Liu et al., 2018), d and d_0 are grain sizes of the composites and the Al2618 alloy, respectively.

CTE mismatch strengthening is resulted from the CTE difference between the TiB_2 particulates and the matrix. Residual plastic strain is produced when the composites are cooled down from processing temperature to an ambient temperature. Then dislocations are generated around the reinforcing particulates to accommodate the CTE difference. The contribution of this mechanism can be calculated generally by Eqs. 2.7 and 2.8.

The Orowan strengthening explains the strengthening effect from the interaction between reinforcement particulates and dislocations motion in the matrix. In general, to activate this mechanism, the particulate size should be less than $1 \mu\text{m}$ in diameter. Based on the size distribution in Fig. 7.2(b), most TiB_2 particulates are submicron-sized and effective in activating the Orowan strengthening. The Orowan-Ashby equation is, therefore, employed to calculated the strengthening effects as Eqs. 2.10 and 2.11.

Then the YS of the $\text{TiB}_2/\text{Al2618}$ composites can be expressed as Eq. 2.12, assuming adding all the contribution of each strengthening mechanism in a linear fashion.

The contribution of each strengthening mechanism to the YS is calculated with Eqs. 2.6~2.11 as listed in Chapter 2. It should be noted that the predicted YS can be larger than the experimental values, because only a portion of TiB_2 reinforces the matrix effectively due to the clustering of TiB_2 particulates along the grain boundaries. M. Wang et al. (2014) proposed an effective volume ratio ($\varepsilon < 1$) to evaluate the effect.

For the heat-treated samples, the YS is also increased with the increase of TiB_2 particles in the heat-treated R35 samples. However, that is not the case for in the heat-treated R70 samples. For the PRAMCs, with the addition of particles in composites, a large amount of metal

matrix/particle interfaces are created, which affect the dissolution-precipitation process of metal matrix during aging treatment. It is called the particulate-assisted precipitation behaviors. In general, reinforced particles accelerate the precipitating kinetics in matrix, because the addition of particles creates more dislocations in the metal matrix. The increase in dislocation density promotes dislocation-assisted diffusion of alloying elements, resulting in solute enrichment in the interfacial region, thus meeting the compositional requirement for precipitation. (Das et al., 1996; M. Wang et al., 2014). Consequently, the peak aging time for the composites is shortened compared to that of the monolithic alloy, as reported by related works (Das et al., 1996; M. Gupta & Surappa, 1995; Mandal et al., 2008). In the current work, all the alloy and composite samples undergo identical heat treatment (solid solution at 530 °C for 5 h, and artificial aging at 195 °C for 20 h). It is indicated that TiB₂ particulates cause particulate-assisted precipitation and accelerate the precipitating kinetics of Al2618 matrix, since TiB₂ particles create more dislocations in the matrix during hot rolling process. As a result, the peak aging time of the TiB₂/Al2618 composites is shorter than that in the Al2618 matrix. For the Al2618 alloy, the applied aging time is 20 h in this work. With the same aging time, the TiB₂/Al2618 composites are over-aged and softened therefore. In the heat-treated R35 samples, the softening effect due to over-aging seems to be not so effective. The YS still shows obvious improvement by particle strengthening from the TiB₂ addition. However, in the heat-treated R70 samples, the YS of the composites is only slightly increased (C8-R70) or even decreased (C4-R70), compared to that of the Al2618-R70 alloy. It is believed that in the R70 composites, the particulate-assisted precipitation becomes more effective and the peak-aging time is shortened greatly than the R35 composites. As a result, more evident softening effect is shown in the R70 composites due to over-aging.

7.6 Summary

In this chapter, TiB₂ particulates were introduced in-situ into an Al2618 alloy matrix with minor Sc element via the mixed salt-melt reactions. The TiB₂/Al2618 composites were subjected to hot rolling with 35% and 70% thickness reductions. The microstructure and mechanical properties of the TiB₂/Al2618 composites were studied thoroughly with different TiB₂ volume fraction, rolling thickness reduction and heat treatment conditions. Their effects were investigated in details. The main conclusions are drawn as follows:

1. Hot rolling results in the reduction of porosity, the fragment of intermetallics and the redistribution of TiB_2 particles. With the increase of thickness reduction by hot rolling, the grains are elongated along the rolling direction and the dynamic recrystallization is enhanced.
2. Heat treatment modifies the morphology of the intermetallics and results in the recrystallization of the matrix. With R35 rolling reduction, recrystallization is not evident due to the low driving force for recrystallization. Recrystallization grains are prevailed after heat treatment of R70 samples with a larger degree rolling deformation.
3. The introduction of TiB_2 particles causes the dendrite to equiaxial conversion of the grains. The presence of larger-sized TiB_2 particles and TiB_2 clusters stimulate the recrystallization by particle stimulated nucleation effect. TiB_2 particles also play a role in restricting the growth of recrystallized grains. During heat treatment, TiB_2 particles accelerate the precipitation dynamics by particulate-assisted precipitation, especially in the R70 samples.
4. The mechanical properties of Al2618 and $\text{TiB}_2/\text{Al2618}$ composites are influenced by rolling thickness reduction, heat treatment and the content of TiB_2 particles. At as-rolled state, with the increase of the rolling thickness reduction, the strength and the elongation are both increased, which is attributed to work hardening effect, reduced porosity, the refined intermetallic particles and more uniform TiB_2 particle distribution. Heat treatment results in precipitation hardening and also softening by recrystallization. In R35 samples, precipitation hardening is advantageous and the strength is greatly increased while in R70 samples, the softening effect by recrystallization becomes more evident that contradicts precipitation hardening. The elongation is improved obviously. TiB_2 particles enhanced the strength of all the as-rolled samples and heat-treated R35 samples by particle strengthening effects, with the expense of ductility though. In the heat-treated R70 composites, the particulate-assisted precipitation becomes more effective. Evident softening effect is shown due to over-aging, causing the improvement of elongation but limited increase in strength.
5. Fractography analysis substantiate the reduced porosity with the increase of rolling reduction. TiB_2 particle clusters are prone to damage nucleation zones and facilitate the damage evolution, causing the reduction of elongation of the composites. Heat treatment

and larger hot rolling deformation enhanced ductility from the small and uniform dimples on the fracture surfaces

CHAPTER 8. CONCLUSIONS

The current research has investigated high strength aluminum matrix composites reinforced with in-situ Al_3Ti and TiB_2 particulates. Two representative in-situ particulate reinforced aluminum matrix composites (PRAMCs) $\text{Al}_3\text{Ti}/\text{A356}$ and $\text{TiB}_2/\text{Al2618}$ composites have been studied for the sake of obtaining high strength engineering materials, focusing on the fabrication, microstructure and mechanical properties. For the $\text{Al}_3\text{Ti}/\text{A356}$ composites, another research interest is the evolution of Al-Si-Ti intermetallic phases, which has been a long-debated topic of Al-Si-Ti ternary alloys. Furthermore, a three-dimensional (3D) micromechanical simulation is carried out in order to study the microstructure-properties relationship of PRAMCs, as a complementary part for the experimental works. The study shows that both $\text{Al}_3\text{Ti}/\text{A356}$ and $\text{TiB}_2/\text{Al2618}$ composites have enhanced mechanical properties under suitable fabrication and processing conditions, compared to their alloy matrix counterparts. Major conclusions of the research are drawn as follows:

The $\text{Al}_3\text{Ti}/\text{A356}$ composites with 5 vol. % in-situ Al_3Ti particulates are fabricated via salt-metal reactions. Microstructure analysis reveals the in-situ Al_3Ti particulates in A356 alloy having an average size of 5~6 μm with a blocky morphology in both as-cast and T6 states. The introduction of Al_3Ti particulates retards the growth of coarse-plate eutectic Si phase in the as-cast composites. The addition of Sr in the composites refines the size and the morphology of Si phase. The yield strength of A356 alloy is improved by the addition of 5 vol. % in-situ Al_3Ti particulates for both as-cast and T6 treated samples. However, the elongation is decreased due to the agglomeration of Al_3Ti particulates. With a Sr addition, the elongation and ultimate tensile strength of $\text{Al}_3\text{Ti}/\text{A356}$ composites are both increased due to the refinement of eutectic Si phase.

A series of as-cast $\text{Al}_3\text{Ti}/\text{A356}$ composites are solution treated at 540 °C for different time periods (0~72 h). The TiAlSi intermetallic particulates are blocky $(\text{Al},\text{Si})_3\text{Ti}$ in the as-cast Al-Si-Ti alloy. After solution treatment for 2 h, a lamellar structure starts to form on certain parts of $(\text{Al},\text{Si})_3\text{Ti}$ particulates. With the increase of the solution treatment time, the amount of the lamellar structure increases. The lamellae are Si enriched, containing about 45 %~48 % at. % Si compared to the $(\text{Al},\text{Si})_3\text{Ti}$ particulates that contain ~ 11 at. % Si. The contents of Al, Ti and Si in both $(\text{Al},\text{Si})_3\text{Ti}$ phase and the Si enriched lamellar structure are almost unaffected by the solution treatment time.

Detailed EDS analyses reveal that the lamellar structure consists of Si and Ti enriched stripes (lamellae) with a thickness of 100~200 nm and Al among the stripes. HRTEM observations and corresponding FFT patterns suggest the Si and Ti enriched stripes being an $(\text{Al,Si})_2\text{Ti}$ (τ_2) phase with a TiSi_2 (C49) structure, in which Al substituted Si readily. Between the τ_2 lamellae, Al phase is verified. The Al- τ_2 and $(\text{Al,Si})_3\text{Ti}$ - τ_2 interfaces are commonly found while direct contact between $(\text{Al,Si})_3\text{Ti}$ and τ_2 can hardly be seen from HRTEM observation. The near-rational orientation relationships (OR) are suggested as $(\text{Al,Si})_3\text{Ti}$ $[110] // \text{Al}$ $[110]$, $(\text{Al,Si})_3\text{Ti}$ $(\bar{1}1\bar{2}) // \text{Al}$ $(\bar{1}1\bar{1})$ between $(\text{Al,Si})_3\text{Ti}$ and Al; and Al $[110] // \tau_2$ $[100]$, Al $(1\bar{1}\bar{1}) // \tau_2$ $[060]$ between Al and τ_2 based on the FFT patterns from the interfaces. Thermodynamic calculations of the Al–Si–Ti system also support the transition from a D0_{22} $(\text{Al,Si})_3\text{Ti}$ to a τ_2 phase. τ_1 phase is indicated to be absent in the microstructure after up to 72 h solution treatment.

3D micromechanical finite element simulation is conducted with a series of automatically generated RVEs to model the $\text{Al}_3\text{Ti}/\text{A356}$ composites with various microstructural features, such as Al_3Ti particles of different sizes, volume fractions and distributions. With the decrease of particle size, the yield stress and elongation of the composites are improved. Microscopically, the damage evolution in A356 matrix in the RVEs with smaller Al_3Ti particles is slower and more uniform compared to those containing larger Al_3Ti particles. The increase of particle fraction in the composites can improve the yield strength while reducing the elongation evidently. Microscopic simulation suggests that a larger fraction of particles results in a reduced distance between neighbor particles and causes severe stress concentration. Particle clustering shows no evident effect on yield strength and flow stress at small strain. However, the elongation is reduced with the increase of the fractions of clustering particles. Microscopically, particle clustering facilitates the damage of particles and matrix locally.

The Young's modulus that is predicted by the RVEs in this work shows a good agreement with the calculation of Tsai-Halpin equation. The predicted yield strengths are close to the micromechanics approach considering the load bearing and CTE mismatch strengthening effects. The influence of particle size on yield strength can be revealed by simulation. The relationship between elongation and the Al_3Ti particle properties are predicted from simulation results by a polynomial fitting.

TiB₂ particulates are introduced in-situ in an Al2618 alloy matrix with minor Sc content via the mixed salt-melt reactions. The TiB₂/Al2618 composites are fabricated with different TiB₂ volume fraction, rolling thickness reduction and heat treatment states. Hot rolling results in the reduce of porosity, the fragment of intermetallics and the redistribution of TiB₂ particles. With the increase of thickness reduction by hot rolling, the grains are elongated along the rolling direction and the dynamic recrystallization is enhanced. Heat treatment refines the morphology of the intermetallics and results in the recrystallization of the matrix. The introduction of TiB₂ causes the dendrite to equiaxial conversion of the grains. The presence of larger-sized TiB₂ particles and TiB₂ clusters stimulates the recrystallization by particle stimulated nucleation effect. TiB₂ particles also play a role in restricting the growth of recrystallized grains. During heat treatment, TiB₂ particles accelerate the precipitation dynamics by particulate-assisted precipitation, especially in the R70 samples.

The mechanical properties of Al2618 and TiB₂/Al2618 composites are influenced by TiB₂ volume fraction and processing parameters. At as-rolled state, with the increase of the rolling thickness reduction, the strength and the elongation are both increased, which is attributed to work hardening effect, reduced porosity, the refined intermetallic particles and more uniform TiB₂ distribution. Heat treatment results in precipitation hardening and also softening by recrystallization. In R35 samples, precipitation hardening is prevailed and the strength is greatly increased, while in R70 samples, the softening effect by recrystallization becomes more evident contradicting precipitation hardening. The elongation is improved obviously. TiB₂ particles enhance the strength of all the as-rolled samples and heat-treated R35 samples by particle strengthening effects, at the expense of ductility. In the heat-treated R70 composites, the particulate-assisted precipitation becomes more effective. Evident softening effect is shown due to over-aging, causing the improvement of elongation but limited increase in strength.

REFERENCES

- Abbasi Chianeh, V., Madaah Hosseini, H. R., & Nofar, M. (2009). Micro structural features and mechanical properties of Al-Al₃Ti composite fabricated by in-situ powder metallurgy route. *Journal of Alloys and Compounds*, 473(1–2), 127–132.
<https://doi.org/10.1016/j.jallcom.2008.05.068>
- Amirkhanlou, S., & Niroumand, B. (2011). Development of Al₃Si/SiCp cast composites by injection of SiCp containing composite powders. *Materials & Design*, 32(4), 1895–1902.
- Arnberg, L., Bäckerud, L., & Klang, H. (1982). 1: Production and properties of master alloys of Al–Ti–B type and their ability to grain refine aluminium. *Metals Technology*, 9(1), 1–6.
<https://doi.org/10.1179/030716982803286205>
- ASTM-B557M. (2015). *Standard Test Methods for Tension Testing Wrought and Cast Aluminum- and Magnesium-Alloy Products* (pp. 1–16). <https://doi.org/10.1520/B0557-15.2>
- ASTM-E112. (2013). *Standard Test Methods for Determining Average Grain Size* (pp. 1–27).
<https://doi.org/10.1520/E0112-13.1.4>
- Basavakumar, K. G., Mukunda, P. G., & Chakraborty, M. (2008). Influence of grain refinement and modification on microstructure and mechanical properties of Al–7Si and Al–7Si–2.5 Cu cast alloys. *Materials Characterization*, 59(3), 283–289.
- Basiri Tochae, E., Madaah Hosseini, H. R., & Seyed Reihani, S. M. (2016). Fabrication of high strength in-situ Al-Al₃Ti nanocomposite by mechanical alloying and hot extrusion: Investigation of fracture toughness. *Materials Science and Engineering A*, 658, 246–254.
<https://doi.org/10.1016/j.msea.2016.02.010>
- Bergsma, S. C., Li, X., & Kassner, M. E. (1996). Effects of Thermal Processing and Copper Additions on the Mechanical Properties of Aluminum Alloy Ingot AA 2618. *Journal of Materials Engineering and Performance*, 5(February), 100–102.
- Bian, Z., Xiao, Y., Hu, L., Liu, Y., Chen, Z., Wang, M., Chen, D., & Wang, H. (2020). Stimulated heterogeneous distribution of Sc element and its correlated local hardening effect in Al–Fe–Ni–Sc alloy. *Materials Science and Engineering A*, 771(October 2019), 138650. <https://doi.org/10.1016/j.msea.2019.138650>

- Brukl, C., Nowotny, H., Schob, O., & Benesovsky, F. (1961). Die Kristallstrukturen von TiSi, Ti (Al, Si) 2 und Mo (Al, Si) 2. *Monatshefte Für Chemie Und Verwandte Teile Anderer Wissenschaften*, 92(3), 781–788.
- Caceres, C. H., & Griffiths, J. R. (1996). Damage by the cracking of silicon particles in an Al-7Si-0.4Mg casting alloy. *Acta Materialia*, 44(1), 25–33. [https://doi.org/10.1016/1359-6454\(95\)00172-8](https://doi.org/10.1016/1359-6454(95)00172-8)
- Casati, R., Lemke, J. N., Alarcon, A. Z., & Vedani, M. (2017). Aging Behavior of High-Strength Al Alloy 2618 Produced by Selective Laser Melting. *Metallurgical and Materials Transactions A: Physical Metallurgy and Materials Science*, 48(2), 575–579. <https://doi.org/10.1007/s11661-016-3883-y>
- Ceschini, L., Dahle, A., Gupta, M., Jarfors, A. E. W., Jayalakshmi, S., Morri, A., Rotundo, F., Toschi, S., & Singh, R. A. (2017). *Aluminum and Magnesium Metal Matrix Nanocomposites*. <https://doi.org/10.1007/978-981-10-2681-2>
- Chawla, N., Andres, C., Jones, J. W., & Allison, J. E. (1998). Effect of SiC volume fraction and particle size on the fatigue resistance of a 2080 Al/SiCp composite. *Metallurgical and Materials Transactions. A, Physical Metallurgy and Materials Science*, 29(11), 2843–2854.
- Chawla, N., & Chawla, K. K. (2013). Metal matrix composites. In *Metal Matrix Composites* (Vol. 9781461495). <https://doi.org/10.1007/978-1-4614-9548-2>
- Chawla, N., Ganesh, V. V., & Wunsch, B. (2004). Three-dimensional (3D) microstructure visualization and finite element modeling of the mechanical behavior of SiC particle reinforced aluminum composites. *Scripta Materialia*, 51(2), 161–165. <https://doi.org/10.1016/j.scriptamat.2004.03.043>
- Chawla, N., & Shen, Y. L. (2001). Mechanical behavior of particle reinforced metal matrix composites. *Advanced Engineering Materials*, 3(6), 357–370. [https://doi.org/10.1002/1527-2648\(200106\)3:6<357::AID-ADEM357>3.0.CO;2-I](https://doi.org/10.1002/1527-2648(200106)3:6<357::AID-ADEM357>3.0.CO;2-I)
- Chawla, N., Sidhu, R. S., & Ganesh, V. V. (2006). Three-dimensional visualization and microstructure-based modeling of deformation in particle-reinforced composites. *Acta Materialia*, 54(6), 1541–1548. <https://doi.org/10.1016/j.actamat.2005.11.027>

- Chen, G., Bezold, A., & Broeckmann, C. (2018). Influence of the size and boundary conditions on the predicted effective strengths of particulate reinforced metal matrix composites (PRMMCs). *Composite Structures*, 189(November 2017), 330–339.
<https://doi.org/10.1016/j.compstruct.2018.01.005>
- Chen, T. J., Qin, H., & Zhang, X. Z. (2018). Effects of reheating duration on the microstructure and tensile properties of in situ core-shell-structured particle-reinforced A356 composites fabricated via powder thixoforming. *Journal of Materials Science*, 53(4), 2576–2593.
<https://doi.org/10.1007/s10853-017-1713-2>
- Chen, X., & Fortier, M. (2010). TiAlSi intermetallic formation and its impact on the casting processing in Al-Si alloys. *Journal of Materials Processing Technology*, 210(13), 1780–1786. <https://doi.org/10.1016/j.jmatprotec.2010.06.009>
- Chen, Z., Sun, G. A., Wu, Y., Mathon, M. H., Borbely, A., Chen, D., Ji, G., Wang, M. L., Zhong, S. Y., & Wang, H. W. (2017). Multi-scale study of microstructure evolution in hot extruded nano-sized TiB₂ particle reinforced aluminum composites. *Materials and Design*, 116, 577–590. <https://doi.org/10.1016/j.matdes.2016.12.070>
- Christian, J. W. (1975). The Theory of Transformations in Metals and Alloys. I. *Equilibrium and General Kinetic Theory*, 586.
- Cibula, A. (1949). The mechanism of grain refinement of sand casting in aluminum alloys. *JOURNAL OF THE INSTITUTE OF METALS*, 76(4), 321-+.
- Closset, B., & Gruzleski, J. E. (1982). Structure and properties of hypoeutectic Al-Si-Mg alloys modified with pure strontium. *Metallurgical Transactions A*, 13(6), 945–951.
<https://doi.org/10.1007/BF02643389>
- D.L. Chung, D. (2009). *Composite Materials: Science and Applications*. Springer Science & Business Media. <https://doi.org/10.1007/978-0-387-74365-3>
- Dahle, A. K., Nogita, K., McDonald, S. D., Dinnis, C., & Lu, L. (2005). Eutectic modification and microstructure development in Al-Si Alloys. *Materials Science and Engineering A*, 413–414, 243–248. <https://doi.org/10.1016/j.msea.2005.09.055>
- Dan, C. Y., Chen, Z., Ji, G., Zhong, S. H., Wu, Y., Brisset, F., Wang, H. W., & Ji, V. (2017). Microstructure study of cold rolling nanosized in-situ TiB₂ particle reinforced Al composites. *Materials and Design*, 130(May), 357–365.
<https://doi.org/10.1016/j.matdes.2017.05.076>

- Dan, C. Y., Chen, Z., Mathon, M. H., Ji, G., Li, L. W., Wu, Y., Brisset, F., Guo, L., Wang, H. W., & Ji, V. (2018). Cold rolling texture evolution of TiB₂ particle reinforced Al-based composites by Neutron Diffraction and EBSD analysis. *Materials Characterization*, *136*(August 2017), 293–301. <https://doi.org/10.1016/j.matchar.2017.12.028>
- Dao, M., Chollacoop, N., Van Vliet, K. J., Venkatesh, T. A., & Suresh, S. (2001). Computational modeling of the forward and reverse problems in instrumented sharp indentation. *Acta Materialia*, *49*(19), 3899–3918. [https://doi.org/10.1016/S1359-6454\(01\)00295-6](https://doi.org/10.1016/S1359-6454(01)00295-6)
- Das, T., Munroe, P. R., & Bandyopadhyay, S. (1996). The effect of Al₂O₃ particulates on the precipitation behaviour of 6061 aluminium-matrix composites. *Journal of Materials Science*, *31*(20), 5351–5361. <https://doi.org/10.1007/BF01159304>
- Dezellus, O., Gardiola, B., Andrieux, J., Lomello-Tafin, M., & Viala, J. C. (2014). On the liquid/solid phase equilibria in the Al-rich corner of the Al-Si-Ti ternary system. *Journal of Phase Equilibria and Diffusion*, *35*(2), 137–145.
- Donaldson Steven, L., & Miracle Daniel, B. (2001). Aeronautical Applications of Metal-Matrix Composites. In *ASM Handbook, Volume 21 - Composites* (pp. 1–2). ASM International.
- Donaldson Steven L, & Miracle Daniel B. (2001). Automotive Applications of Metal-Matrix Composites. In *ASM Handbook, Volume 21 - Composites* (pp. 1–1). ASM International.
- Easton, M., & StJohn, D. (1999). Grain refinement of aluminum alloys: Part II. Confirmation of, and a mechanism for, the solute paradigm. *Metallurgical and Materials Transactions A*, *30*(June), 1625–1633. <https://doi.org/10.1007/s11661-999-0099-4>
- Eckslager, A., & Han, W. (2002). A unit cell model for brittle fracture of particles embedded in a ductile matrix. *Computational Materials Science*, *25*, 85–91.
- Elgallad, E. M., Shen, P., Zhang, Z., & Chen, X. (2014). Effects of heat treatment on the microstructure and mechanical properties of AA2618 DC cast alloy. *Materials and Design*, *61*, 133–140. <https://doi.org/10.1016/j.matdes.2014.04.045>
- Fu, C. L. (1990). Electronic, elastic, and fracture properties of trialuminide alloys: Al₃Sc and Al₃Ti. *Journal of Materials Research*, *5*(5), 971–979.
- Fuller, C. B., Seidman, D. N., & Dunand, D. C. (2003). Mechanical properties of Al(Sc,Zr) alloys at ambient and elevated temperatures. *Acta Materialia*, *51*(16), 4803–4814. [https://doi.org/10.1016/S1359-6454\(03\)00320-3](https://doi.org/10.1016/S1359-6454(03)00320-3)

- Gao, T., Li, P., Li, Y., & Liu, X. (2011). Influence of Si and Ti contents on the microstructure, microhardness and performance of TiAlSi intermetallics in Al–Si–Ti alloys. *Journal of Alloys and Compounds*, 509(31), 8013–8017.
- Gao, T., Liu, G., & Liu, X. (2014). Compositions and morphologies of TiAlSi intermetallics in different diffusion couples. *Materials Characterization*, 95, 285–290.
- Gao, X., Zhang, X., Li, A., & Geng, L. (2020). Plastic deformation and fracture behaviors in particle-reinforced aluminum composites: A numerical approach using an enhanced finite element model. *Journal of Composite Materials*, 54(15), 1977–1985.
<https://doi.org/10.1177/0021998319889110>
- Gao, X., Zhu, Y., Easton, M. A., Rinderer, B., Couper, M., & Nie, J.-F. (2015). Characterization and formation of rod-shaped (Al, Si) 3Ti particles in an Al-7Si-0.35 Mg-0.12 Ti (Wt Pct) alloy. *Metallurgical and Materials Transactions A*, 46(8), 3723–3731.
- Gao, Y. H., Kuang, J., Liu, G., & Sun, J. (2019). Effect of minor Sc and Fe co-addition on the microstructure and mechanical properties of Al-Cu alloys during homogenization treatment. *Materials Science and Engineering A*, 746(September 2018), 11–26.
<https://doi.org/10.1016/j.msea.2018.12.099>
- Garcia-Hinojosa, J. A., Gonzalez, C. R., Juárez, J. I., & Surappa, M. K. (2004). Effect of Sr addition on an Al-7Si-10 vol.% SiCpcast composites. *Materials Science and Engineering A*, 382(1–2), 315–320. <https://doi.org/10.1016/j.msea.2004.05.017>
- Ghosh, S., & Moorthy, S. (1998). Particle fracture simulation in non-uniform microstructures of metal-matrix composites. *Acta Materialia*, 46(3), 965–982.
[https://doi.org/10.1016/S1359-6454\(97\)00289-9](https://doi.org/10.1016/S1359-6454(97)00289-9)
- Gu, Y. W., Goi, L. S., Jarfors, A. E. W., Butler, D. L., & Lim, C. S. (2004). Structural evolution in Ti–Si alloy synthesized by mechanical alloying. *Physica B: Condensed Matter*, 352(1–4), 299–304.
- Guo, B., Yi, J., Ni, S., Shen, R., & Song, M. (2016). Factors affecting the microstructure and mechanical properties of Ti-Al₃Ti core-shell-structured particle-reinforced Al matrix composites. *Philosophical Magazine*, 96(12), 1196–1210.
<https://doi.org/10.1080/14786435.2016.1157638>

- Gupta, M., & Surappa, M. K. (1995). Effect of weight percentage of SiC particulates on the ageing behaviour of 6061/SiC metal matrix composites. *Journal of Materials Science Letters*, *14*(18), 1283–1285. <https://doi.org/10.1007/BF01262268>
- Gupta, R., Chaudhari, G. P., & Daniel, B. S. S. (2018). Strengthening mechanisms in ultrasonically processed aluminium matrix composite with in-situ Al₃Ti by salt addition. *Composites Part B: Engineering*, *140*(August 2017), 27–34. <https://doi.org/10.1016/j.compositesb.2017.12.005>
- Halpin, J. C., & Kardos, J. L. (1976). The Halpin-Tsai equations: a review. *Polymer Engineering and Science*, *16*(5), 344–352.
- Hsu, C. J., Chang, C. Y., Kao, P. W., Ho, N. J., & Chang, C. P. (2006). Al-Al₃Ti nanocomposites produced in situ by friction stir processing. *Acta Materialia*, *54*(19), 5241–5249. <https://doi.org/10.1016/j.actamat.2006.06.054>
- Hu, X. H., Jain, M., Wilkinson, D. S., & Mishra, R. K. (2008). Microstructure-based finite element analysis of strain localization behavior in AA5754 aluminum sheet. *Acta Materialia*, *56*(13), 3187–3201. <https://doi.org/10.1016/j.actamat.2008.02.048>
- Humphreys, F. J. (2004). *Recrystallization and related annealing phenomena* (M. Hatherly (ed.); 2nd ed.). Elsevier.
- Humphreys, F. J., Miller, W. S., & Djazeb, M. R. (1990). Microstructural development during thermomechanical processing of particulate metal-matrix composites. *Materials Science and Technology (United Kingdom)*, *6*(11), 1157–1166. <https://doi.org/10.1179/mst.1990.6.11.1157>
- Ibrahim, I. A., Mohamed, F. A., & Lavernia, E. J. (1991). Particulate reinforced metal matrix composites - a review. *Journal of Materials Science*, *26*(5), 1137–1156. <https://doi.org/10.1007/BF00544448>
- Jagadeesh, G. V., & Setti, S. G. (2020). A review on micromechanical methods for evaluation of mechanical behavior of particulate reinforced metal matrix composites. *Journal of Materials Science*, *55*(23), 9848–9882. <https://doi.org/10.1007/s10853-020-04715-2>
- Kang, Y.-C., & Chan, S. L.-I. (2004). Tensile properties of nanometric Al₂O₃ particulate-reinforced aluminum matrix composites. *Materials Chemistry and Physics*, *85*(2–3), 438–443.

- Kanit, T., Forest, S., Galliet, I., Mounoury, V., & Jeulin, D. (2003). Determination of the size of the representative volume element for random composites: Statistical and numerical approach. *International Journal of Solids and Structures*, 40(13–14), 3647–3679. [https://doi.org/10.1016/S0020-7683\(03\)00143-4](https://doi.org/10.1016/S0020-7683(03)00143-4)
- Kapoor, R., Kumar, N., Mishra, R. S., Huskamp, C. S., & Sankaran, K. K. (2010). Influence of fraction of high angle boundaries on the mechanical behavior of an ultrafine grained Al–Mg alloy. *Materials Science and Engineering: A*, 527(20), 5246–5254.
- Kim, C. S., Sohn, I., Nezafati, M., Ferguson, J. B., Schultz, B. F., Bajestani-Gohari, Z., Rohatgi, P. K., & Cho, K. (2013). Prediction models for the yield strength of particle-reinforced unimodal pure magnesium (Mg) metal matrix nanocomposites (MMNCs). *Journal of Materials Science*, 48(12), 4191–4204. <https://doi.org/10.1007/s10853-013-7232-x>
- Klinger, M. (2017). More features, more tools, more CrysTBox. *Journal of Applied Crystallography*, 50(4), 1226–1234.
- Kobayashi, T. (2000). Strength and fracture of aluminum alloys. *Materials Science and Engineering: A*, 280(1), 8–16.
- Kumar, G. B. V., Rao, C. S. P., & Selvaraj, N. (2011). Mechanical and Tribological Behavior of Particulate Reinforced Aluminum Metal Matrix Composites – a review. *Journal of Minerals and Materials Characterization and Engineering*, 10(01), 59–91. <https://doi.org/10.4236/jmmce.2011.101005>
- Kumar, N., Gautam, G., Gautam, R. K., Mohan, A., & Mohan, S. (2016). Synthesis and Characterization of TiB₂ Reinforced Aluminium Matrix Composites: A Review. *Journal of The Institution of Engineers (India): Series D*, 97(2), 233–253. <https://doi.org/10.1007/s40033-015-0091-7>
- Kumar, N. M., Kumaran, S. S., & Kumaraswamidhas, L. A. (2016). Aerospace application on Al 2618 with reinforced e Si₃N₄, AlN and ZrB₂ in-situ composites. *Journal of Alloys and Compounds*, 672, 238–250. <https://doi.org/10.1016/j.jallcom.2016.02.155>
- Kumar, R. V., Keshavamurthy, R., Perugu, C. S., Koppad, P. G., & Alipour, M. (2018). Influence of hot rolling on microstructure and mechanical behaviour of Al6061-ZrB₂ in-situ metal matrix composites. *Materials Science and Engineering A*, 738(September), 344–352. <https://doi.org/10.1016/j.msea.2018.09.104>

- Kurşun, A., Bayraktar, E., & Enginsoy, H. M. (2016). Experimental and numerical study of alumina reinforced aluminum matrix composites: Processing, microstructural aspects and properties. *Composites Part B: Engineering*, 90, 302–314.
<https://doi.org/10.1016/j.compositesb.2016.01.006>
- Kuruville, A. K., Prasad, K. S., Bhanuprasad, V. V., & Mahajan, Y. R. (1990). Microstructure-property correlation in AlTiB₂ (XD) composites. *Scripta Metallurgica et Materialia*, 24(5), 873–878. [https://doi.org/10.1016/0956-716X\(90\)90128-4](https://doi.org/10.1016/0956-716X(90)90128-4)
- Kut, S. (2010). A Simple Method To Determine Ductile Fracture Strain in a Tensile Test of Plane Specimen. *Metalurgija*, 49(4), 295–299.
- Lee, J. C., & Subramanian, K. N. (1992). Effect of cold rolling on the tensile properties of (Al₂O₃)_p/Al composites. *Materials Science and Engineering A*, 159(1), 43–50.
[https://doi.org/10.1016/0921-5093\(92\)90397-J](https://doi.org/10.1016/0921-5093(92)90397-J)
- Li, G., Xu, T., Wang, H., Zhao, Y., Chen, G., & Kai, X. (2021). Microstructure study of hot rolling nanosized in-situ Al₂O₃ particle reinforced A356 matrix composites. *Journal of Alloys and Compounds*, 855, 157107. <https://doi.org/10.1016/j.jallcom.2020.157107>
- Li, J. H., Albu, M., Hofer, F., & Schumacher, P. (2015). Solute adsorption and entrapment during eutectic Si growth in Al–Si-based alloys. *Acta Materialia*, 83, 187–202.
- Li, Y., Zhao, Y. H., Ortalan, V., Liu, W., Zhang, Z. H., Vogt, R. G., Browning, N. D., Lavernia, E. J., & Schoenung, J. M. (2009). Investigation of aluminum-based nanocomposites with ultra-high strength. *Materials Science and Engineering: A*, 527(1–2), 305–316.
- Li, Yang, Gu, Q.-F., Luo, Q., Pang, Y., Chen, S.-L., Chou, K.-C., Wang, X.-L., & Li, Q. (2016). Thermodynamic investigation on phase formation in the Al–Si rich region of Al–Si–Ti system. *Materials & Design*, 102, 78–90.
- Li, Yang, Hu, B., Liu, B., Nie, A., Gu, Q., Wang, J., & Li, Q. (2020). Insight into Si poisoning on grain refinement of Al-Si/Al-5Ti-B system. *Acta Materialia*, 187, 51–65.
- Lin, Y. C., Luo, S.-C., Huang, J., Yin, L.-X., & Jiang, X.-Y. (2018). Effects of solution treatment on microstructures and micro-hardness of a Sr-modified Al-Si-Mg alloy. *Materials Science and Engineering: A*, 725, 530–540.
- Liu, Q., Qi, F., Wang, Q., Ding, H., Chu, K., Liu, Y., & Li, C. (2018). The influence of particles size and its distribution on the degree of stress concentration in particulate reinforced metal matrix composites. *Materials Science and Engineering: A*, 731, 351–359.

- Liu, S., Weitzer, F., Schuster, J. C., Krendelsberger, N., & Du, Y. (2008). On the reaction scheme and liquidus surface in the ternary system Al–Si–Ti. *International Journal of Materials Research*, 99(7), 705–711.
- Liu, X., Liu, Y., Huang, D., Han, Q., & Wang, X. (2017). Tailoring in-situ TiB₂ particulates in aluminum matrix composites. *Materials Science and Engineering A*, 705(May), 55–61. <https://doi.org/10.1016/j.msea.2017.08.047>
- Liu, Z., Cheng, N., Zheng, Q., Wu, J., Han, Q., Huang, Z., Xing, J., Li, Y., & Gao, Y. (2018). Processing and tensile properties of A356 composites containing in situ small-sized Al₃Ti particulates. *Materials Science and Engineering A*, 710(November 2017), 392–399. <https://doi.org/10.1016/j.msea.2017.11.005>
- Liu, Z., Han, Q., Li, J., & Huang, W. (2012). Effect of ultrasonic vibration on microstructural evolution of the reinforcements and degassing of in situ TiB₂p/Al-12Si-4Cu composites. *Journal of Materials Processing Technology*, 212(2), 365–371. <https://doi.org/10.1016/j.jmatprotec.2011.09.021>
- Liu, Z., Rakita, M., Wang, X., Xu, W., & Han, Q. (2014). In situ formed Al₃Ti particles in Al alloy matrix and their effects on the microstructure and mechanical properties of 7075 alloy. *Journal of Materials Research*, 29(12), 1354–1361. <https://doi.org/10.1557/jmr.2014.123>
- Liu, Z. W., Wang, X. M., Han, Q. Y., & Li, J. G. (2014). Effect of ultrasonic vibration on direct reaction between solid ti powders and liquid al. *Metallurgical and Materials Transactions A: Physical Metallurgy and Materials Science*, 45(2), 543–546. <https://doi.org/10.1007/s11661-013-2145-5>
- Liu, Z., Wang, X., Han, Q., & Li, J. (2014). Effects of the addition of Ti powders on the microstructure and mechanical properties of A356 alloy. *Powder Technology*, 253, 751–756. <https://doi.org/10.1016/j.powtec.2013.12.052>
- Lloyd, D. J. (1994). Particle reinforced aluminium and magnesium matrix composites. *International Materials Reviews*, 39(1), 1–23. <https://doi.org/10.1179/imr.1994.39.1.1>
- Lu, S.-Z., & Hellawell, A. (1995). Modification of Al-Si alloys: microstructure, thermal analysis, and mechanisms. *JOM*, 47(2), 38–40.

- Lu, Z., Wei, N., Li, P., Guo, C., & Jiang, F. (2016). Microstructure and mechanical properties of intermetallic Al₃Ti alloy with residual aluminum. *Materials and Design*, *110*, 466–474. <https://doi.org/10.1016/j.matdes.2016.08.025>
- Luo, Q., Li, Q., Zhang, J.-Y., Chen, S.-L., & Chou, K.-C. (2014). Experimental investigation and thermodynamic calculation of the Al–Si–Ti system in Al-rich corner. *Journal of Alloys and Compounds*, *602*, 58–65.
- Ma, S. M., Zhang, P., Ji, G., Chen, Z., Sun, G. A., Zhong, S. Y., Ji, V., & Wang, H. W. (2014). Microstructure and mechanical properties of friction stir processed Al-Mg-Si alloys dispersion-strengthened by nanosized TiB₂ particles. *Journal of Alloys and Compounds*, *616*, 128–136. <https://doi.org/10.1016/j.jallcom.2014.07.092>
- Ma, S., & Wang, X. (2019). Mechanical properties and fracture of in-situ Al₃Ti particulate reinforced A356 composites. *Materials Science and Engineering: A*, *754*, 46–56.
- Ma, S., Wang, Y., & Wang, X. (2020). Microstructures and mechanical properties of an Al-Cu-Mg-Sc alloy reinforced with in-situ TiB₂ particulates. *Materials Science and Engineering A*, *788*(March), 139603. <https://doi.org/10.1016/j.msea.2020.139603>
- Ma, S., Zhuang, X., & Wang, X. (2019). 3D micromechanical simulation of the mechanical behavior of an in-situ Al₃Ti/A356 composite. *Composites Part B: Engineering*, *176*, 107115. <https://doi.org/10.1016/j.compositesb.2019.107115>
- Ma, Y., Ji, G., Chen, Z., Addad, A., & Ji, V. (2018). On the study of a TiB₂ nanoparticle reinforced 7075Al composite with high tensile strength and unprecedented ductility. *Materials Science Forum*, *941 MSF*, 1933–1938. <https://doi.org/10.4028/www.scientific.net/MSF.941.1933>
- Ma, Z. Y., Bi, J., Lu, Y. X., Shen, H. W., & Gao, Y. X. (1993). Microstructure and interface of the in situ forming TiB₂-reinforced aluminum composite. *Composite Interfaces*, *1*(4), 287–291. <https://doi.org/10.1163/156855493X00121>
- Mandal, A., Chakraborty, M., & Murty, B. S. (2008). Ageing behaviour of A356 alloy reinforced with in-situ formed TiB₂ particles. *Materials Science and Engineering A*, *489*(1–2), 220–226. <https://doi.org/10.1016/j.msea.2008.01.042>
- Mann, R. W., & Clevenger, L. A. (1994). The C49 to C54 phase transformation in TiSi₂ thin films. *Journal of The Electrochemical Society*, *141*(5), 1347–1350.

- Manoharan, M., & Lewandowski, J. J. (1992). Effect of reinforcement size and matrix microstructure on the fracture properties of an aluminum metal matrix composite. *Materials Science & Engineering. A, Structural Materials : Properties, Microstructure and Processing*, 150(2), 179–186. [https://doi.org/10.1016/0921-5093\(92\)90110-M](https://doi.org/10.1016/0921-5093(92)90110-M)
- Massalski, T. B. (1990). Binary alloy phase diagrams ASM International. *Materials Park, OH*, 1442–1446.
- McCartney, D. G. (1989). Grain refining of aluminium and its alloys using inoculants. *International Materials Reviews*, 34(1), 247–260. <https://doi.org/10.1179/imr.1989.34.1.247>
- McEvily Jr, A. J. (1994). Aluminum and Aluminum Alloys. In *CHOICE: Current Reviews for Academic Libraries* (Vol. 31, Issues 11–12, p. 1753). American Library Association CHOICE.
- Miracle, D. B. (2005). *Metal matrix composites – From science to technological significance*. 65, 2526–2540. <https://doi.org/10.1016/j.compscitech.2005.05.027>
- Mishnaevsky, L., Derrien, K., & Baptiste, D. (2004). Effect of microstructure of particle reinforced composites on the damage evolution: Probabilistic and numerical analysis. *Composites Science and Technology*, 64(12), 1805–1818. <https://doi.org/10.1016/j.compscitech.2004.01.013>
- Mohanty, P. S., & Gruzleski, J. E. (1995). Mechanism of grain refinement in aluminium. *Acta Metallurgica Et Materialia*, 43(5), 2001–2012. [https://doi.org/10.1016/0956-7151\(94\)00405-7](https://doi.org/10.1016/0956-7151(94)00405-7)
- Mohanty, P. S., & Gruzleski, J. E. (1996). Grain refinement mechanisms of hypoeutectic Al–Si alloys. *Acta Materialia*, 44(9), 3749–3760. [https://doi.org/10.1016/1359-6454\(96\)00021-3](https://doi.org/10.1016/1359-6454(96)00021-3)
- Mondolfo, L. F. (1976). *Al–Si–Ti Aluminum–Silicon–Titanium system* (L. F. B. T.-A. A. Mondolfo (ed.); pp. 614–615). Butterworth-Heinemann. <https://doi.org/https://doi.org/10.1016/B978-0-408-70932-3.50334-X>
- Mortensen, A., & Llorca, J. (2010). Metal matrix composites. *Annual Review of Materials Research*, 40, 243–270.

- Nampoothiri, J., Harini, R. S., Nayak, S. K., Raj, B., & Ravi, K. R. (2016). Post in-situ reaction ultrasonic treatment for generation of Al-4.4Cu/TiB₂ nanocomposite: A route to enhance the strength of metal matrix nanocomposites. *Journal of Alloys and Compounds*, 683, 370–378. <https://doi.org/10.1016/j.jallcom.2016.05.067>
- Nardone, V. C., & Prewo, K. M. (1986). On the strength of discontinuous silicon carbide reinforced aluminum composites. *Scripta Metallurgica*, 20(1), 43–48.
- Nofar, M., Madaah Hosseini, H. R., & Kolagar-Daroonkolaie, N. (2009). Fabrication of high wear resistant Al/Al₃Ti metal matrix composite by in situ hot press method. *Materials & Design*, 30(2), 280–286. <https://doi.org/https://doi.org/10.1016/j.matdes.2008.04.071>
- Norby, P., Christensen, A. N., & Pedersen, E. (1986). Preparation and structure of Al₃Ti. *Acta Chemica Scandinavica, Series A*, 40, 157.
- Nový, F., Janeček, M., & Král, R. (2009). Microstructure changes in a 2618 aluminium alloy during ageing and creep. *Journal of Alloys and Compounds*, 487(1–2), 146–151. <https://doi.org/10.1016/j.jallcom.2009.08.014>
- Nukami, T., & Flemings, M. C. (1995). In situ synthesis of TiC particulate-reinforced aluminum matrix composites. *Metallurgical and Materials Transactions A*, 26(7), 1877–1884. <https://doi.org/10.1007/BF02670775>
- Özbek, İ. (2007). A study on the re-solution heat treatment of AA 2618 aluminum alloy. *Materials Characterization*, 58(3), 312–317.
- Pande, C. S., & Cooper, K. P. (2009). Nanomechanics of Hall-Petch relationship in nanocrystalline materials. *Progress in Materials Science*, 54(6), 689–706. <https://doi.org/10.1016/j.pmatsci.2009.03.008>
- Pang, J. C., Cui, X. P., Li, A. B., Fan, G. H., Geng, L., Zheng, Z. Z., & Wang, Q. W. (2013). Effect of solid solution of Si on mechanical properties of TiAl₃ based on the multi-laminated Ti- (SiC P / Al) composite system. *Materials Science & Engineering A*, 579, 57–63. <https://doi.org/10.1016/j.msea.2013.05.007>
- Perrot, P. (1990). *Aluminium-silicon-titanium In: Petzow, G., Effenberg, G. (Eds.), Ternary Alloys-A Comprehensive Compendium of Evaluated Constitutional Data and Phase Diagrams*. VCH Publishers.

- Pramod, S. L., Prasada Rao, A. K., Murty, B. S., & Bakshi, S. R. (2015). Effect of Sc addition on the microstructure and wear properties of A356 alloy and A356-TiB₂ in situ composite. *Materials and Design*, 78, 85–94. <https://doi.org/10.1016/j.matdes.2015.04.026>
- Qin, Q. D., Zhao, Y. G., Liu, C., Zhou, W., & Jiang, Q. C. (2007). Development of aluminium composites with in situ formed AlTiSi reinforcements through infiltration. *Materials Science and Engineering: A*, 460, 604–610.
- Qing, H. (2013a). 2D micromechanical analysis of SiC/Al metal matrix composites under tensile, shear and combined tensile/shear loads. *Materials and Design*, 51, 438–447. <https://doi.org/10.1016/j.matdes.2013.04.051>
- Qing, H. (2013b). Automatic generation of 2D micromechanical finite element model of silicon-carbide/aluminum metal matrix composites: Effects of the boundary conditions. *Materials and Design*, 44, 446–453. <https://doi.org/10.1016/j.matdes.2012.08.011>
- Qiu, D., Taylor, J. A., Zhang, M. X., & Kelly, P. M. (2007). A mechanism for the poisoning effect of silicon on the grain refinement of Al–Si alloys. *Acta Materialia*, 55(4), 1447–1456.
- Ramakrishnan, N. (1996). An analytical study on strengthening of particulate reinforced metal matrix composites. *Acta Materialia*, 44(1), 69–77. [https://doi.org/https://doi.org/10.1016/1359-6454\(95\)00150-9](https://doi.org/https://doi.org/10.1016/1359-6454(95)00150-9)
- Raman, A. (1965). “Über den Aufbau einiger zu TiAl₃ verwandter Legierungsreihen. II. Untersuchungen in einigen T-Al-Si und T⁴... T⁶ Li Systemen”, im Dreistoif: Mn-Al-Si. *Z. Metallkd*, 56, 44–52.
- Ramazani, A., Mukherjee, K., Quade, H., Prah, U., & Bleck, W. (2013). Correlation between 2D and 3D flow curve modelling of DP steels using a microstructure-based RVE approach. *Materials Science and Engineering A*, 560, 129–139. <https://doi.org/10.1016/j.msea.2012.09.046>
- Ramazani, A., Mukherjee, K., Schwedt, A., Goravanchi, P., Prah, U., & Bleck, W. (2013). Quantification of the effect of transformation-induced geometrically necessary dislocations on the flow-curve modelling of dual-phase steels. *International Journal of Plasticity*, 43, 128–152. <https://doi.org/10.1016/j.ijplas.2012.11.003>

- Ramazani, A., Pinard, P. T., Richter, S., Schwedt, A., & Prah, U. (2013). Characterisation of microstructure and modelling of flow behaviour of bainite-aided dual-phase steel. *Computational Materials Science*, *80*, 134–141.
<https://doi.org/10.1016/j.commatsci.2013.05.017>
- Rao, J., Zhang, J., Liu, R., Zheng, J., & Yin, D. (2018). Modification of eutectic Si and the microstructure in an Al-7Si alloy with barium addition. *Materials Science and Engineering: A*, *728*, 72–79.
- Rice, J. R., & Tracey, D. M. (1969). On the ductile enlargement of voids in triaxial stress fields. *Journal of the Mechanics and Physics of Solids*, *17*(3), 201–217.
- Riley, D. P., Oliver, C. P., & Kisi, E. H. (2006). In-situ neutron diffraction of titanium silicide, Ti₅Si₃, during self-propagating high-temperature synthesis (SHS). *Intermetallics*, *14*(1), 33–38.
- Safiri, M., Meratian, M., & Panjepour, M. (2019). Fabrication of Al-TiAl₃ Composite Via In-Situ Accumulative Roll Bonding (ARB) and Annealing. *Metallurgical and Materials Transactions A: Physical Metallurgy and Materials Science*, *50*(1), 415–425.
<https://doi.org/10.1007/s11661-018-4986-4>
- Samuel, A. M., Doty, H. W., Valtierra, S., & Samuel, F. H. (2014). Effect of grain refining and Sr-modification interactions on the impact toughness of Al-Si-Mg cast alloys. *Materials and Design*, *56*, 264–273. <https://doi.org/10.1016/j.matdes.2013.10.029>
- Sanaty-Zadeh, A. (2012). Comparison between current models for the strength of particulate-reinforced metal matrix nanocomposites with emphasis on consideration of Hall–Petch effect. *Materials Science and Engineering: A*, *531*, 112–118.
- Saraev, D., & Schmauder, S. (2003). *Finite element modelling of Al / SiC p metal matrix composites with particles aligned in stripes — a 2D – 3D comparison*. *19*, 733–747.
- Schubert, K., Frank, K., Gohle, R., Maldonado, A., Meissner, H. G., Raman, A., & Rossteutscher, W. (1963). Some Structural Data of Metallic Phases. Part VIII. *Naturwissenschaften (West Germany)*, *50*.
- Schubert, K., Raman, A., & Rossteutscher, W. (1964). Structural Data of Some Metallic Phases. *Naturwissenschaften*, *51*(12), 287.
- Sekine, H., & Chent, R. (1995). A combined microstructure strengthening analysis of SiCp/Al metal matrix composites. *Composites*, *26*(3), 183–188.

- Shao, J. C., Xiao, B. L., Wang, Q. Z., Ma, Z. Y., & Yang, K. (2011). An enhanced FEM model for particle size dependent flow strengthening and interface damage in particle reinforced metal matrix composites. *Composites Science and Technology*, *71*(1), 39–45.
<https://doi.org/10.1016/j.compscitech.2010.09.014>
- Shen, P., Elgallad, E. M., & Chen, X. G. (2016). On the aging behavior of AA2618 DC cast alloy. *Minerals, Metals and Materials Series*, *210869*, 373–377.
https://doi.org/10.1007/978-3-319-65136-1_65
- Shorowordi, K. M., Laoui, T., Haseeb, A. S. M. A., Celis, J. P., & Froyen, L. (2003). Microstructure and interface characteristics of B₄C, SiC and Al₂O₃ reinforced Al matrix composites: A comparative study. *Journal of Materials Processing Technology*, *142*(3), 738–743. [https://doi.org/10.1016/S0924-0136\(03\)00815-X](https://doi.org/10.1016/S0924-0136(03)00815-X)
- Srivatsan, T. S., Zhang, Y., & Harrigan Jr, W. C. (2018). *Metal-Matrix Composites Innovations, Advances and Applications*. Springer.
- Sun, X., Choi, K. S., Liu, W. N., & Khaleel, M. A. (2009). Predicting failure modes and ductility of dual phase steels using plastic strain localization. *International Journal of Plasticity*, *25*(10), 1888–1909. <https://doi.org/10.1016/j.ijplas.2008.12.012>
- Sung, Y., Joshi, S. P., & Ramesh, K. T. (2009). An enhanced continuum model for size-dependent strengthening and failure of particle-reinforced composites. *Acta Materialia*, *57*(19), 5848–5861. <https://doi.org/10.1016/j.actamat.2009.08.010>
- Suthar, J., & Patel, K. M. (2018). Processing issues, machining, and applications of aluminum metal matrix composites. *Materials and Manufacturing Processes*, *33*(5), 499–527.
<https://doi.org/10.1080/10426914.2017.1401713>
- Tahamtan, S., Halvae, A., Emamy, M., Jiang, Z. Y., & Fadavi Boostani, A. (2014). Exploiting superior tensile properties of a novel network-structure AlA206 matrix composite by hybridizing micron-sized Al₃Ti with Al₂O₃ nano particulates. *Materials Science and Engineering A*, *619*, 190–198. <https://doi.org/10.1016/j.msea.2014.09.090>
- Tahiri, H., Mohamed, S. S., Doty, H. W., Valtierra, S., & Samuel, F. H. (2018). Effect of Sr–Grain Refining–Si Interactions on the Microstructural Characteristics of Al–Si Hypoeutectic Alloys. *International Journal of Metalcasting*, *12*(2), 343–361.
<https://doi.org/10.1007/s40962-017-0169-0>

- Tan, M., Xin, Q., Li, Z., & Zong, B. Y. (2001). Influence of SiC and Al₂O₃ particulate reinforcements and heat treatments on mechanical properties and damage evolution of Al-2618 metal matrix composites. *Journal of Materials Science*, *36*(8), 2045–2053. <https://doi.org/10.1023/A:1017591117670>
- Tang, J., Geng, J., Xia, C., Wang, M., Chen, D., & Wang, H. (2019). Superior Strength and Ductility of In Situ Nano TiB₂/Al–Cu–Mg Composites by Cold Rolling and Post-Aging Treatment. *Materials*, *12*(21), 3626.
- Tao, R., Zhao, Y., Kai, X., Zhao, Z., Ding, R., Liang, L., & Xu, W. (2018). Effects of hot rolling deformation on the microstructure and tensile properties of an in situ-generated ZrB₂ nanoparticle-reinforced AA6111 composite. *Materials Science and Engineering A*, *732*(June), 138–147. <https://doi.org/10.1016/j.msea.2018.06.107>
- Tearney, G. J., Brezinski, M. E., Southern, J. F., Bouma, B. E., Boppart, S. A., & Fujimoto, J. G. (1997). Optical biopsy in human urologic tissue using optical coherence tomography. *The Journal of Urology*, *157*(5), 1915–1919.
- Timpel, M., Wanderka, N., Schlesiger, R., Yamamoto, T., Lazarev, N., Isheim, D., Schmitz, G., Matsumura, S., & Banhart, J. (2012). The role of strontium in modifying aluminium-silicon alloys. *Acta Materialia*, *60*(9), 3920–3928. <https://doi.org/10.1016/j.actamat.2012.03.031>
- Tjong, S. C., & Lau, K. C. (1999). Properties and abrasive wear of TiB₂/Al-4% Cu composites produced by hot isostatic pressing. *Composites Science and Technology*, *59*(13), 2005–2013.
- Tjong, S., & Ma, Z. Y. (2000). Microstructural and mechanical characteristics of in situ metal matrix composites. *Materials Science and Engineering: R: Reports*, *29*(3–4), 49–113. [https://doi.org/10.1016/S0927-796X\(00\)00024-3](https://doi.org/10.1016/S0927-796X(00)00024-3)
- Tomida, S., Nakata, K., Shibata, S., Zenkouji, I., & Saji, S. (2003). Improvement in wear resistance of hyper-eutectic Al–Si cast alloy by laser surface remelting. *Surface and Coatings Technology*, *169*, 468–471.
- Tursun, G., Weber, U., Soppa, E., & Schmauder, S. (2006). The influence of transition phases on the damage behaviour of an Al/10vol.%SiC composite. *Computational Materials Science*, *37*(1–2), 119–133. <https://doi.org/10.1016/j.commatsci.2005.12.018>

- Villars, P., Prince, A., & Okamoto, H. (1995). *Handbook of ternary alloy phase diagrams* (Vol. 5). ASM international Materials Park, OH.
- Wang, D., Zhang, H., Nagaumi, H., Jia, P., & Cui, J. (2020). Microstructural homogeneity, mechanical properties, and wear behavior of in situ Mg₂Si particles reinforced Al-matrix composites fabricated by hot rolling. *Journal of Materials Research and Technology*, 9(2), 1882–1892. <https://doi.org/10.1016/j.jmrt.2019.12.020>
- Wang, J. H., & Yi, D. Q. (2006). Preparation and properties of alloy 2618 reinforced by submicron AlN particles. *Journal of Materials Engineering and Performance*, 15(5), 596–600.
- Wang, M., Chen, D., Chen, Z., Wu, Y., Wang, F., Ma, N., & Wang, H. (2014). Mechanical properties of in-situ TiB₂/A356 composites. *Materials Science and Engineering A*, 590, 246–254. <https://doi.org/10.1016/j.msea.2013.10.021>
- Wang, Q. G., & Davidson, C. J. (2001). Solidification and precipitation behaviour of Al-Si-Mg casting alloys. *Journal of Materials Science*, 36(3), 739–750. <https://doi.org/10.1023/A:1004801327556>
- Wang, T., Chen, Z., Zheng, Y., Zhao, Y., Kang, H., & Gao, L. (2014). Development of TiB₂ reinforced aluminum foundry alloy based in situ composites - Part II: Enhancing the practical aluminum foundry alloys using the improved Al-5wt%TiB₂ master composite upon dilution. *Materials Science and Engineering A*, 605, 22–32. <https://doi.org/10.1016/j.msea.2014.03.021>
- Wang, X., Jha, A., & Brydson, R. (2004). In situ fabrication of Al₃Ti particle reinforced aluminium alloy metal-matrix composites. *Materials Science and Engineering A*, 364(1–2), 339–345. <https://doi.org/10.1016/j.msea.2003.08.049>
- Wang, X., Liu, Z., Dai, W., & Han, Q. (2015). On the Understanding of Aluminum Grain Refinement by Al-Ti-B Type Master Alloys. *Metallurgical and Materials Transactions B: Process Metallurgy and Materials Processing Science*, 46(4), 1620–1625. <https://doi.org/10.1007/s11663-014-0252-3>
- Wang, Z., Song, M., Sun, C., & He, Y. (2011). Effects of particle size and distribution on the mechanical properties of SiC reinforced Al-Cu alloy composites. *Materials Science and Engineering A*, 528(3), 1131–1137. <https://doi.org/10.1016/j.msea.2010.11.028>

- Weng, L., Fan, T., Wen, M., & Shen, Y. (2019). Three-dimensional multi-particle FE model and effects of interface damage, particle size and morphology on tensile behavior of particle reinforced composites. *Composite Structures*, 209(October 2018), 590–605.
<https://doi.org/10.1016/j.compstruct.2018.11.008>
- Wu, J. M., Zheng, S. L., & Li, Z. Z. (2000). *Thermal stability and its effects on the mechanical properties of rapidly solidified Al-Ti alloys*. 289, 246–254.
- Xiao, P., Gao, Y., Yang, C., Liu, Z., Li, Y., & Xu, F. (2018). Microstructure, mechanical properties and strengthening mechanisms of Mg matrix composites reinforced with in situ nanosized TiB₂ particles. *Materials Science and Engineering: A*, 710(October), 251–259. <https://doi.org/10.1016/j.msea.2017.10.107>
- Xiong, H.-P., Mao, W., Xie, Y.-H., Ma, W.-L., Chen, Y.-F., Li, X.-H., Li, J.-P., & Cheng, Y.-Y. (2004). Liquid-phase siliconizing by Al–Si alloys at the surface of a TiAl-based alloy and improvement in oxidation resistance. *Acta Materialia*, 52(9), 2605–2620.
- Yang, C., Liu, Z., Zheng, Q., Cao, Y., Dai, X., Sun, L., Zhao, J., Xing, J., & Han, Q. (2018). Ultrasound assisted in-situ casting technique for synthesizing small-sized blocky Al₃Ti particles reinforced A356 matrix composites with improved mechanical properties. *Journal of Alloys and Compounds*, 747, 580–590.
<https://doi.org/10.1016/j.jallcom.2018.02.010>
- Yang, R., Zhang, Z., Zhao, Y., Chen, G., Guo, Y., Liu, M., & Zhang, J. (2015). Effect of multi-pass friction stir processing on microstructure and mechanical properties of Al₃Ti/A356 composites. *Materials Characterization*, 106, 62–69.
<https://doi.org/10.1016/j.matchar.2015.05.019>
- Yu, H., Chen, H., Sun, L., & Min, G. (2006). Preparation of Al-Al₃Ti in situ composites by direct reaction method. *Rare Metals*, 25(1), 32–36.
- Yu, K., Li, W., Li, S., & Zhao, J. (2004). Mechanical properties and microstructure of aluminum alloy 2618 with Al₃(Sc, Zr) phases. *Materials Science and Engineering A*, 368(1–2), 88–93. <https://doi.org/10.1016/j.msea.2003.09.092>
- Zeng, Y., Himmler, D., Randelzhofer, P., & Körner, C. (2018). Microstructures and Mechanical Properties of Al₃Ti/Al Composites Produced In Situ by High Shearing Technology. *Advanced Engineering Materials*, 1800259.

- Zhang, J. F., Zhang, X. X., Wang, Q. Z., Xiao, B. L., & Ma, Z. Y. (2018). Simulations of deformation and damage processes of SiCp/Al composites during tension. *Journal of Materials Science and Technology*, *34*(4), 627–634.
<https://doi.org/10.1016/j.jmst.2017.09.005>
- Zhang, J., Ouyang, Q., Guo, Q., Li, Z., Fan, G., Su, Y., Jiang, L., Lavernia, E. J., Schoenung, J. M., & Zhang, D. (2016). 3D Microstructure-based finite element modeling of deformation and fracture of SiCp/Al composites. *Composites Science and Technology*, *123*, 1–9. <https://doi.org/10.1016/j.compscitech.2015.11.014>
- Zhang, Q., Xiao, B. L., Wang, D., & Ma, Z. Y. (2011). Formation mechanism of in situ Al₃Ti in Al matrix during hot pressing and subsequent friction stir processing. *Materials Chemistry and Physics*, *130*, 1109–1117.
<https://doi.org/10.1016/j.matchemphys.2011.08.042>
- Zhang, X. X., Xiao, B. L., Andrä, H., & Ma, Z. Y. (2014). Homogenization of the average thermo-elastoplastic properties of particle reinforced metal matrix composites: The minimum representative volume element size. *Composite Structures*, *113*(1), 459–468.
<https://doi.org/10.1016/j.compstruct.2014.03.048>
- Zhang, Z., Hosoda, S., Kim, I.-S., & Watanabe, Y. (2006). Grain refining performance for Al and Al–Si alloy casts by addition of equal-channel angular pressed Al–5 mass% Ti alloy. *Materials Science and Engineering: A*, *425*(1–2), 55–63.
- Zhao, Y. G., Qin, Q. D., Zhao, Y. Q., Liang, Y. H., & Jiang, Q. C. (2004). In situ Mg₂Si/Al–Si composite modified by K₂TiF₆. *Materials Letters*, *58*(16), 2192–2194.
<https://doi.org/https://doi.org/10.1016/j.matlet.2004.01.016>
- Zhou, J., Gokhale, A. M., Gurumurthy, A., & Bhat, S. P. (2015). Realistic microstructural RVE-based simulations of stress-strain behavior of a dual-phase steel having high martensite volume fraction. *Materials Science and Engineering A*, *630*, 107–115.
<https://doi.org/10.1016/j.msea.2015.02.017>
- Zhu, G., Dai, Y., Shu, D., Xiao, Y., Yang, Y., Wang, J., Sun, B., & Boom, R. (2011). Intermetallics Diffusion mechanisms of vacancy and doped Si in Al₃Ti from first-principles calculations. *Intermetallics*, *19*(7), 1036–1040.
<https://doi.org/10.1016/j.intermet.2011.03.012>

- Zhu, G., Wang, R., Wang, W., Shu, D., Dong, A., Wang, D., & Wang, J. (2017). The Removal of Impurity Silicon from Aluminum Melt by the Addition of K₂TiF₆. *Key Engineering Materials*, 748, 192–196. <https://doi.org/10.4028/www.scientific.net/KEM.748.192>
- Zhu, M., Jian, Z., Yang, G., & Zhou, Y. (2012). Effects of T6 heat treatment on the microstructure, tensile properties, and fracture behavior of the modified A356 alloys. *Materials & Design (1980-2015)*, 36, 243–249.

PUBLICATIONS

- Ma, S., Li, N., Zhang, C., & Wang, X. (2020). Evolution of intermetallic phases in an Al–Si–Ti alloy during solution treatment. *Journal of Alloys and Compounds*, 831, 154872. <https://doi.org/10.1016/j.jallcom.2020.154872>
- Ma, S., & Wang, X. (2019). Mechanical properties and fracture of in-situ Al₃Ti particulate reinforced A356 composites. *Materials Science and Engineering A*, 754(January), 46–56. <https://doi.org/10.1016/j.msea.2019.03.044>
- Ma, S., Wang, Y., & Wang, X. (2019). The in-situ formation of Al₃Ti reinforcing particulates in an Al-7wt%Si alloy and their effects on mechanical properties. *Journal of Alloys and Compounds*, 792, 365–374. <https://doi.org/10.1016/j.jallcom.2019.04.064>
- Ma, S., Wang, Y., & Wang, X. (2020). Microstructures and mechanical properties of an Al-Cu-Mg-Sc alloy reinforced with in-situ TiB₂ particulates. *Materials Science and Engineering A*, 788(March), 139603. <https://doi.org/10.1016/j.msea.2020.139603>
- Ma, S., Zhang, X., Chen, T., & Wang, X. (2020). Microstructure-based numerical simulation of the mechanical properties and fracture of a Ti-Al₃Ti core-shell structured particulate reinforced A356 composite. *Materials and Design*, 191, 108685. <https://doi.org/10.1016/j.matdes.2020.108685>
- Ma, S., Zhuang, X., & Wang, X. (2019). 3D micromechanical simulation of the mechanical behavior of an in-situ Al₃Ti/A356 composite. *Composites Part B: Engineering*, 176, 107115. <https://doi.org/10.1016/j.compositesb.2019.107115>
- Ma, S., Zhuang, X., & Wang, X. (2021). Particle distribution-dependent micromechanical simulation on mechanical properties and damage behaviors of particle reinforced metal matrix composites. *Journal of Materials Science*, 56(11), 6780–6798. <https://doi.org/10.1007/s10853-020-05684-2>
- Ma, S., & Wang, X. (2019). The Effects of Strontium Addition on the Microstructures and Mechanical Properties of Al-7Si Alloy Reinforced with In Situ Al₃Ti Particulates. *Light Metals*, 1485–1490. https://doi.org/10.1007/978-3-030-05864-7_186
- Ma, S. et al. (2019). Aluminum matrix composites: the formation and effects of in-situ reinforcing particles, *MS&T 2019-Light Metal Technology*

- Zhang, X., Chen, T., Ma, S., Qin, H., & Ma, J. (2021). Overcoming the strength-ductility trade-off of an aluminum matrix composite by novel core-shell structured reinforcing particulates. *Composites. Part B, Engineering*, 206. <https://doi.org/10.1016/j.compositesb.2020.108541>
- Huang, D., Yan, D., Ma, S., & Wang, X. (2018). Scandium on the formation of in situ TiB₂ particulates in an aluminum matrix. *J. Mater. Res*, 33(18), 2721–2727. <https://doi.org/10.1557/jmr.2018.208>
- Ma, S., Jiang, A., & Wang, X. (2021). Effects of hot rolling and heat treatment on the microstructure and mechanical properties of in-situ TiB₂/Al-Cu-Mg-Sc composites. Submitted to *Materials Science and Engineering A*